Abstract

High-coherence Phononic Resonator for Quantum Acoustic Applications

Yizhi Luo

2025

Long-lived phonons are a promising quantum resource, enabling advanced applications in quantum sensing, transduction, and memory. While mechanical resonators spanning over a wide range of frequencies have been demonstrated, high-frequency (GHz) phonons are particularly sought after for quantum acoustic systems, as they permit ground-state operations at cryogenic temperatures and are more readily controlled using quantum optics and circuit-QED techniques. Recent advancements in silicon-based nanomechanical resonators have demonstrated lifetimes on the order of seconds; however, their coherence times are constrained to $\sim$ 100 us due to pronounced surface interactions.

In this thesis, I will present a different type of phononic resonator: a microfabricated high-overtone bulk acoustic resonator (μHBAR) based on high-purity quartz crystal. These resonators achieve Q-factors of 360 million at 12 GHz, translating to phonon coherence times of nearly 10 ms and record-setting f-Q products of 4.6×10^{18} Hz. The coherence time was derived from the phonon spectral linewidth measured by a novel Brillouin-based laser spectroscopy technique. Complementary spectral and coherent ring-down measurements revealed negligible dephasing within these oscillators. Furthermore, surface-limited phonon dissipation was identified and found to extend far beyond surface roughness scattering, implicating subsurface defects—such as lattice distortions, dislocations, and elemental contamination—as significant contributors. By employing an optimized polishing process in conjunction with advanced material diagnostic techniques, including X-ray diffraction (XRD) and atomic force microscopy (AFM), the above record-high phonon coherence times have been realized.

In conclusion, μHBARs not only provide an ideal platform for hosting high-coherence phonons, unlocking a wide spectrum of quantum applications, but also serve as a valuable testbed for investigating fundamental material properties and surface interactions.

High-coherence Phononic Resonator for Quantum Acoustic Applications

A Dissertation
Presented to the Faculty of the Graduate School
of
Yale University
in Candidacy for the Degree of
Doctor of Philosophy

by
Yizhi Luo

Dissertation Director: Peter T. Rakich

May 2025

Contents

List of Figures

List of Tables

Acknowledgments

Has it been this long already! Eight years later, I'm finally graduating from Yale. Looking back from now, my journey at Yale (also at the United States) has been cut into two periods. In the pre-pandemic era, I was immersed in the joy and excitement of getting into such a prestigious university and having the chance to learn from the world-class physicists. I spent most of my time on taking classes and reading textbooks (such as quantum field theory, general relativity, and differential topology) that are not relevant to the my research at all. Now looking back, I was so capricious and had not the faintest idea what modern research is like. I genuinely thought PhD was such a long period that it should give you enough time to master all these topics and get the experimental work done as well. Happy time always passes quickly. I could never forget the moment when I stepped my foot on the plane that would take me to home China after I finished my area exam and officially became a PhD candidate. It was the Christmas of year 2019 and I had no idea what was in front of me. Then the world was hit by the wildest pandemic and everything turned into chaos. Too many things happened and too many lessons were learned in the hardest way (these stories are beyond the scope of this section and will be told elsewhere maybe in the future). Anyways, I was able to get back to Yale again, only after one and a half years, in the summer of year 2021. The pandemic hit me in the most unexpected way and changed my whole course all of a sudden. I have no choice but keep my nose down to the lab work since 2021, when I have to start almost everything

from scratch. Here I am, ten days from my PhD defense, with very complex feelings. On one hand, I feel pretty sad about all the time wasted in the past years. On the other hand, I feel proud that I survived and am still able to do physics. There is one thing that becomes more and more clear to me over all these difficult years: I love doing physics and still want to be a physicist.

Enough ranting about my past, I'm ready to give my thanks to so many people that I met through this journey. The first one I'd like to thank is with no doubt, my advisor Professor Peter Rakich. I decided to join Peter's lab after the first meeting with him. Till this date, I still believe he is the best professor I can find at Yale (call me biased). Peter has a special type of charisma in him that makes you want to work with him, and I'm not sure it can be learned. I appreciate the opportunity to work in his lab and his mentorship. His knowledge about experimental details and his passion about building things still amaze me to this date. Most importantly, he cares about his students. There are so many frustrating days and nights in my PhD years. However, his messages like "Good job! Keep on it" or "Fantastic!!! well done" always come in time when they are needed the most. Peter, thank you for your patience and constant support through all these years. Let's keep in touch.

Prash, thank you for your mentorship in my early years at Yale. You are the most productive and knowledgeable PhD student that I know. You look so confident when making life choices and always seem to know where you are heading. The memories we had together are always joyful.

Hagai, thank you for the friendship and the energy you brought into our office. Thank you for sharing the Jewish culture and I'm glad we share a lot of values in common. Wish you all the best for starting your new lab in Israel.

Haotian, losing to your Hum in Warcraft III is just because I haven't practiced and get rusty. Will challenge you again.

With that said, I'd like to express my thanks to all the classmates and labmates

I've worked with. I appreciate all the help and communication from you guys.

I feel very lucky to meet a bunch of friends on Yale's badminton court, old ones (pre-pandemic) and new ones (post-pandemic). Although we complained so much about the badminton facility at Yale, once the game is on, we'll have 100% pure joy. Thanks for the companion and competition. I will miss you guys so much.

At last, shout out to the Yale Tango Club. Learning Tango is one of the few things I feel most proud of during my years at Yale. Thank you, Clara and Jon, for introducing me to the family. I've witnessed the growth of the club and your leadership is just amazing.

Now it is time to say goodbye. Good luck everyone. Hope we can cross paths again in the near future.

Chapter 1

Introduction

Phonons, or acoustic waves, are the collective modes of mechanical vibration of atoms. It has long been studied in the history of physics and enabled a wide range of classical applications in the advancement of technology including time keeping [1], sensing [2,3], and micro-wave filtering [4–6]. Recently, with the development of the emerging quantum technology, phonon has become a compelling quantum resource and has caught wide attention in quantum information and metrology. A relatively new field of quantum acoustics has been built where people look for smart ways to control and engineer non-classical phonon states in the quantum regime [7–9]. It has been a lasting challenge in controlling and measuring complex quantum states in the motion of a macroscopic solid-state object because, unlike photons can propagate in vacuum, phonons can only propagate in complex and potentially lossy media. However, phonons bring a new degree of freedom into the quantum hybrid system and open a lot of opportunities in applications such as quantum sensing [10–13], quantum transduction [14–17], and quantum memory [18–21]. Since the sound speed is usually five orders of magnitude lower than the electromagnetic waves, these quantum acoustic devices should be much more compact than its electromagnetic counterparts.

Long-lived phonons have been favored and sought after for quantum applications

as they permit more quantum operations within its coherence time. Over the past three decades, a variety of mechanical oscillators have been designed and built to produce such long-lived phonons over a wide range of frequencies [22]. The high-frequency (>GHz) phononic resonators are typically demanded for quantum applications because they are more immune to environmental noise, easier to be cooled down to ground state, and more readily controlled using quantum optics and circuit quantum electrodynamics (cQED) techniques.

Recently, micro-fabricated nanomechanical resonators have demonstrated extremely long lifetimes (> 1 s) [19]. This is achieved by fabricating phononic bandgap structures at both ends of the nanobeam resonator to block the phonon radiation to the environment and cooling down to cryogenic temperature to reduce thermal phonon scattering. Those nanomechanical resonators has small footprint, large optomechanical coupling rate (due to small mode volume) and longest phonon lifetime (to date). However, the coherence time (~ 130 μs) is found less than the lifetime by four orders of magnitude, suggesting a large dephasing rate due to large interaction with surface defects. Moreover, the heating is another a big issue in this type of resonators and limits the optical power it can handle. To avoid the strong dephasing by the surface, one has to reduce the surface participation of the phonon mode. In this sense, bulk phonons seem to be a better option.

In contrast to these nanomechanical resonators, bulk acoustic-wave (BAW) resonators use two surfaces of a crystalline substrate as mirrors to form a Fabry-Perot (FP) cavity for phonons. As we know, to form a stable cavity, one surface needs to be convex (thus concave to the phonons). In these BAW resonators, phonons mostly propagate inside the bulk crystal and only get reflected at the surfaces. Bulk phonons have huge potential as their dissipation drops down as T^6 for longitudinal waves or T^4 for shear waves at cryogenic temperatures according to Landau-Rumer theory [23–27]. In experiment, 8 billion Qs have been demonstrated in these BAW

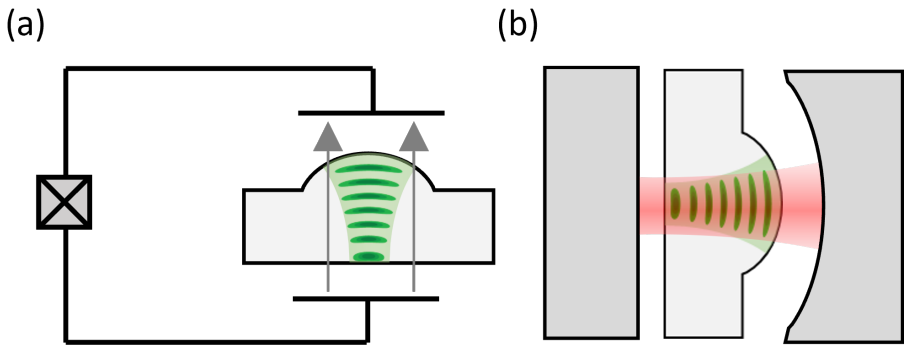

Figure 1.1: Two coupling schemes to HBAR phonons. (a) Piezoelectric coupling to superconducting qubit. (b) Optomechanical coupling to photon.

resonators for high-overtone phonon modes (200 MHz) [27]. These high-overtone bulk acoustic resonators (HBAR) will be the focus of this thesis. Next, I will introduce ways to control and measure gigahertz phonon modes in the HBARs.

So far, there have been two main approaches to manipulating HBARs: electromechanically and optomechanically (Fig. 1.1). The first approach utilizes the piezoelectric interaction between electric fields and strain fields in crystalline materials with no inversion symmetry. It generally has larger interaction than optomechanical interaction. In the past, people have successfully used superconducting quantum circuits to manipulate and measure phononic resonators via piezoelectricity, which gives birth to the field of circuit quantum acoustodynamics (cQAD) [7–9]. However, the requirement of no inversion symmetry limits the materials we can choose and rules out many promising high-purity crystals such as silicon and diamond. The second approach takes advantage of the optomechanical interaction. Optomechanical interaction in bulk materials can be divided into electrostriction and photoelastic effect [28, 29]. When light is incident into a medium, it triggers a strain modulation of the medium via electrostriction, which is proportional to the intensity of the electric fields. Then the strain modulation in return alters the local permittivity via photoelastic effect, which will later modulate the displacement field of light. In history, this interaction was first observed in fibers, as demonstration of a 3rd-order nonlin-

ear optical effect called stimulated Brillouin scattering (SBS) [29–31]. Two coherent counter-propagating laser beams with slightly different frequencies are incident into the medium and create a traveling intensity beat note. This traveling beat drives an acoustic wave via electrostrictive if the frequency difference between the two laser beams matches with the Brillouin frequency of the material. Then the acoustic wave will modulate the local refractive index which, as a moving Bragg grating, will in return scatter the photons from one frequency to the other. Overall, it results in a resonant energy transfer from the high-frequency photons to the low-frequency photons and the low-frequency photons will experience a resonant SBS gain. The resonant spectrum of the SBS gain then reflects the coherence of the acoustic waves (phonons) that are generated in the SBS process.

Phonon coherence is generally limited by the energy dissipation (i.e. phonon loss) and pure dephasing. There are various phonon loss mechanisms that can cause phonon dissipation, such as impurity scattering, thermal phonon scattering, lattice defects and disorders. Recently, large discrepancy between the phonon coherence time and lifetime revealed significant pure dephasing in these nanomechanical resonators, due to large interaction between phonons and the so-called two-level systems (TLS) associated with surfaces [19, 32, 33]. Generally speaking, thermal phonon scattering loss can be mitigated by cooling the device down to a few Kelvin or even milli-Kelvin temperatures. Impurity scattering sets a requirement for the crystal quality. However, as you will see in this thesis in Chapter 4 and 5, various contamination and lattice distortion can happen during the manufacturing and fabrication. Fabrication, measurement of the µHBAR devices and figuring out the dominant sources of the phonon loss are the main body of this thesis.

In this thesis, I will talk about the fabrication of the µHBAR devices. I will also introduce a novel laser-based spectroscopy technique based on the SBS effect to measure the spectrum and ring-down of phonon modes in µHBARs. At end end, I will investi-

gate the dominating sources of phonon loss using powerful material characterization tools and treatments. Combining all these technical advances, we finally unlocked ∼10-ms coherence time with > 10-GHz phonons and achieved a record-setting f-Q product. The rest of the thesis is structured in the following way:

- **Chapter 2:** µHBAR. This chapter introduces the basic concept of µHBAR. I discuss about the acoustic wave propagation theory in an anisotropic crystal like quartz and Gaussian beam theory. These theories provide a solid background for understanding phonon modes in a µHBAR device. Then I explained the fabrication recipe and key details to achieve high-coherence resonators. At last, I developed an eigenmode solver to model both acoustic and optical FP resonators with irregular mirror shapes. Taking the input of the real mirror profile, this eigenmode solver can calculate the mode profiles, mode frequencies, as well as geometric losses of the irregular FP resonators.

- **Chapter 3:** Measurement. In this chapter, I will introduce a novel laser-based spectroscopy technique that utilizes the optomechanical interaction to measure the phonon coherence and lifetime of the µHBAR devices. This technique is based on SBS effect and provides an efficient and noninvasive way to characterize the fabricated µHBARs. I will fully lay out the theory behind it and share some key experimental details to guarantee consistent results.

- **Chapter 4:** Main result. This chapter talks about the main measurements of phonon spectra and ring-down. To figure out the limiting factors of phonon coherence, we performed temperature sweeps and measured multiple devices with a series of difference thicknesses. In the last section, I give a detailed analysis of the phonon coherence and relevant limiting factors.

- **Chapter 5:** Surface/subsurface damage remediation and Q improvement. This chapter focuses on the surface/subsurface damages which proves to be the dom-

inating phonon loss sources in our µHBAR systems. It turns out those damages are unavoidable in the crystalline substrates received from the vendor. Therefore, powerful and reliable characterization tools and remediation methods are necessary to build high-coherence resonators. I will show you how we tackle these problems and finally reach record-high coherence times and f-Q products in our µHBAR devices.

- **Chapter 6:** Conclusion and outlook. In the last chapter, I brief summarize the lessons we learned along the way of building µHBARs with record-setting coherence times and the potential application in quantum acoustics reserach.

Chapter 2

Micro-fabricated high-overtone bulk acoustic resonator (μHBAR)

2.1 Solution of bulk acoustic modes in z-cut quartz

In this section, I will introduce the Christoffel equation that dictates the propagation of acoustic waves in z-cut (i.e. c-axis) quartz and its plane wave solutions, which will be the basis for more complex phonon mode studies. Generally speaking, the propagation of acoustic waves obeys the Christoffel equation in an anisotropic medium,

$$\rho \frac{\partial^2 u_i}{\partial t^2} = c_{ijkl} \frac{\partial^2 u_l}{\partial x_j \partial x_k}, \tag{2.1}$$

where ρ is the density, u_i is the displacement field, c_{ijkl} is the stiffness tensor, and $i, j, k, l = x, y, z$. In matrix form with abbreviated subscripts, this is

$$\rho \frac{\partial^2 u_i}{\partial t^2} = \nabla_{iK} c_{KL} \nabla_{Lj} u_j, \tag{2.2}$$

where $K, L = 1, 2, ...6$ and the matrix-differential operators are defined as

$$\nabla_{iK} = \begin{bmatrix} \partial_x & 0 & 0 & 0 & \partial_z & \partial_y \\ 0 & \partial_y & 0 & \partial_z & 0 & \partial_x \\ 0 & 0 & \partial_z & \partial_y & \partial_x & 0 \end{bmatrix}, \nabla_{Lj} = \begin{bmatrix} \partial_x & 0 & 0 \\ 0 & \partial_y & 0 \\ 0 & 0 & \partial_z \\ 0 & \partial_z & \partial_y \\ \partial_z & 0 & \partial_z \\ \partial_y & \partial_x & 0 \end{bmatrix}. \tag{2.3}$$

As for α-quartz crystal, which has a trigonal lattice structure, its stiffness tensor (symmetric) is

$$c \text{ (symmetric)} = \begin{bmatrix} c_{11} & c_{12} & c_{13} & c_{14} & 0 & 0 \\ & c_{11} & c_{13} & -c_{14} & 0 & 0 \\ & & c_{33} & 0 & 0 & 0 \\ & & & c_{44} & 0 & 0 \\ & & & & c_{44} & c_{14} \\ & & & & & c_{66} \end{bmatrix}, \tag{2.4}$$

where $c_{66} = (c_{11} - c_{14})/2$ and the stiffness constants are shown in Table 2.1. Then

Stiffness constant	c_{11}	c_{12}	c_{13}	c_{14}	c_{33}	c_{44}
Value (GPa)	86.6	6.7	12.4	17.8	106.4	58.0

Table 2.1: Stiffness tensor constants of α-quartz [34].

Eq. 2.2 for the quartz crystal becomes

$$\rho \frac{\partial^2 u_i}{\partial t^2} = \Gamma_{ij}^{\text{quartz}} u_j, \tag{2.5}$$

where Γ^{quartz} is the Christoffel matrix for quartz

$$\begin{bmatrix} c_{11}\partial_x^2 + c_{66}\partial_y^2 + c_{44}\partial_z^2 + 2c_{14}\partial_y\partial_z & (c_{12}+c_{66})\partial_x\partial_y + 2c_{14}\partial_x\partial_z & (c_{13}+c_{44})\partial_x\partial_z + 2c_{14}\partial_x\partial_y \\ (c_{12}+c_{66})\partial_x\partial_y + 2c_{14}\partial_x\partial_z & c_{66}\partial_x^2 + c_{11}\partial_y^2 + c_{44}\partial_z^2 - 2c_{14}\partial_y\partial_z & (c_{13}+c_{44})\partial_y\partial_z + c_{14}(\partial_x^2 - \partial_y^2) \\ (c_{13}+c_{44})\partial_x\partial_z + 2c_{14}\partial_x\partial_y & (c_{13}+c_{44})\partial_y\partial_z + c_{14}(\partial_x^2 - \partial_y^2) & c_{44}(\partial_x^2 + \partial_y^2) + c_{33}\partial_z^2 \end{bmatrix} \tag{2.6}$$

Consider a uniform plane wave $u_0 e^{i(k\cdot\hat{l}\cdot\vec{r}-\omega t)}$ propagating along the direction

$$\hat{l} = \hat{x}l_x + \hat{y}l_y + \hat{z}l_z. \tag{2.7}$$

In this case, the Christoffel Eq. 2.5 turns into

$$\Gamma_{ij}u_j = \rho(\omega/k)^2 u_i, \tag{2.8}$$

where Γ is expressed by

$$\Gamma = \begin{bmatrix} c_{11}l_x^2 + c_{66}l_y^2 + c_{44}l_z^2 + 2c_{14}l_yl_z & (c_{12}+c_{66})l_xl_y + 2c_{14}l_xl_z & (c_{13}+c_{44})l_xl_z + 2c_{14}l_xl_y \\ (c_{12}+c_{66})l_xl_y + 2c_{14}l_xl_z & c_{66}l_x^2 + c_{11}l_y^2 + c_{44}l_z^2 - 2c_{14}l_yl_z & (c_{13}+c_{44})l_yl_z + c_{14}(l_x^2 - l_y^2) \\ (c_{13}+c_{44})l_xl_z + 2c_{14}l_xl_y & (c_{13}+c_{44})l_yl_z + c_{14}(l_x^2 - l_y^2) & c_{44}(l_x^2 + l_y^2) + c_{33}l_z^2 \end{bmatrix}. \tag{2.9}$$

Solving the Christoffel equation now becomes an eigenvalue problem. Γ solely depends on the propagation direction, whose eigenvalue determines the sound speed ($v_{\text{ph}} = \omega/k$) and the eigenvector determines the displacement field (the acoustic polarization). Assuming the wave is propagating along z direction, i.e. $\hat{l} = \hat{z}$, Eq. 2.8 becomes

$$k^2 \begin{bmatrix} c_{44} & 0 & 0 \\ 0 & c_{44} & 0 \\ 0 & 0 & c_{33} \end{bmatrix} \begin{bmatrix} u_x \\ u_y \\ u_z \end{bmatrix} = \rho\omega^2 \begin{bmatrix} u_x \\ u_y \\ u_z \end{bmatrix}. \tag{2.10}$$

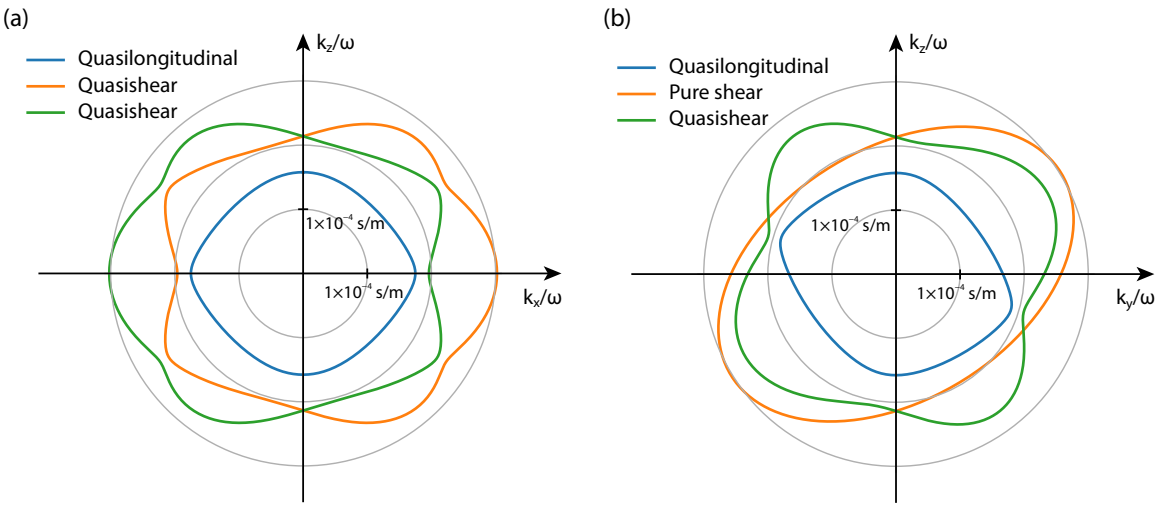

Figure 2.1: Slowness surface of z-cut quartz. (a) Slowness surface in XZ plane. (b) Slowness surface in YZ plane.

Three eigenvectors can be found from the Christoffel matrix, corresponding to three bulk phonon modes. One has a polarization parallel to the propagation direction, called longitudinal phonon mode, and its speed is $\sqrt{c_{33}/\rho}$. The other two have a polarization perpendicular to the propagation direction, called the transverse phonon mode, and share the same speed of $\sqrt{c_{44}/\rho}$. By plotting the inverse of the phonon speed (slowness) versus all possible propagation directions, we obtain the slowness surface. Fig.2.1 shows the slowness surface in XZ and YZ plane for z-cut quartz. As you will see later in Chapter 3, the phonon modes to which we will optomechanically couple are longitudinal phonon modes.

2.2 Gaussian modes of a quartz μHBAR

The μHBAR resembles the FP cavity for laser optics in many aspects. To make a high-quality FP cavity, one needs highly reflective mirrors and stable geometry. Because of the large acoustic impedance mismatch between a crystal and air, the crystal surface naturally forms a highly reflective mirror for phonons with negligible transmission. Just like in the optical cavity, the shapes of the acoustic cavity mirrors,

i.e. the crystal surfaces, need careful design to host stable phonon modes. It is well-known that the eigenmodes of a stable FP cavity are Hermite-Gaussian modes. In this section, I will derive the acoustic version of the Hermite-Gaussian modes from Christoffel Eq. 2.2.

As one can see from Eq. 2.5 and Eq. 2.6, the dynamics of different polarizations of the displacement field are coupled together by the stiffness tensor, making it more complicated than the optical field. Consider a monochromatic acoustic field primarily propagating along the z-direction. Since the diffraction terms ($c_{44}\partial_x^2, c_{44}\partial_y^2$) are symmetric about the z-direction, for simplicity, we only consider a 2D acoustic beam propagating in xz plane (i.e. ignore terms related to the displacement u_y). Then the coupled equations of motion become

$$\begin{aligned}\frac{\partial^2 u_x}{\partial t^2} &= v_{lx}^2\frac{\partial^2 u_x}{\partial x^2} + v_t^2\frac{\partial^2 u_x}{\partial z^2} + \gamma^2\frac{\partial^2 u_z}{\partial x \partial z},\\ \frac{\partial^2 u_z}{\partial t^2} &= v_{lz}^2\frac{\partial^2 u_z}{\partial z^2} + v_t^2\frac{\partial^2 u_z}{\partial x^2} + \gamma^2\frac{\partial^2 u_x}{\partial x \partial z},\end{aligned} \tag{2.11}$$

where $v_{lx} = \sqrt{c_{11}/\rho}$ is the longitudinal phonon speed along x-direction,$v_{lz} = \sqrt{c_{33}/\rho}$ is the longitudinal phonon speed along z-direction, and $\gamma = \sqrt{(c_{13}+c_{44})/\rho}$ represents the coupling between u_x and u_z. Consider a monochromatic longitudinal wave propagating along the z-direction $\vec{u}(x,z) = [\hat{x}A_x(x,z) + \hat{z}A_z(x,z)]e^{i(kz-\Omega t)}$, where $\Omega = k\cdot v_{lz}$. Using the slowly varying envelope approximation (SVEA), we have $|\partial_z A_{x,z}| \ll |kA_{x,z}|$ and $|\partial_z^2 A_{x,z}| \ll |k^2 A_{x,z}|$. Then Eq. 2.11 becomes

$$\begin{aligned}&v_{lx}^2\,\partial_x^2 A_x + 2ikv_t^2\,\partial_z A_x + ik\gamma^2\,\partial_x A_z = -k^2(v_{lz}^2 - v_t^2)A_x,\\ &v_t^2\,\partial_x^2 A_z + 2ikv_{lz}^2\,\partial_z A_z + ik\gamma^2\,\partial_x A_x = 0.\end{aligned} \tag{2.12}$$

To solve these coupled equations, we Fourier transform $A_{x,z}(x,z)$ to k_x-space. Define $\tilde{A}_{x,z}(k_x,z) = \int_{-\infty}^{\infty} A_{x,z}(x,z)e^{-ik_x x}\,dx$ and then we get the following first-order

differential equations

$$\begin{aligned} \partial_z \tilde{A}_z + ip\tilde{A}_z + iq\tilde{A}_x = 0, \\ \partial_z \tilde{A}_x + ir\tilde{A}_x + is\tilde{A}_z = 0, \end{aligned} \tag{2.13}$$

where $p = k_x^2 v_t^2/2kv_{lz}^2$, $q = k_x\gamma^2/2v_{lz}^2$, $p = -[k^2(v_{lz}^2 - v_t^2) - k_x^2 v_{lx}^2]/2kv_t^2$, and $s = k_x\gamma^2/2v_t^2$. By neglecting the second-order derivative, we finally get

$$\partial_z \tilde{A}_z + i\frac{pr - qs}{p + r}\tilde{A}_z = 0. \tag{2.14}$$

Note that under paraxial approximation, $k_x \ll k$, thus

$$\begin{aligned} \frac{pr - qs}{p + r} &= \frac{\frac{k_x^2 v_t^2}{2kv_{lz}^2} \cdot \frac{k^2(v_{lz}^2 - v_t^2)}{2kv_t^2} + \frac{k_x^2\gamma^4}{4v_{lz}^2 v_t^2} + O(k_x^4)}{\frac{k^2(v_{lz}^2 - v_t^2)}{2kv_t^2} + O(k_x^2)} \\ &= \frac{v_t^2(v_{lz}^2 - v_t^2) + \gamma^4}{2v_{lz}^2(v_{lz}^2 - v_t^2)}\frac{k_x^2}{k} \\ &= \chi\frac{k_x^2}{k}, \end{aligned} \tag{2.15}$$

and above differential equation can be rewritten as

$$2i\chi k\partial_z \tilde{A}_z - k_x^2 \tilde{A}_z = 0. \tag{2.16}$$

Now this looks the same as the paraxial Helmholtz equation for electromagnetic field except for $k' = \chi k$. Here χ is called the anisotropic parameter [28], which accounts for the anisotropic medium. Learning from the solution to paraxial Helmholtz equation, we can directly write down the fundamental acoustic Gaussian mode as

$$\begin{aligned} u_z(x, z) &= \frac{A_0}{q'(z)} \exp\left(i\frac{k'x^2}{2q'(z)}\right) \exp(ikz) \\ &= \frac{A_0}{z - iz'_R} \exp\left(-\frac{x^2}{w'^2(z)} + i\frac{k'x^2}{2R'(z)} + ikz\right) \\ &= A_0\frac{iw_0}{z'_R w'(z)} \exp\left(-\frac{x^2}{w'^2(z)} + i\frac{kx^2}{2R'(z)} - i\zeta'(z) + ikz\right), \end{aligned} \tag{2.17}$$

where

$$k' = \chi k = \frac{2\pi}{\lambda_{\text{ph}}}\chi \text{ for phonon wavelength } \lambda_{\text{ph}},$$

w_0 is the acoustic beam waist at $z = 0$,

$$z'_R = \frac{1}{2}k'w_0^2 = \frac{\pi w_0^2}{\lambda_{\text{ph}}}\chi \text{ is the acoustic Rayleigh length,}$$

$$w'(z) = w_0\sqrt{1 + \frac{z^2}{z'^2_R}} \text{ is the acoustic beam waist at } z,$$

$$R'(z) = \frac{1}{\chi}(z + \frac{z'^2_R}{z}) \text{ is the radius of curvature of the acoustic beam's wavefront at } z,$$

$$\zeta'(z) = \arctan(\frac{z}{z'_R}) \text{ is the acoustic beam's Guoy phase at } z. \tag{2.18}$$

The density of α-quartz ρ is 2650 kg/m^3. Using the stiffness tensor parameters from Table 2.1, we can calculate $v_{lz} = 6336$m/s, $v_{lx} = 5717$m/s, $v_t = 4678$m/s, and $\gamma = 5154$m/s. Thus the anisotropic parameter for z-cut quartz is $\chi = 0.6633$.

2.3 Stability criterion, Gaussian beam waist and transverse mode spacing

Now that we derived the propagation formula for the acoustic beam, we can do a stable FP resonator analysis similar to that of two optical mirrors. As you can see from the Gaussian beam solution (Eq. 2.17), the wavefront of the propagating acoustic beam is spherical near the propagating axis, and its radius of curvature $R'(z)$ is a function of propagation distance z. To form a stable resonator, the shape of each cavity mirror needs to match the wavefront at its position to realize normal reflection. Given two convex spherical surfaces with radius of curvature R_1 and R_2, separated by distance d, let us try to find the Gaussian mode it supports. Assume the Gaussian beam has an unknown waist of w_0 which is located somewhere in the cavity and the two mirrors

are at distance z_1 and z_2 away from it. Then we get

$$\begin{aligned} R'(z_1) &= \frac{1}{\chi}(z_1 + \frac{z_R'^2}{z_1}) = R_1, \\ R'(z_2) &= \frac{1}{\chi}(z_2 + \frac{z_R'^2}{z_2}) = R_2, \\ L &= z_2 - z_1. \end{aligned} \tag{2.19}$$

Define "g-parameter" as $g_{1,2} = 1 - L/\chi R_{1,2}$, and we can find z_1, z_2 and z'_R in terms of g_1, g_2 and L. The Rayleigh length for this trapped Gaussian beam is given by

$$z_R'^2 = \frac{g_1 g_2 (1 - g_1 g_2)}{(g_1 + g_2 - 2g_1 g_2)^2} L^2. \tag{2.20}$$

Since $z_R'^2$ is always nonnegative, g_1 and g_2 have to satisfy $0 \leq g_1 g_2 \leq 1$, which is called the stability criterion of the acoustic FP cavity. The positions of the two spherical surfaces can also be figured out as

$$\begin{aligned} z_1 &= \frac{g_2(1 - g_1)}{g_1 + g_2 - 2g_1 g_2} L, \\ z_2 &= \frac{g_1(1 - g_2)}{g_1 + g_2 - 2g_1 g_2} L. \end{aligned} \tag{2.21}$$

The beam waist w_0 can be calculated from z'_R as

$$w_o = \sqrt{\frac{L\lambda_{\mathrm{ph}}}{\pi\chi}} \left(\frac{g_1 g_2 (1 - g_1 g_2)}{(g_1 + g_2 - 2g_1 g_2)^2} \right)^{\frac{1}{4}}. \tag{2.22}$$

Since all the μ HBARs in this thesis have plano-convex structure (plano-concave for phonons), thus $R_1 = \infty$ and $g_1 = 1$. The stability criterion requires $0 \leq g_2 \leq 1$, i.e. $R_2 \geq L/\chi$ (note that $\chi > 0$ for quartz). Moreover, for this plano-convex structure, $z_1 = 0$ meaning the beam waist lies at the plano surface, and beam waist is $w_0 = \sqrt{\frac{L\lambda_{\mathrm{ph}}}{\pi\chi}} \left(\frac{g_2}{1-g_2} \right)^{\frac{1}{4}} = \sqrt{\frac{\lambda_{\mathrm{ph}}}{\pi\chi}} [L(\chi R_2 - L)]^{\frac{1}{4}}$.

We can also calculate the frequency spacing between different Hermite-Gaussian

modes for this plano-convex μHBAR cavity. Let's first take a look at the frequency spacing between adjacent longitudinal modes, which is also called the free spectral range (FSR). By definition, the adjacent longitudinal modes have 2π phase difference over round-trip propagation, i.e. $\Delta k \cdot L = \pi$, thus the FSR can be calculated by $\Delta\nu = \frac{\Delta k \cdot v_l}{2\pi} = \frac{v_l}{2L}$. The Gaussian beam theory also predicts that except for the fundamental Gaussian modes (Eq. 2.17), there are high-order Hermite-Gaussian modes that are also solutions to the Eq. 2.16, which can be expressed by

$$u(x,z) = A_n H_n(\frac{\sqrt{2}x}{w'(z)}) \exp\left(-\frac{x^2}{w'^2(z)} + i\frac{kx^2}{2R'(z)} - i(n+1)\zeta'(z) + ikz\right). \tag{2.23}$$

Similarly, the adjacent resonances of the higher-order modes are separated by phase of 2π for a round trip, thus $\Delta kL - \zeta'(L) = \pi$. Therefore, the frequency spacing ($\Delta\nu$) between adjacent higher-order modes is given by

$$\Delta\nu = \frac{\Delta k v_l}{2\pi} = \mathrm{FSR} \cdot \frac{1}{\pi} \arctan(\frac{L}{z'_R}). \tag{2.24}$$

Consider a z-cut quartz ($\chi = 0.6633$) μHBAR device whose convex surface has a radius of curvature of 100 mm ($R_1 = \infty, R_2 = 100$ mm). For phonons with 500 nm wavelength, we can calculate the FSR, Rayleigh range (z'_R), mode waists (w_0), and frequency spacings ($\Delta\nu$) of higher-order modes with a series of thicknesses (L) from 0.5 mm to 3.0 mm, as shown in Table 2.2.

L (mm)	0.5	1.0	1.5	2.0	2.5	3.0
FSR (MHz)	6.336	3.168	2.112	1.584	1.267	1.056
z'_R (mm)	5.737	8.083	9.861	11.34	12.63	13.78
w_0 (μm)	37.10	44.04	48.64	52.17	55.05	57.51
$\Delta\nu$ (kHz)	175.3	124.1	101.5	88.00	78.81	72.04

Table 2.2: FSR, Rayleigh range (z'_R), mode waists (w_0), and frequency spacings ($\Delta\nu$) of higher-order modes with a range of thicknesses (L) from 0.5 mm to 3.0 mm.

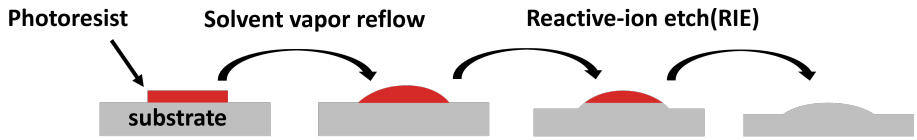

Figure 2.2: Flow chart of the µHBAR fabrication process.

2.4 µHBAR fabrication

Micro-fabrication of these HBARs enables customized designs and quality control of the material. In this section, I will describe a reflow-based technique that was recently developed in this group. The material on which we build the µHBAR is commercial z-cut quartz. The whole fabricated flow is shown in Fig. 2.2.

1. Substrate cleaning

   It is vital to prepare a clean surface before the fabrication. Any dust and dirt on the surface can lead to photoresist peeling off or defects on the fabricated surface. This cleaning procedure itself includes three steps: (i) organic solvent sonication; (ii) Piranha cleaning; (iii) oxygen plasma ashing. We start the cleaning by sonicating the substrate in NMP, acetone, and methanol solvent, for 3 min each. Then we put it in Piranha solution (H2SO4:H2O2=3:1) for 8 min to remove the organic contaminants. After that, the substrate needs to be thoroughly washed with DI water to remove any Piranha residue from the surface. Piranha residue on the substrate surface can lead to a blurry (sticky feeling) image in the atomic force microscope (AFM) measurement. We soak the substrate in DI water right after the Piranha cleaning for 5 min, change water and soak the substrate in for another 5 min, change water and sonicate for 5 min, change water again and sonicate for another 10 min. The last step in the cleaning procedure is oxygen plasma cleaning, which activates the surface for better adhesion to the photoresist. We put the substrate in a plasma asher (AutoGlow 200) and clean it for 1 min at an RF power of 100 W and an oxygen

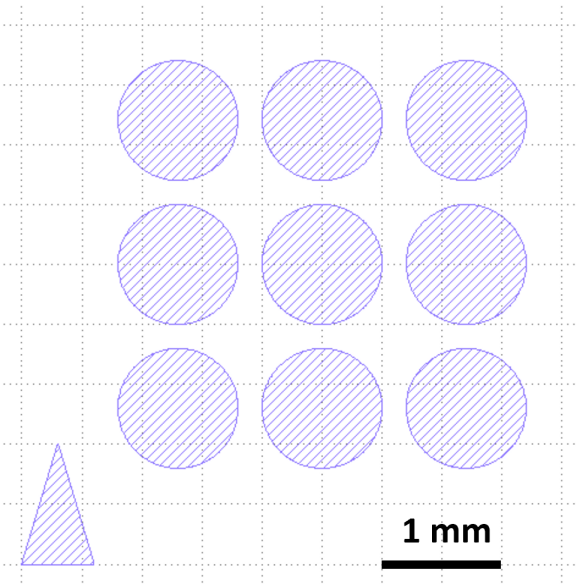

Figure 2.3: GDS pattern design of photoresist. It consists of 3 by 3 disk array, each is 1 mm in diameter. The triangle is the bottom left corner is a marker.

pressure of 300 mTorr.

2. Spin coating of photoresist

   After the cleaning procedure, the substrate is ready for photoresist spin coating. We bake (pre-bake) the substrate at 150 °C for 2 min to eliminate water molecules. The photoresist we use in this fabrication is S1808 (Shiply Microposit S1800 series). The spinning speed is 500 rpm for 10 sec and 2000 rpm for 60 sec, which yields a photoresist thickness of $\sim 1.3\mu$m. Then bake (post-bake) the substrate at 120 °C for 5 min to harden the photoresist a little bit.

3. Optical lithography and developing

   Optical lithography involves exposing the photoresist in ultra-violet (UV) light. Since S1808 is a positive photoresist, anywhere that gets exposed will be washed away in the following developing procedure. The UV exposure is done in a Heidelberg MLA150 maskless aligner with 375-nm laser. Exposing dose is set to be 250 mJ/cm^2. Fig. 2.3 shows the photoresist pattern we use in our fabrication. They are an array of 1-mm-diameter circles with a marker on the bottom left

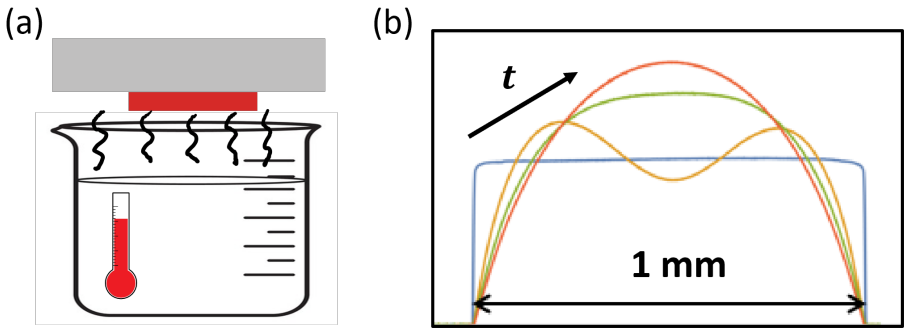

Figure 2.4: (a) Sketch of the reflow setup. (b) Shape change of the photoresist as it reflows.

corner, which will become 1-mm-diameter 1.3μm-high cylinders after developing. We develop the exposed substrate in MF-319 developer for 60 sec. After about 20 sec, we start gently stirring the developer to speed up the dissolution of the photoresist. The substrate needs to be quickly soaked in DI water and rinsed thoroughly after the developing procedure to remove any developer residue.

4. Solvent vapor reflow

This is the most critical step in the fabrication of µHBAR devices. The goal is to turn the cylinder shape of the photoresist into a dome shape. The photoresist is primed with hexamethyldisilizane (HMDS) vapor for 15 min beforehand to preserve the circular base during the reflow. As you can see from the sketch in Fig. 2.4a, the substrate is put on a hot pad at 60 °C and placed upside down (the photoresist side facing down) on top of a beaker of heated solvent but without touch the solvent. The solvent used here is polypropylene glycol monomethyl ether acetate (PGMEA) and the temperature is set as around 55 °C. The hot solvent vapor is then absorbed into the photoresist and softens it. Then, under the effect of surface tension and gravity, the photoresist slowly changes its shape from a cylinder to a dome (Fig. 2.4b). The reflow speed is highly dependent on the temperature difference between the hot pad and the PGMEA solvent

and the spacing between the photoresist and solvent in a very nonlinear way. During our fabrication, the volume of PGMEA solvent is fixed and the solvent temperature needs to be calibrated each time before a formal device fabrication.

5. Reactive ion etching

   After the reflow, the target dome shape is obtained on the photoresist. We then use the reactive ion etching (RIE) to imprint the same shape onto the quartz substrate. Our RIE process uses high-energy SF6 and Ar plasma to remove photoresist and substrate material in a very directional way. Note that the etching rate of photoresist is generally different from that of the substrate material, so the final shape imprinted on the substrate is only the same as the shape on the photoresist within a scaling factor called selectivity. Before we implement the RIE, we need to hard-bake the photoresist. It is done by a series of baking steps: (i) 90 °C for 1 min; (ii) 110 °C for 5 min; (iii) gradually increase the temperature to 130 °C by 5 °C per 30 sec, and stay at 130 °C for 3 min.

   The RIE is done in Oxford Plasmalab 80 Plus. The gas flow rate is 4 sccm for SF6 and 14 sccm for Ar. The chamber pressure is controlled to be 4.5 mTorr and the forward RF power is 150 W, which will gives a DC bias of 430 V. No ICP power is used in this etching process. The sample sits on a 2-inch-diameter fused silica carrier wafer. Thermal paste is used between the carrier wafer and the sample to keep good thermal conduction and avoid burning of the photoresist . The etch time should be optimized each time based on the etch rate and the exact photoresist dome height, to minimize the over-etch duration which can potential harm the substrate surface (See Section 4.4).

It is worth noticing that although we focus on quartz μHBAR devices in this thesis, this reflow-based micro-fabrication technique is in principle applicable to any material.

2.5 Shape control and surface roughness

There are two primary figures of merit for the fabricated µHBAR devices: the shape and the surface roughness. Since the µHBAR device is a plano-convex FP cavity, the shape of the convex surface, together with the substrate thickness, determines the phonon mode volume. The ideal shape of the convex surface is spherical, which is uniquely set by the radius of curvature R and the lateral diameter D. Assume the photoresist cylinder before reflow has a base diameter D and a height h_1. After reflow, it turns into a dome (spherical cap) whose base diameter is still D and height is h_2, as seen in Fig. 2.5. The radius of curvature R can be calculated by $h_2(2R - h_2) = D^2/4$ and the volume of the dome is $V_{\text{dome}} = \pi h_2^2(R - h_2/3)$. In the limit of $h_2 \ll D$, we have $R = D^2/8h_2$ and $V_{\text{dome}} = \pi h_2^2 R = \pi D^2 h_2/8$. We also know that the volume of the photoresist cylinder before reflow is $V_{\text{cyln}} = \pi D^2 h_1/4$. By equating the photoresist volume before and after the reflow, we get $h_2 = 2h_1$, meaning that the height of the dome is twice the height of the photoresist cylinder. After the RIE process, the dome imprinted on the quartz substrate will have the same base diameter D but its height h will be $h = S \cdot h_2$, where S is the etch selectivity of quartz to the photoresist ($S = \frac{\text{Etch rate of quartz}}{\text{Etch rate of the photoresist}}$). At last, we can calculate the radius of curvature of the dome imprinted on the quartz substrate as

$$R_{\text{quartz}} = \frac{D^2}{16Sh_1}. \tag{2.25}$$

From the above formula we can see that the radius of curvature of the final resonator can be largely tuned by the lateral diameter and height of the photoresist. The lateral diameter is set in the pattern design and the height is determined by the type of photoresist and the coating speed during the spin coating procedure. In practice, we have fabricated µHBARs with radius of curvature ranging over 5 order of magnitude ($10^{-5} \sim 1$ m).

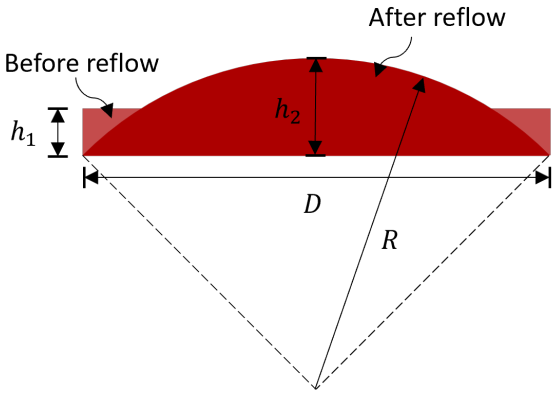

Figure 2.5: Sketch of cross section of the photoresist before and after the reflow process.

Eq. 2.25 shows a simple relation between the final shape of the μHBAR surface and the dimension of the photoresist pattern. However, what comes out of a real fabrication deviates from this ideal spherical dome, thus always has a shape error. Moreover, the surface roughness on the μHBAR surface is closely related to the phonon dissipation due to scattering. These two quantities are the major figures of merits in evaluating a fabrication run. Here we measure the shape error and surface roughness using a 3D optical profilometer (Bruker ContourX-500) which is based on white light interferometry (WLI). Since the wavelength of target phonons in this study is 500 nm, this WLI-based profilometer provides enough lateral resolution to capture detailed surface structures. The quartz substrate we use is half-inch large and a few millimeter ($0.5 \sim 3$ mm) thick. Fig. 2.6a shows the surface profile of a typical 3×3 μHBAR array, each dome has a diameter of 1 mm and height of 1.3 μm. The parabolic fitting shows a radius of curvature of 100 mm (Fig. 2.6b). At last, a zoomed-in image using a 50× objective reveals a surface roughness of 0.25 nm within a field of view of 80×60 μm (Fig. 2.6c).

The surface roughness is an important figure in this study, as it directly affects the phonon scattering. Assuming the surface height profile as the a random variable that obeys Gaussian distribution with variance σ and zero correlation (white noise),

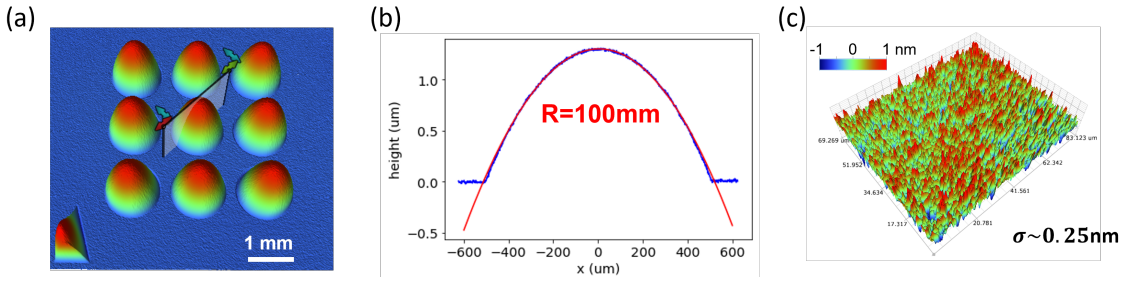

Figure 2.6: µHBAR surface measured by 3D optical profilometer. (a) Surface profiles of 9 µHBAR devices. The triangle in the bottom left corner is a marker. (b) Cross section of the central µHBAR shows a parabolic shape and a radius of curvature of 100 mm. (c) A zoomed-in image of 80 by 60 μm shows the surface roughness is 0.25 nm.

the reflectivity R can be expressed by $R = e^{-(2k\sigma)^2}$ [27]. Therefore, the phonon scattering loss per reflection is $l = 1 - R \approx (\frac{4\pi\sigma}{\lambda_{\text{ph}}})^2$, where the λ_{ph} is the phonon wavelength. Given $\sigma = 0.25$ nm and $\lambda = 500$ nm, the phonon loss per reflection is 40 part-per-million (ppm).

2.6 Acoustic eigenmode solver

Our µHBAR is essentially a FP cavity for acoustic waves. The Christoffel equation and Gaussian beam theory provides a theoretical background of understanding the phonon modes supported by an ideal plano-spherical cavity. However, in practice the fabricated convex surface always have some shape error, i.e. deviation from a perfect sphere. Oh the other hand, the surface is never perfectly smooth. Understanding how these imperfections of the geometry affect the phonon mode profile and phonon loss is of great importance to make high-coherence µHBARs. Moreover, our reflow-based fabrication technique opens the possibility of engineering surfaces with a range of geometries that no longer conform to the conventional paradigm of Gaussian beam resonators (i.e. with spherical mirrors and analytically solvable modes). While this myriad of possible mirror geometries brings new opportunities for mode engineering (design of shape and mode spectrum), it also brings questions about the optimal

mirror shape as we seek to push mirror to new extremes of performance. Overall, it is a nontrivial task to predict mode spectra, mode shapes, and cavity finesse using these non-standard mirror geometries. To fully utilize the opportunities offered by these μHBAR devices, we will require new simulation methods.

The dimensions of our μHBARs are at millimeter level, making it impractical to use FEM or FDTD methods which are widely used for calculating eigenmodes in micron-scale integrated photonic/phononic devices. Different techniques have been developed over the decades to model large optical FP cavities. Scalar-field-based beam propagation methods have been used to calculate the modes of stable FP resonators [35]. Scalar-field eigenmode analysis by Kleckner *et al.* [36] has also been shown to be very effective at predicting the mode shape and mode losses by casting the mirror reflection in the form of a scattering matrix which is then used to compute the eigenmodes of the system. In this section, I will introduce a hybrid technique that combines a Fourier beam propagation method and eigenmode analysis, and can predict eigenmode profiles, frequencies, and geometric losses (i.e. due to mirror clipping and surface scattering) of acoustic FP cavities with arbitrary mirror shapes. Moreover, as the optical wave obeys the same type equation of propagation (only simpler because lack of anisotropy), the algorithm easily applies to solving the eigenmodes of optical FP cavities as well.

2.6.1 The mode-mixing matrix and eigenmode analysis

The algorithm of our eigenmode solver is similar to a work presented by Kleckner *et al.* [36], which runs significantly faster than the famous Fox-Li approach. Consider a wave field $|\psi_A\rangle$ that propagates inside a plano-concave FP cavity (acoustic or optical) of length L. As you can see from Fig. 2.7a, it starts from mirror A ($|\psi_A\rangle$), propagates from mirror A to mirror B ($|\psi_B\rangle$), gets reflected by mirror B ($|\psi'_B\rangle$), propagate back to mirror A ($|\psi''_B\rangle$), gets reflection by mirror A ($|\psi'_A\rangle$) and repeats the process again.

Two mirror reflections and two propagations over distance of L make one round-trip propagation. Define the propagation operators and reflection operators as shown in Fig. 2.7b, i.e.

$$|\psi_B\rangle = \hat{P}_{A\to B}|\psi_A\rangle, \tag{2.26}$$

$$|\psi''_B\rangle = \hat{P}_{B\to A}|\psi'_B\rangle, \tag{2.27}$$

$$|\psi'_B\rangle = \hat{R}_B|\psi_B\rangle, \tag{2.28}$$

$$|\psi'_A\rangle = \hat{R}_A|\psi''_B\rangle. \tag{2.29}$$

Propagation operator $\hat{P}_{A\to B}$ ($\hat{P}_{B\to A}$), has to do with the propagation in the bulk medium (or vacuum for optical fields). For acoustic waves propagating in a bulk crystal, it is determined by the crystal orientation, slowness dispersion (set by the Christoffel equation) and the propagation length. The reflection operator $\hat{R}_A$ ($\hat{R}_B$) is determined by the mirror shape and roughness. All the geometric information of the FP cavity is encoded into the propagation and reflection operators. More details will be discussed in Section 2.6.2. Overall, after one round of propagation, the wave field can be written as

$$|\psi'_A\rangle = \hat{R}_A\hat{P}_{B\to A}\hat{R}_B\hat{P}_{A\to B}|\psi_A\rangle = \hat{M}|\psi_A\rangle, \tag{2.30}$$

where $\hat{M}$ is referred to as the mode-mixing matrix.

To efficiently represent the intracavity wave field, we need a pick up an orthonormal basis to build a Hilbert space. For FP cavity with mirror shapes that are nearly spherical, Hermite-Gaussian (HG) mode basis $\{|\phi_0\rangle, |\phi_1\rangle, |\phi_2\rangle,...\}$ is typically a good choice. Assume that we set frequency Ω_o and waist w_o for the HG basis. In practice, we can choose the mode waist such that it gives the closest wavefront to the end

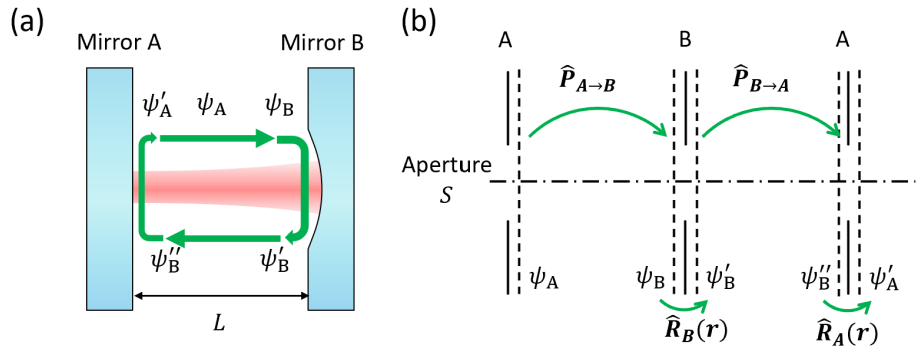

Figure 2.7: Scheme of the Eigenmode Solver. (a) Sketch of a plano-concave FP cavity of length L. The field amplitude ψ_A becomes ψ'_A after one round trip of propagation. (b) The round trip of propagation can be divided into four steps: light propagating from mirror A to mirror B (depicted by operator $\hat{P}_{A\to B}$), reflection from mirror B (depicted by $\hat{R}_B$), propagating from mirror B to mirror A (depicted by operator $\hat{P}_{B\to A}$), reflection from mirror A (depicted by $\hat{R}_A$).

mirror B. Once we adopt the HG basis, any wave field $|\psi\rangle$ can be expressed as

$$|\psi\rangle = \sum_j a_j |\phi_j\rangle, \tag{2.31}$$

and the mode-mixing matrix $\hat{M}$ can be expressed by

$$\hat{M}_{ij} = \langle\phi_i|\hat{M}|\phi_j\rangle. \tag{2.32}$$

To find the eigenmodes of the FP cavity is equal to find the wave field $|\psi\rangle$ such that after one round-trip propagation, we have $|\psi'\rangle = \gamma|\psi\rangle = \hat{M}|\psi\rangle$. Under the representation of the HG basis, we have

$$\hat{M}_{ij}\nu_j = \gamma\nu_i. \tag{2.33}$$

Now clearly it becomes a eigenvalue problem. The eigenmode of the FP cavity is represented by the eigenvalue of the mode-mixing matrix $\hat{M}$ and γ is the eigenvalue.

Let's take a look at some properties of γ. Firstly, since intensity $I' = |\langle\psi'|\psi'\rangle|^2 =$

$|\gamma|^2|\langle\psi|\psi\rangle|^2 = |\gamma|^2 I$, if there is no energy input from outside of the cavity, $|\gamma| \leq 1$. For a lossless system, $\hat{M}$ is unitary and $|\gamma| = 1$. But in practice, we always have $|\gamma| < 1$, indicating some energy loss of the FP cavity. With that said, $\delta = 1 - |\gamma|^2$ indeed captures the fractional energy loss of the wave field oer round-trip propagation. Therefore, the finesse of the cavity is then $F = 2\pi/\delta$ in the limit of $\delta \ll 1$.

The phase angle $\arg\{\gamma\}$ contains important information as well. It represents the phase shift of $|\psi\rangle$ after a round-trip propagation. The resonant condition requires that phase shift of a resonant mode after one round-trip propagation should be multiple times of 2π. Thus for the resonant modes, $\arg\{\gamma\}$=0. Generally, the eigenvalue of the mode-mixing matrix is complex. This is because the wavelength you set for the HG mode basis is generally not on resonance. The phase angle $\arg\{\gamma\}$ gives direct information about the detuning of the resonant frequency with respect to the preset frequency as

$$\Omega = \Omega_o + \mathrm{FSR} \cdot \arg\{\gamma\}. \tag{2.34}$$

At last, the eigenmode profile can be fully reconstructed from the eigenvector $\vec{\nu}$, as $|\psi\rangle = \sum_i \nu_i |\phi_i\rangle$.

2.6.2 Fourier beam propagation (FBP)

From Section 2.6.1, we see that the key step of the eigenmode solver is to construct the mode-mixing matrix which represents the mode-mixing operator $\hat{M}$. The mode-mixing operator is uniquely determined by the propagation operator and reflection operator.

Here I introduce the so-called Fourier beam propagation (FBP) method which features the Fast Fourier Transform (FFT) algorithm. As discussed in Section2.1, the acoustic wave propagation in an anisotropic medium is dictated by the Christoffel equation 2.2. Consider a monochromatic vector field $\vec{u}(\vec{r}, t) = \vec{\psi}(x, y, z)e^{-i\Omega t}$. In the

most general form, it can be expressed in k-domain as

$$\vec{\psi}(x,y,z) = (\frac{1}{2\pi})^3 \iiint_{-\infty}^{\infty} d^3k \cdot \hat{d}(k_x,k_y,k_z)\phi(k_x,k_y,k_z)\exp[i(k_x x+k_y y+k_z z)], \quad (2.35)$$

where $\hat{d}$ is the polarization and ϕ is the Fourier component. Since any propagating acoustic field has to be a solution of the Christoffel equation 2.2, $\{k_x,k_y,k_z\}$ are not independent variables. Instead, given $\{k_x,k_y\}$, k_z only has 3 options as $k_z^i(k_x,k_y)(i=1,2,3)$, corresponding to 3 phonon branches as shown in Fig. 2.1. The polarization also has 3 options as determined by the eigenvectors of the Christoffel matrix. Therefore, the field can be expressed by

$$\vec{\psi}(x,y,z) = (\frac{1}{2\pi})^2 \iint_{-\infty}^{\infty} dk_x k_y \cdot \sum_{i=1}^{3} \hat{d}^i(k_x,k_y)\phi^i(k_x,k_y)\exp[i(k_x x+k_y y+k_z^i z)]. \quad (2.36)$$

If we only consider one phonon branch, say the longitudinal phonon, then it can be simplified to

$$\vec{\psi}(x,y,z) = (\frac{1}{2\pi})^2 \iint_{-\infty}^{\infty} dk_x k_y \cdot \hat{d}(k_x,k_y)\phi(k_x,k_y)\exp[i(k_x x + k_y y)] \cdot e^{k_z z}. \quad (2.37)$$

At $z=0$,

$$\vec{\psi}(x,y,0) = (\frac{1}{2\pi})^2 \iint_{-\infty}^{\infty} dk_x k_y \cdot \hat{d}(k_x,k_y)\phi(k_x,k_y)\exp[i(k_x x + k_y y)]. \quad (2.38)$$

Hence, the wave field at $z=L$ can be calculated by

$$\begin{aligned} \vec{\psi}(x,y,L) &= (\frac{1}{2\pi})^2 \iint_{-\infty}^{\infty} dk_x k_y \cdot \hat{d}(k_x,k_y)\phi(k_x,k_y)\exp[i(k_x x + k_y y)] \cdot e^{k_z L} \\ &= e^{k_z L} \cdot \iint_{-\infty}^{\infty} \vec{\psi}(x,y,0)dxdy. \end{aligned} \quad (2.39)$$

From the above equation, we can see that the propagation has a simpler form in k-domain, just multiplied by $e^{k_z L}$. In the limit of paraxial beam, the polarization's

divergence is negligible (i.e. $\hat{d}(k_x, k_y) = \hat{d}(0,0)$) and we can replace the vector field with a scalar one $\psi(x, y, z)$. Therefore, for the longitudinal phonons, the propagation operator $\hat{P}_L$ over distance L can be calculated by

$$\psi(x, y, L) = \hat{P}_L \psi(x, y, 0) = F^{-1}\{F\{\psi(x, y, 0)\} \cdot e^{k_z L}\}, \tag{2.40}$$

where $F\{\cdot\}$ is the 2D Fourier transform in space.

The reflection operator $\hat{R}$ is more straightforward. The reflected field is simply the incident field multiplied by a complex factor, i.e.

$$\psi_{\mathrm{R}}(x, y, z) = \hat{R}\psi(x, y, z) = \psi(x, y, z) \cdot re^{2ik \cdot \Delta(x,y)}, \tag{2.41}$$

where r is the mirror's reflection coefficient and $\Delta(x, y)$ is its height profile with respect to center point, positive if it aligns with the propagation direction of the incident wave, negative if opposite to the propagation direction. For phonon waves propagating inside the plano-convex µHBARs, the phonon leaked out of the crystal is essentially zero, i.e. $|r| = 1$. For the reflection from the convex surface, $\Delta < 0$.

By combining both the propagation operators and reflection operators, we can now calculate the mode-mixing operator as shown in Eq. 2.6.1. As discussed before, the surface profiles of both mirrors are measured by an optical profilometer and sent into the eigenmode solver via Δ. If both mirrors have ideal shapes that match with the acoustic wavefront and zero roughness, it is a lossless system. The mode-mixing operator will be the unit operator and the eigenmodes are simply the HG modes. If we introduce a little bit of shape errors (well-confined transverse k-vector), the mode-mixing operator will not be unit operator anymore and cause mode-mode mixing in the HG basis. Even so, if the mirror aperture is sufficiently large, the mode-mixing operator will be unitary and it is still a lossless system. Only the eigenmodes will be modified and are not no longer the HG modes. However, if there

is surface roughness on the mirrors, just as in any physical case, the reflected wave field will contain transverse k-components large enough (because surface roughness is generally considered as wide-band noise) to cause a fraction of the wave leaking outside of the cavity. This fractional energy loss is modeled by adding an absorbing window artificially on the side wall of the FP cavity.

Chapter 3

Coherent anti-Stokes Brillouin spectroscopy (CABS) and phonon ring-down

3.1 Stimulated Brillouin scattering

Stimulated Brillouin scattering (SBS) is a nonlinear optical effect that results from the interaction between the light and traveling acoustic waves, i.e. light-sound coupling. It is called *stimulated* because the phonons are produced by the light waves. There are two major schemes to realize stimulated Brillouin scattering. One is the so-called forward SBS (Fig. 3.1a), which involves two co-propagating optical waves. The other is the backward SBS (Fig. 3.1b), which involves two counter-propagating optical waves. In order to satisfy the phase matching condition, acoustic wave guidance is generally required to achieve forward SBS, which makes it not suitable for our bulk crystal system.

The backward SBS is schematically illustrated in Fig. 3.1b. There are two incident counterpropagating laser beams, one of pump frequency ω_{p} and the other of

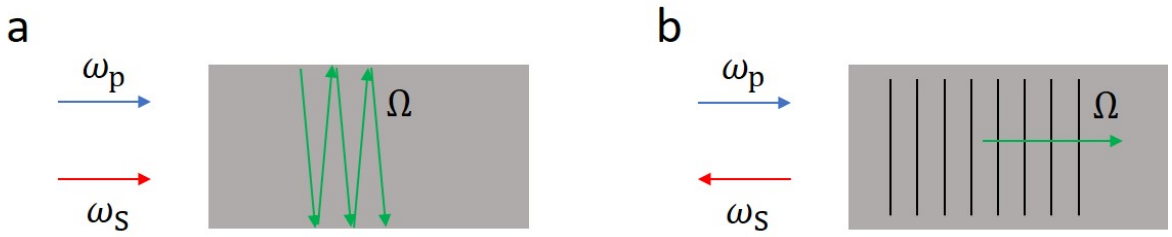

Figure 3.1: (a) Schematic of forward SBS. Pump and Stokes light travel in the same direction. The driven acoustic wave typically have large transverse k-vector and it requires transverse confinement. (b) Schematic of backward SBS. Pump and Stokes light travel in the opposite direction. The driven acoustic wave travels in the direction of the pump light (higher frequency). It can happen in any bulk material.

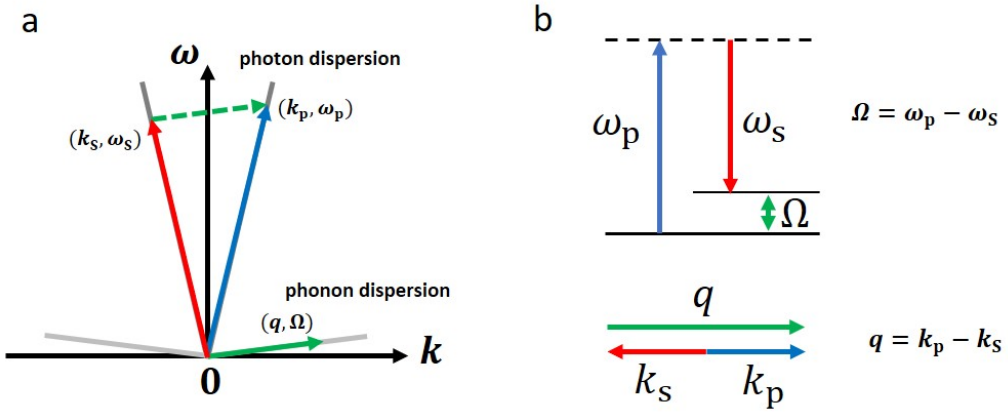

Figure 3.2: (a) Dispersion relation of optical and acoustic fields. (b) Energy and momentum conservation in SBS.

Stokes frequency ω_S. Then the two laser beams will beat with each other and create density and pressure variations at frequency $\Omega = \omega_p - \omega_S$ through a process called electrostriction. In this way, acoustic waves are driven. Those traveling acoustic waves will in return modulate the refractive index, which would scatter more pump light into Stokes light. Under proper circumstances, i.e. the phase matching condition, the positive feedback of these two interactions will lead to the exponential gain of the Stokes wave.

The phase matching condition (Fig. 3.2) basically describes the energy and momentum conservation rules in this process, as they are the fundamental conservation rules in any physical process. Mathematically, it means the following two equations

must be satisfied.

$$\Omega = \omega_{\mathrm{p}} - \omega_{\mathrm{S}} \tag{3.1}$$

$$\vec{q} = \vec{k_{\mathrm{p}}} - \vec{k_{\mathrm{S}}} \tag{3.2}$$

With the linear dispersion relation for both light ($k = n\omega/c$) and sound ($q = \Omega/v_{\mathrm{a}}$), in the backward SBS scheme, we can easily calculate the Brillouin frequency as

$$\Omega_{\mathrm{B}} = 2n\omega_{\mathrm{p}}v_{\mathrm{a}}/c \tag{3.3}$$

where n is the refractive index of the material, v_{a} is the speed of sound and c is the speed of light. Because of the phase matching condition, the acoustic waves will only be excited efficiently when the frequency difference between the pump light and Stokes light ($\omega_{\mathrm{p}} - \omega_{\mathrm{S}}$) gets close enough to the Brillouin frequency (Ω_{B}), at least within the Brillouin linewidth Γ_{B}. This linewidth, which is typically between $2\pi\times$ (10 - 100 MHz), is given by the lifetime of ($\tau_{\mathrm{ph}} = 1/\Gamma_{\mathrm{B}}$).

3.1.1 Low phonon coherence limit

Conventional treatment of the stimulated Brillouin can be found in many standard nonlinear optics textbooks [29, 31]. Here I will give a brief overview of the tradition classical SBS theory. For simplicity, let's treat optical fields as two plane waves $\tilde{E}_1$ (pump) and $\tilde{E}_2$ (Stokes) $\tilde{E}(z,t) = \tilde{E}_1(z,t) + \tilde{E}_2(z,t)$ counter-propagating along z axis, assuming they have the same polarization.

$$\tilde{E}_1(z,t) = \tilde{A}_1(z,t)e^{i(k_1 z - \omega_1 t)} + \text{c.c.} \tag{3.4}$$

$$\tilde{E}_2(z,t) = \tilde{A}_2(z,t)e^{i(k_2 z - \omega_2 t)} + \text{c.c.} \tag{3.5}$$

Similarly, the acoustic field can be represented by the density variation. Because it is driven by the beat of the two optical fields, the acoustic frequency should be around the beat frequency.

$$\tilde{\rho}(z,t) = \rho_0 + [\rho(z,t)e^{i(qz-\Omega t)} + \text{c.c.}] \tag{3.6}$$

where $\Omega = \omega_1 - \omega_2$, $q = 2k_1$ and ρ_0 denotes the mean density of the medium. Here $\rho(z,t)$, representing the envelop of the acoustic field, must vary slowly in space and time, i.e. $|\frac{\partial \rho}{\partial z}| \ll q, |\frac{\partial \rho}{\partial t}| \ll \Omega$. The acoustic field must obey the acoustic wave equation

$$\frac{\partial^2 \tilde{\rho}}{\partial t^2} - \Gamma' \nabla^2 \frac{\partial \tilde{\rho}}{\partial t} - v^2 \nabla^2 \tilde{\rho} = \nabla \cdot \mathbf{f} \tag{3.7}$$

where v is the velocity of sound and Γ' is the damping parameter. While the source term on the right side of the acoustic eave equation consists of the divergence of the force per unit volume $\mathbf{f}$, which is given by

$$\mathbf{f} = -\frac{1}{2}\epsilon_0 \gamma_e \nabla \langle \tilde{E}^2 \rangle \tag{3.8}$$

where ϵ_0 is the vacuum permitivity and γ_e is the relevant electrostrictive constant, defined by $\gamma_e = \rho \frac{\partial \epsilon}{\partial \rho}|_{\rho=\rho_0}$. For the optical fields we consider here, the source term is give by

$$\nabla \cdot \mathbf{f} = -\frac{1}{2}\epsilon_0 \gamma_e \nabla^2 \langle \tilde{E}^2 \rangle = \epsilon_0 \gamma_e q^2 [A_1 A_2^* e^{i(qz-\Omega t)} + \text{c.c.}]. \tag{3.9}$$

Now substitute (Eq. 3.6) and (Eq. 3.9) back into (Eq. 3.7) and with the slow-varying envelop assumption on $\rho(z,t)$ we can obtain the result

$$-2i\Omega \frac{\partial \rho}{\partial t} + (\Omega_{\text{B}}^2 - \Omega^2 - i\Omega\Gamma_{\text{B}})\rho - 2iqv^2 \frac{\partial \rho}{\partial z} = \epsilon_0 \gamma_e q^2 A_1 A_2^* \tag{3.10}$$

where the Brillouin linewidth is introduced $\Gamma_{\text{B}} = q^2\Gamma'$.

Eq. 3.10 looks very hard to solve, but some simplification can be done here.

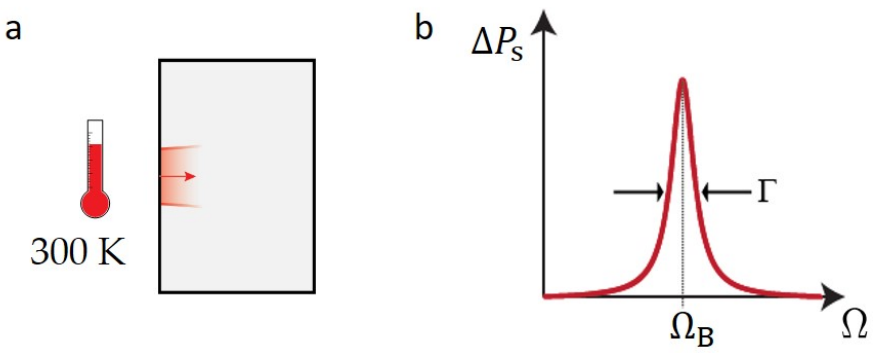

Figure 3.3: Schematics of SBS at low phonon coherence limit. (a) At room temperature, the driven acoustic wave dies off quickly. It cannot propagate to the other surface to form standing mode. (b) Therefore, its spectrum is a wide Lorentzian peak. Spectral linewidth Γ reveals its decoherence rate.

Actually, at most of the time the last term on the left side can be omitted for the following reason. This term describes the propagation phonons. However, phonons generated here have very high frequency ($\sim$ GHz). Usually such hypersonic phonons are strongly damped and thus propagate only over very short distance before being absorbed (see Fig. 3.3). Since the phonon propagation distance is typically way shorter than the distance over which the source term on the right side of (Eq. 3.10) varies significantly, it is conventional to drop the term containing $\frac{\partial\tilde{\rho}}{\partial z}$ in describing SBS. This approximation can break down in cryogenic temperature, as I will discuss in next section, in which the phonons will live so long in the medium and we will observe some exotic phenomenon. If we drop the spatial derivative term and assume steady-state conditions so that $\frac{\partial\tilde{\rho}}{\partial t}$ also vanishes, we find the acoustic amplitude will be given by

$$\rho(z,t) = \epsilon_0\gamma_e q^2 \frac{A_1 A_2^*}{\Omega_B^2 - \Omega^2 - i\Omega\Gamma_B}. \tag{3.11}$$

Next, this acoustic field will polarize the medium, change its refractive index and thus change the way the optical fields propagate. The way how optical field propagates inside a medium is determined by the Maxwell equation. With some algebra, we can

easily get the sourced Helmholtz equation in a nonlinear medium,

$$\frac{\partial^2 \tilde{E}_i}{\partial z^2} - \frac{1}{(c/n)^2}\frac{\partial^2 \tilde{E}_i}{\partial t^2} = \frac{1}{\epsilon_0 c^2}\frac{\partial^2 \tilde{P}_i^{\mathrm{NL}}}{\partial t^2} \quad (i = 1, 2). \tag{3.12}$$

The nonlinear polarization on the right side, which gives rise to the source term, is given by

$$\tilde{P}_i^{\mathrm{NL}} = \epsilon_0 \Delta\epsilon \tilde{E} = \epsilon_0 \rho_0^{-1} \gamma_e (\tilde{\rho} - \rho_0)\tilde{E}. \tag{3.13}$$

The right side contains eight terms, but we only need to pick the ones that can act as phase-matched source terms for the pump and Stokes fields. This procedure is sometimes called rotating-wave approximation (RWA) in some context. Substitute these phase-matched source terms back into (Eq. 3.12), and also with the slow-varying envelop approximation for the optical fields, we can obtain the coupled mode equations

$$\frac{\partial A_1}{\partial z} + \frac{1}{c/n}\frac{\partial A_1}{\partial t} = \frac{i\omega\gamma_e}{2nc\rho_0}\rho A_2, \tag{3.14}$$

$$-\frac{\partial A_2}{\partial z} + \frac{1}{c/n}\frac{\partial A_2}{\partial t} = \frac{i\omega\gamma_e}{2nc\rho_0}\rho^* A_1. \tag{3.15}$$

ρ is give by (Eq. 3.11). If we only consider steady-state solution here, the $\frac{\partial A_1}{\partial t}$ term can be dropped, then it becomes a coupled ordinary differential equation. In order to look at how the light power changes during this SBS process, we define the light power as $P_i = I_i \cdot A_{\mathrm{ao}} = 2n\epsilon c A_i A_i^* \cdot A_{\mathrm{ao}}$, where A_{ao} is the effective acousto-optic interacting area. The the coupled equation for pump and Stokes light power is

$$\frac{dP_1}{dz} = -G_{\mathrm{SBS}} P_1 P_2 \tag{3.16}$$

$$\frac{dP_2}{dz} = -G_{\mathrm{SBS}} P_1 P_2 \tag{3.17}$$

where G_{SBS} is the SBS gain, which to a good approximation can be given by

$$G_{\mathrm{SBS}} = \frac{\gamma_e^2 \omega^2}{nvc^3 \rho_0 \Gamma_{\mathrm{B}} A_{\mathrm{ao}}} \frac{(\Gamma_{\mathrm{B}}/2)^2}{(\Omega_{\mathrm{B}} - \omega)^2 + (\Gamma_{\mathrm{B}}/2)^2}. \tag{3.18}$$

If we assume a stiff pump, i.e. $P_1(z) = \text{constant}$, the solution is quite straightforward,

$$P_2(z) = P_2(L) e^{G_{\mathrm{SBS}} P_1 (L-z)}. \tag{3.19}$$

, In a weak signal gain limit ($G_{\mathrm{SBS}} \ll 1$), the scattered Stokes light power is

$$\Delta P_2 = P_2(0) - P_2(L) = P_2(L) e^{G_{\mathrm{SBS}} P_1 (L-z) - 1} = G_{\mathrm{SBS}} P_1(0) P_2(L) L. \tag{3.20}$$

From the this equation, we can see that the back-scattered Stokes signal has a Lorentzian shape (Fig. 3.3) centered at the Brillouin frequency (Ω_{B}) and has a linewidth (Γ_{B}) determined by the phonon damping inside the medium. Moreover, the height of the signal gain spectrum along with the phonon damping rate can represent the strength of the electrostrictive coupling.

However, as I mentioned before, this conventional treatment assumes the hypersonic phonons die out quickly in the medium, which is not always the case, especially when the crystal is cooled down to cryogenic temperature. The lifetime of the coherent phonons is enlarged and they will propagate over the a distance even longer than the dimension of the crystal. In that case, the coherent phonons will be bounced back and forth for many rounds before they are absorbed. The left and right moving acoustic waves will then form standing waves and create discrete phonon modes. Next I will discuss about the Brillouin scattering in this regime when phonon's coherence length far exceeds the dimension of the crystal.

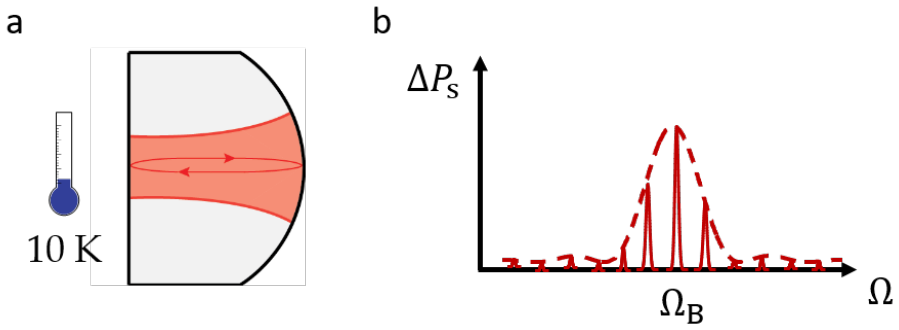

Figure 3.4: Schematics of SBS at high phonon coherence limit. (a) At low temperature, the coherence length of the acoustic wave gets largely extended such that it can propagate to the other surface and form a standing mode. In this way, we can engineer the crystal surfaces to make it a stable FP cavity. (b) Once the cavity phonon mode is formed, its spectrum will be modulated by the cavity resonance. Overall, it looks like a sinc function (determined by the phase matching condition) sampled by a delta comb (cavity resonance). But the delta comb cannot be infinitely sharp. The linewidth of each mode again represents its decoherence rate.

3.1.2 High phonon coherence limit

In the high phonon coherence limit, the acoustic wave will be reflected back and forth from the two surfaces of the diamond crystal before it decays (Fig. 3.4). Therefore, discrete phonon modes are formed. The Brillouin interaction becomes the coupling among two optical fields and several discrete phonon modes. Mathematically, an obvious difference from the conventional treatment of Brillouin interaction in the low phonon coherence limit is that the spatial derivative term of the density variation in (Eq. 3.10) can no longer be neglected. However, it can still be solved. The solution is very similar to (Eq. 3.11) except for a phase-mismatch term, which in some degree explains the spectral shape observed in experiment. However, since we aim to develop a novel optomechanical system, in order to make analogies between our system and conventional cavity optomechanical systems, a Hamiltonian treatment is introduced [28, 37]. Here I'll give a brief view of it.

The total Hamiltonian of a system with acousto-optic interaction can be expressed

as

$$H = H^{\mathrm{ph}} + H^{\mathrm{opt}} + H^{\mathrm{int}} \tag{3.21}$$

where H^{ph}, H^{opt} and H^{int} represent the Hamiltonian of the acoustic field, the optical field and acousto-optic interaction, respectively. For a crystal with length L,

$$H^{\mathrm{ph}} = \sum_m \hbar\Omega_m (b_m^\dagger b_m + \frac{1}{2}) \tag{3.22}$$

$$H^{\mathrm{opt}} = \int_0^L dz\ \hbar(A_{\mathrm{p}}^\dagger \hat{\omega}_{\mathrm{p},z} A_{\mathrm{p}} + \frac{1}{2}) + \int_0^L dz \hbar(A_{\mathrm{S}}^\dagger \hat{\omega}_{\mathrm{S},z} A_{\mathrm{S}} + \frac{1}{2}) \tag{3.23}$$

$$H^{\mathrm{int}} = \sum_m \int_0^L dz\ \hbar g_0^m(z) e^{i\Delta q z} A_{\mathrm{p}}^\dagger A_{\mathrm{S}} b_m + \mathrm{H.c.} \tag{3.24}$$

where $A_j (j = \mathrm{p}, \mathrm{S})$ is the mode amplitude operator over real space for pump and Stokes light respective. b_m is the amplitude operator for the mth acoustic mode. $\Delta q = q_m - k_{\mathrm{p}} - k_{\mathrm{S}}$ represents the phase mismatch among these three fields. $\hat{\omega}_{\mathrm{p},z} = \omega_{\mathrm{p}} - iv_0\partial_z$ and $\hat{\omega}_{\mathrm{S},z} = \omega_{\mathrm{S}} + iv_0\partial_z$, are spatial operators obtained by Taylor expanding the dispersion relations for the optical fields $\omega_{\mathrm{p}}(k)$ and $\omega_{\mathrm{S}}(k)$ in k-space. $g_0^m(z)$ is the single-photon coupling rate that depends on the mode overlaps between the acoustic and optical fields. Knowing the Hamiltonian, it is quite straightforward to write down the Heisenberg equations of motion for all the three fields. Along with the rotating-wave approximation, the following coupled mode equations for the slow-varying envelop operators $(\bar{A}_{\mathrm{p}}, \bar{A}_{\mathrm{S}}, \bar{b}_m)$ of the three fields can be obtained,

$$\partial_t \bar{b}_m = -i(\Omega_m - \Omega)\bar{b}_m - \frac{\Gamma_m}{2}\bar{b}_m - i\int_0^L dz\ (g_0^m)^* e^{i\Delta q z} \bar{A}_{\mathrm{S}}^\dagger \bar{A}_{\mathrm{S}}, \tag{3.25}$$

$$\partial_t \bar{A}_{\mathrm{p}} + v_0\partial_z \bar{A}_{\mathrm{p}} = -i\sum_m g_0^m e^{i\Delta q z} \bar{A}_{\mathrm{p}} \bar{b}_m, \tag{3.26}$$

$$\partial_t \bar{A}_{\mathrm{S}} - v_0\partial_z \bar{A}_{\mathrm{S}} = -i\sum_m (g_0^m)^* e^{-i\Delta q z} \bar{b}_m^\dagger \bar{A}_{\mathrm{p}}. \tag{3.27}$$

We phenomenologically added a phonon dissipation rate $\Gamma_m/2$ to model all the phonon

losses. If we now make the stiff pump assumption ($\partial_z \bar{A}_\mathrm{p} = 0$) and small signal gain approximation ($\Delta P_\mathrm{S} \ll P_\mathrm{S}(L)$), the steady-state solutions to Eq. 3.25 for phonon mode can be given by

$$\bar{b}_m = (g_0^m)^* L \frac{\bar{A}_\mathrm{p}(0)\bar{A}_\mathrm{p}^*(L)}{\Omega - \Omega_m + i\Gamma_m/2} e^{-i\Delta qL/2} \mathrm{sinc}^2(\frac{\Delta qL}{2}). \tag{3.28}$$

and the Stokes signal power can be expressed as

$$\Delta P_\mathrm{S} = P_\mathrm{S}(0) - P_\mathrm{S}(L) \approx P_\mathrm{p}(0) \sum_m \frac{4|g_0^m|^2 L^2}{\hbar\omega_\mathrm{p} v_0^2 \Gamma_m} \frac{(\Gamma_m/2)^2}{(\Omega - \Omega_m)^2 + (\Gamma_m/2)^2} \mathrm{sinc}^2(\frac{\Delta qL}{2}). \tag{3.29}$$

At last, the single-photon coupling rate in our optomechanical system can be calculated based on the photon-phonon interaction Hamiltonian H^int, and is determined by the photo-elastic tensor and the mode overlap between the optical and acoustic fields. If we assume the pump and Stokes electric fields are both polarized in x direction, we can get a simplified expression as

$$g_0^m \approx i \frac{\omega^2 n^3 p_{13}}{2c} \sqrt{\frac{\hbar}{\Omega_m \rho A_\mathrm{ao} L}}. \tag{3.30}$$

Here it is also assumed that both the optical fields and the acoustic field are uniform inside the effective interaction area A_ao and $\omega_\mathrm{p} \simeq \omega_\mathrm{S} \equiv \omega$.

3.2 Theory of CABS spectroscopy

In this section, I will walk you through the theory behind the CABS spectroscopy. Since all the CABS measurements are performed at low temperature, it is similar to the high phonon coherence limit in the previous section. This is essentially a three-mode interaction problem, one phonon mode and two optical modes. Note that the phonon modes are discrete modes because they are bounded by the substrate surfaces,

while the two optical modes are continuous. Let's start with the field quantization.

3.2.1 Quantization of the acoustic field

Following [37], we introduce vector field variables $\mathbf{u}(\mathbf{r},t)$ describing the displacement and $\pi(\mathbf{r},t)$ as their conjugate momenta. Since $\mathbf{u}(\mathbf{r},t)$ and $\pi(\mathbf{r},t)$ form a canonical pair, they should satisfy the following commutation relations

$$[u^n(\mathbf{r}), \pi^m(\mathbf{r}')] = i\hbar\delta_{nm}\delta(\mathbf{r}-\mathbf{r}') \quad (m,n=1,2,3), \tag{3.31}$$

where δ_{nm} and $\delta(\mathbf{r}-\mathbf{r}')$ are the Kronecker delta and Dirac delta functions respectively. The acoustic Hamiltonian can be formulated as

$$H^A = \int \frac{\pi^i(\mathbf{r})\pi^i(\mathbf{r})}{2\rho(\mathbf{r})}\, d\mathbf{r} + \frac{1}{2}\int S^{ij}(\mathbf{r})c^{ijkl}(\mathbf{r})S^{kl}(\mathbf{r})\, d\mathbf{r}, \tag{3.32}$$

where $\rho(\mathbf{r})$ is the density, $c^{ijkl}(\mathbf{r})$ is the stiffness tensor, and

$$S^{ij}(\mathbf{r}) = \frac{1}{2}\left(\frac{\partial u^i(\mathbf{r})}{\partial r^j} + \frac{\partial u^j(\mathbf{r})}{\partial r^i}\right), \tag{3.33}$$

is the strain tensor. Based on this Hamiltonian, we can quickly write down the Heisenberg equations of motion,

$$\frac{\partial}{\partial t}u^n(\mathbf{r},t) = \frac{1}{i\hbar}\left[u^n(\mathbf{r}), H^A\right] = \frac{\pi^n(\mathbf{r},t)}{\rho(\mathbf{r})}, \tag{3.34}$$

$$\frac{\partial}{\partial t}\pi^n(\mathbf{r},t) = \frac{1}{i\hbar}\left[\pi^n(\mathbf{r}), H^A\right] = \frac{\partial}{\partial r^j}\left(c^{njkl}(\mathbf{r})S^{kl}(\mathbf{r})\right). \tag{3.35}$$

From these equations of motion, we can recover the Christoffel equation

$$\rho(\mathbf{r})\frac{\partial^2 u^n(\mathbf{r},t)}{\partial t^2} = \frac{\partial}{\partial r^j}\left(c^{njkl}(\mathbf{r})S^{kl}(\mathbf{r})\right). \tag{3.36}$$

Similar to the quantization of electromagnetic fields bounded in an FP cavity, we write down

$$\mathbf{u}(\mathbf{r}) = \sum_m \sqrt{\frac{\hbar\Omega_m}{2}}\, \mathbf{U}_m(\mathbf{r})\hat{b}_m + \text{h.c.}, \tag{3.37}$$

and claim that it will be the correct quantitation of the phonon field if the following normalization condition holds,

$$\int \rho(\mathbf{r})\, \Omega_m^2\, \mathbf{U}_m^*(\mathbf{r})\, \mathbf{U}_{m'}(\mathbf{r})\, d\mathbf{r} = \delta_{mm'}. \tag{3.38}$$

To confirm it, we substitute Eq. 3.37 back to the Hamiltonian equation 3.32 and hope to see the Hamiltonian of a harmonic oscillator. From Eq. 3.34 we get

$$\pi(\mathbf{r},t) = \rho(\mathbf{r})\frac{\partial \mathbf{u}(\mathbf{r},t)}{\partial t} = \sum_m \left(-i\Omega_m\rho(\mathbf{r})\right) \sqrt{\frac{\hbar\Omega_m}{2}}\, \mathbf{U}_m(\mathbf{r})\, \hat{b}_m + \text{h.c.}. \tag{3.39}$$

Then substitute it back to the Hamiltonian equation 3.32 and we obtain

$$\begin{aligned} H^A &= \int \frac{d\mathbf{r}}{\rho(\mathbf{r})} \left[\sum_m (-i\Omega_m\rho(\mathbf{r}))\sqrt{\frac{\hbar\Omega_m}{2}}\mathbf{U}_m(\mathbf{r})\hat{b}_m + \text{h.c.}\right]^2 \\ &= \sum_{m,m'} \frac{\hbar}{2}\sqrt{\Omega_m\Omega_{m'}} \int \rho(\mathbf{r})\Omega_m\Omega_{m'}\mathbf{U}_m^*(\mathbf{r})\mathbf{U}_{m'}(\mathbf{r})d\mathbf{r}\cdot \hat{b}_m^\dagger\hat{b}_{m'} + \text{h.c.} \\ &= \frac{1}{2}\sum_m \hbar\Omega_m \left(\hat{b}_m^\dagger\hat{b}_m + \hat{b}_m\hat{b}_m^\dagger\right), \end{aligned} \tag{3.40}$$

One can also easily confirm that the following commutation relation between $\hat{b}_m$ and $\hat{b}_m^\dagger$ holds,

$$\left[\hat{b}_m, \hat{b}_{m'}^\dagger\right] = \delta_{m,m'}. \tag{3.41}$$

For simplicity, consider a longitudinal acoustic wave propagating within the μH-BAR of length L that has an effective area of A_a. It gets reflected at the boundary and forms a standing wave. Then the scalar field of the standing wave can be expressed

by

$$U_m(\mathbf{r}) = U_m \cdot \cos(q_m z), \tag{3.42}$$

where $q_m = \Omega_m/v = 2\pi m/\lambda_{\text{ph}}$ is the k-vector of the m-th phonon mode. The normalization equation 3.38 requires

$$\begin{aligned} \rho\Omega_m^2 \int_V |U_m(\mathbf{r})|^2 d\mathbf{r} &= \rho\Omega_m^2 \int_{A_a} |U_m|^2 dxdy \cdot \int_0^L \cos^2(q_m z) dz \\ &= \frac{\rho\Omega_m^2 L}{2} |U_m|^2 A_a \\ &= 1, \end{aligned} \tag{3.43}$$

which gives

$$U_m(\mathbf{r}) = \sqrt{\frac{2}{\rho\Omega_m^2 A_a L}} \cdot \cos(q_m z). \tag{3.44}$$

3.2.2 Quantization of the optical field

The quantization of the optical field is similar to that of the acoustic field. The tricky part is that although they form standing waves due to the mirror reflection, they are continuous modes. As you will see in this section, it makes the normalization condition a bit different. The optical Hamiltonian can be written as

$$H^{\text{EM}} = \frac{1}{2\mu_0} \int B^i(\mathbf{r}) B^i(\mathbf{r})\, d\mathbf{r} + \frac{1}{2\epsilon_0} \int D^i(\mathbf{r}) \beta_{\text{ref}}(\mathbf{r}) D^i(\mathbf{r})\, d\mathbf{r}, \tag{3.45}$$

where $\mathbf{B}(\mathbf{r})$ is the magnetic field, $\mathbf{D}(\mathbf{r})$ is the electric displacement, and $\beta_{\text{ref}}(\mathbf{r}) = 1/\epsilon_{\text{ref}}(\mathbf{r})$ is the inverse of the background permittivity, neglecting any acoustic effects.

Now since the optical field is continuous, we expand the electric displacement as

$$\mathbf{D}(\mathbf{r}, t) = \int dk \sqrt{\frac{\hbar\omega_k}{2}}\, \mathbf{U}_k(\mathbf{r})\, \hat{a}_k(t) + \text{h.c.}, \tag{3.46}$$

with the normalization condition

$$\frac{1}{\epsilon_0}\int d\mathbf{r}\,\beta_{\mathrm{ref}}(\mathbf{r})\,\mathbf{U}_k^*(\mathbf{r})\,\mathbf{U}_{k'}(\mathbf{r}) = \delta(k-k'). \tag{3.47}$$

Substituting Eq. 3.46 back to Eq. 3.45, we can verify that it is the correct quantization form of the electromagnetic field.

$$\begin{aligned} H^{\mathrm{EM}} &= \frac{1}{\epsilon_0}\int D^i(\mathbf{r})\beta_{\mathrm{ref}}(\mathbf{r})D^i(\mathbf{r})\,d\mathbf{r} \\ &= \frac{1}{\epsilon_0}\int d\mathbf{r}\beta_{\mathrm{ref}}(\mathbf{r})\left[\int dk\sqrt{\frac{\hbar\omega_k}{2}}\mathbf{U}_k(\mathbf{r})\hat{a}_k(t) + \mathrm{h.c.}\right]^2 \\ &= \iint dk\,dk'\,\frac{\hbar}{2}\sqrt{\omega_k\omega_{k'}}\cdot\frac{1}{\epsilon_0}\int d\mathbf{r}\,\beta(\mathbf{r})\mathbf{U}_k^*(\mathbf{r})\mathbf{U}_{k'}(\mathbf{r})\cdot\hat{a}_k^\dagger\hat{a}_{k'} + \mathrm{h.c.}, \\ &= \frac{1}{2}\int \hbar\omega_k\left(\hat{a}_k^\dagger\hat{a}_k + \hat{a}_k\hat{a}_k^\dagger\right). \end{aligned} \tag{3.48}$$

For simplicity, we consider a linearly polarized optical field propagating in a medium that has uniform permittivity. Write down the optical field as

$$U_k(\mathbf{r}) = U_k\cdot\sin(kz) \quad (k>0). \tag{3.49}$$

Then the normalization condition Eq. 3.47 requires

$$\begin{aligned} \frac{1}{\epsilon_0}\int d\mathbf{r}\,\beta(\mathbf{r})\,U_k^*(\mathbf{r})\,U_{k'}(\mathbf{r}) &= \frac{\beta_{\mathrm{ref}}}{\epsilon_0}\int_{A_o} U_k^*U_{k'}dxdy\cdot\int_0^\infty \sin(kz)\sin(k'z)\,dz \\ &= \frac{1}{\epsilon_0\epsilon_{\mathrm{ref}}}|U_k|^2A_o\cdot\frac{\pi}{2}\delta(k-k') \\ &= \delta(k-k'). \end{aligned} \tag{3.50}$$

It gives

$$U_k(\mathbf{r}) = \sqrt{\frac{2\epsilon_0\epsilon_{\mathrm{ref}}}{\pi A_o}}\cdot\sin(kz), \tag{3.51}$$

where A_o is the effective area of the optical modes.

3.2.3 The zero-point coupling rate

Now that we have quantized the optical field and acoustic field, neglecting the moving boundary effect (this is usually infinitesimal in bulk devices like our μHBARs), let's write down the optomechanical interaction Hamiltonian only addressing the photoelastic effect,

$$\begin{aligned} H^{\text{int}} &= \frac{1}{2\epsilon_0}\int D^i(\mathbf{r})D^j(\mathbf{r})p^{ijlm}S^{lm}(\mathbf{r}) \\ &= \frac{1}{2\epsilon_0}\int D^i(\mathbf{r})D^j(\mathbf{r})p^{ijlm}\frac{\partial u^l(\mathbf{r})}{\partial r^m}, \end{aligned} \tag{3.52}$$

where p^{ijkl} is the photoelastic tensor. The photoelastic tensor for α-quartz under retracted subscripts is

$$\begin{aligned} p &= \begin{bmatrix} p_{11} & p_{12} & p_{13} & p_{14} & 0 & 0 \\ p_{12} & p_{11} & p_{13} & -p_{14} & 0 & 0 \\ p_{31} & p_{31} & p_{33} & 0 & 0 & 0 \\ p_{41} & -p_{41} & 0 & p_{44} & 0 & 0 \\ 0 & 0 & 0 & 0 & p_{44} & p_{41} \\ 0 & 0 & 0 & 0 & p_{14} & (p_{11}-p_{12})/2 \end{bmatrix} \\ &= \begin{bmatrix} 0.16 & 0.27 & 0.27 & -0.03 & 0 & 0 \\ 0.27 & 0.16 & 0.27 & 0.03 & 0 & 0 \\ 0.29 & 0.29 & 0.10 & 0 & 0 & 0 \\ -0.047 & 0.047 & 0 & -0.079 & 0 & 0 \\ 0 & 0 & 0 & 0 & -0.079 & -0.047 \\ 0 & 0 & 0 & 0 & -0.03 & -0.055 \end{bmatrix}. \end{aligned} \tag{3.53}$$

Since the acoustic wave in our μHBAR propagates along z-axis, r^m in Eq. 3.52 is z axis, i.e. $m = 3$. If $l = 1$ or $l = 2$, the relevant photoelastic constant will be either in the 5-th or 4-th column, respectively. You can see from Eq. 3.53 that all the numbers in the 4-th and 5-th columns of the quartz photoelastic tensor are pretty small. Only when $l = 3$, the relevant photoelastic constant will be in 3-rd column. We can align the two optical polarizations to be either xx or yy, which corresponds to photoelastic constant p^{1133} or p^{2233}, respectively. Both give a value of 0.27, a pretty large value in the whole photoelastic tensor. This is why the phonons we manipulate are mostly longitudinal phonons. Moreover, realize that the x-polarized light and y-polarized light have the same coupling strength to the longitudinal phonons. It means that we can drive the phonons using one polarization and detect them using the other polarization. This is exactly what we do in the dual-polarization pump-probe CABS spectroscopy, which will be discussed in next section.

Back to the interaction Hamiltonian, consider two laser beams, one pump beam (k_p, ω_p) and one Stokes beam (k_S, ω_S), are interacting with the acoustic wave (q_m, Ω_m). Assume both pump and Stokes beams are x-polarized and the acoustic wave is a longitudinal wave propagating along z-direction. Substituting Eq. 3.44 and Eq. 3.51

into Eq. 3.52, we get

$$
\begin{aligned}
H^{\text{int}} &= \frac{1}{2\epsilon_0}\int_V D^2(\mathbf{r}) p^{13} \partial_z u(\mathbf{r}) \\
&= \frac{p^{13}}{2\epsilon_0}\int_V d\mathbf{r}\left[\int dk_p \sqrt{\frac{\hbar\omega_{k_p}}{2}} U_{k_p}\sin(k_p z)\hat{a}_{k_p} + \int dk_S \sqrt{\frac{\hbar\omega_{k_S}}{2}} U_{k_S}\sin(k_S z)\hat{a}_{k_S} + \text{h.c.}\right]^2 \\
&\qquad \cdot \left[\sum_m \sqrt{\frac{\hbar\Omega_m}{2}} U_m(-q_m)\sin(q_m(z-d))\hat{b}_m + \text{h.c.}\right] \\
&= \frac{p^{13}}{2\epsilon_0}\sum_m \sqrt{\frac{\hbar^3\omega_{k_p}\omega_{k_S}\Omega_m}{8}} \iint dk_p dk_S U_{k_p} U_{k_S}(-q_m) U_m A_{ao} \cdot \\
&\qquad \int_d^{d+L} dz \sin(k_p z)\sin(k_S z)\sin(q_m(z-d)) \cdot 2(\hat{a}^\dagger_{k_p}\hat{a}_{k_S}\hat{b}_m + \text{h.c.}) \\
&= -\sum_m \iint dk_p dk_S \int_d^{d+L} \sin(\Delta q z + q_m d) dz \cdot (\hat{a}^\dagger_{k_p}\hat{a}_{k_S}\hat{b}_m + \text{h.c.}) \cdot \\
&\qquad \frac{q_m p^{13}}{4\epsilon_0}\sqrt{\frac{\hbar^3\omega_{k_p}\omega_{k_S}\Omega_m}{8}} U_{k_p} U_{k_S} U_m A_{ao}.
\end{aligned}
\tag{3.54}
$$

Here the optical mirror surface is defined as $z = 0$ and d is the spacing between the mirror surface and the substrate surface. The substrate has thickness L, thus the interaction Hamiltonian integrates from d to $d + L$. $\Delta q = k_p + k_S - q_m$ is the phase mismatch. Here I assume the effective areas of the laser beams and acoustic wave are the same, i.e. $A_a = A_o = A_{ao}$. I also used the identity

$$
\sin(a)\sin(b)\sin(c) = \frac{1}{4}\left(\sin(c+a-b) + \sin(c-a+b) - \sin(c+a+b) - \sin(c-a-b)\right),
\tag{3.55}
$$

in the derivation. Comparing this with

$$
H^{\text{int}} = -\sum_m \iint \frac{dk_p dk_S}{2\pi}\hbar g(k_p, k_S, g_m) \cdot (\hat{a}^\dagger_{k_p}\hat{a}_{k_S}\hat{b}_m + \text{h.c.}),
\tag{3.56}
$$

we get the zero-point coupling rate of the three-wave interaction

$$\begin{aligned} g(k_p, k_S, g_m) &= \frac{\pi p^{13} q_m}{4\epsilon_0} \sqrt{\frac{\hbar}{2} \omega_{k_p} \omega_{k_S} \Omega_m} \cdot U_{k_p} U_{k_S} U_m A_{ao} \\ &\qquad \cdot \int_d^{d+L} \sin(\Delta q z + q_m d) dz \\ &= \frac{\epsilon_{\text{ref}}\ p^{13} q_m}{2} \sqrt{\frac{\hbar \omega_{k_p} \omega_{k_S}}{\rho \Omega_m A_{ao} L}} \cdot \int_d^{d+L} \sin(\Delta q z + q_m d) dz \\ &= \frac{p^{13} n^3 \omega^2}{c} \sqrt{\frac{\hbar}{\rho \Omega_m A_{ao} L}} \cdot \int_d^{d+L} \sin(\Delta q z + q_m d) dz \\ &= g_0 \cdot \int_d^{d+L} \sin(\Delta q z + q_m d) dz. \end{aligned} \tag{3.57}$$

Note that $g(k_p, k_S, g_m)$ has unit of [Hz·m], and g_0 has unit of [Hz], because

$$\begin{aligned} \int_d^{d+L} \sin(\Delta q z + q_m d) dz &= \int_0^L \sin(\Delta q z + \phi) dz \\ &= \frac{1}{\Delta q} \left[\cos\phi - \cos(\Delta q L + \phi)\right] \\ &= \frac{2}{\Delta q} \sin(\Delta q L/2) \sin(\phi + \Delta q L/2) \\ &= L \cdot \frac{\sin(\Delta q L/2) \sin(\phi + \Delta q L/2)}{\Delta q L/2}. \end{aligned} \tag{3.58}$$

Here $\phi = (k_p + k_S)d \approx q_m d = 2\pi d/\lambda_{\text{ph}}$ is the phase delay introduced by the spacing between the mirror and substrate and it can largely modulate the phase matching profile. When $\phi = 0$,

$$g(k_p, k_S, g_m) = g_0 L \cdot \sin(\Delta q L/2) \text{sinc}(\Delta q L/2). \tag{3.59}$$

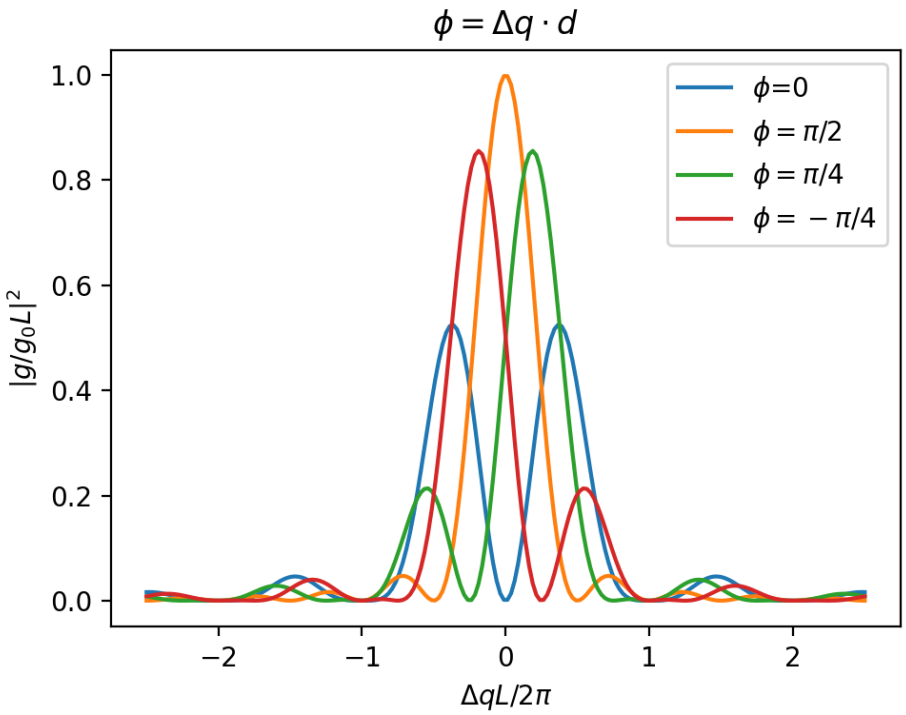

Figure 3.5: Phase matching profile. L is the substrate thickness and $\Delta q = k_p + k_S - q_m$ is the k mismatch. It is largely modulated by the phase delay ϕ caused by the spacing between the optical mirror and substrate.

When $\phi = \pi/2$,

$$g(k_p, k_S, g_m) = g_0 L \cdot \mathrm{sinc}(\Delta q L). \tag{3.60}$$

Fig. 3.5 shows the phase matching profiles under different phase delays. It's very sensitive to the phase delay, thus to the spacing d given how small the phonon wavelength is. I'd like to remind you that one FSR means that single-trip phase shifts by $\Delta qL = \pi$, therefore in Fig. 3.5 it will be $\Delta qL = \pi/2\pi = 1/2$. Therefore, you can see at most 2 or 3 longitudinal mode families in the main lobe of the phase matching profile in the spectral measurement.

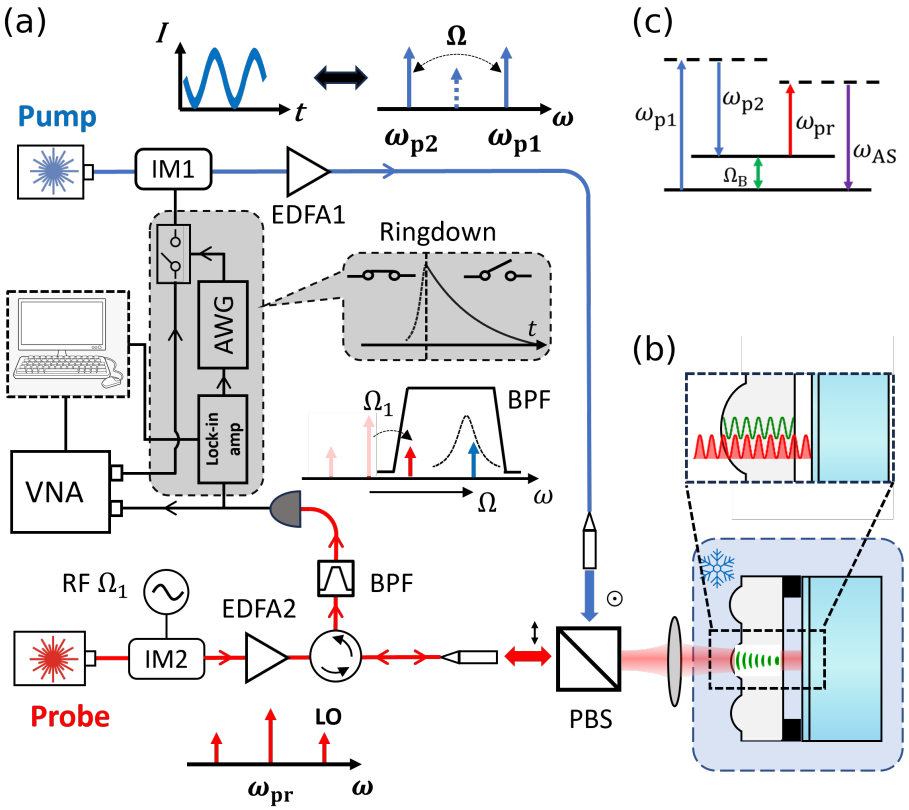

Figure 3.6: (a) Schematic of CABS setup. The pump laser (blue) is centered at 1549.068 nm, s-polarized, passing through by an intensity modulator (IM1) driven by a vector network analyzer (VNA) at ∼6.33 GHz, at null-bias configuration. The probe laser (red) is centered at 1549.120 nm, p-polarized. A local oscillator (LO) signal is imprinted on the probe light by another intensity modulator IM2, driven at 12.651 GHz. Both pump and probe lights then combine at a polarization beamsplitter (PBS) and shine into our μHBAR device and enable both Stokes and anti-Stokes scattering of the probe light through acousto-optic interaction. Then the anti-Stokes light (p-polarized, same as the probe light), together with the LO, is transmitted through a band-pass filter (BPF) and detected by a photodetector. The beat note output from the photodetector, usually at ∼10 MHz, is then split in half; one goes to the receiving port of the VNA for spectral measurements, while the other one goes to an arbitrary waveform generator (AWG) for ringdown measurements. The μHBAR device is mounted on an optical mirror with a spacer in between and cooled down to 6 K. (b) The laser intensity pattern (red) needs to match with the phonon displacement pattern (green) to satisfy the phase matching condition. (c) Energy diagram of the pump-probe CABS process.

3.3 CABS spectroscopy and phonon ring-down

We developed a two-color pump-probe spectroscopy technique to measure phonon coherence. Fig. 3.6 shows the reflection-mode apparatus used to perform non-invasive Brillouin-based measurements of the fabricated µHBARs. Pump (blue) and probe (red) waves having distinct wavelengths are used to simultaneously transduce and detect phonons within the µHBAR, enabling background-free measurement of the transduced elastic wave motion.

The µHBAR array is mounted on a dielectric mirror such that both the pump and probe waves produce standing-wave field patterns, closely matching those of the standing-wave phonon modes within the µHBAR (Fig. 3.6b). This permits efficient Brillouin (or acousto-optic) coupling to the µHBAR phonon modes while eliminating the need for active interferometric stabilization required using prior methods [28, 38]. The pump and probe waves are focused to a spot size closely matching that of the µHBAR, which allows coupling to the fundamental Gaussian µHBAR phonon modes with frequencies near the Brillouin frequency of z-cut quartz ($\Omega_B/2\pi \cong 12.66$ GHz) using 1550 nm light. The frequencies of the pump and probe waves are chosen to fall within the Brillouin phase-matching bandwidth, enabling efficient transduction and detection of elastic wave motion using the coherent anti-Stokes Brillouin scattering (CABS) process, diagrammed in Fig. 3.6c. Phonons are first generated within the µHBAR using an intensity-modulated pump wave (blue). As seen in Fig. 3.6a (upper arm), intensity modulation produces two optical tones with a frequency separation (Ω) near the Brillouin frequency (Ω_B). A stimulated Stokes scattering process results in the energy transfer between these optical pump tones, exciting phonons within the µHBAR; the resulting elastic wave motion is simultaneously detected using a continuous-wave probe laser (red). Stokes and anti-Stokes sidebands are imprinted on the probe wave through phase-matched Brillouin scattering (lower arm of Fig. 3.6a). Heterodyne detection of the anti-Stokes sideband is then used to measure the

phase and amplitude of coherently driven phonons.

To prevent optical crosstalk, orthogonally polarized pump (s-polarized) and probe (p-polarized) waves are used to excite and detect phonons within the µHBAR resonator. The pump wave (s-polarized) is synthesized by modulating 1549.068 nm laser light using an intensity modulator (IM1) that is driven by a vector network analyzer (VNA). This modulator (IM1) is operated at the null-bias point to produce two first-order sideband tones with frequency separation Ω, when intensity modulator is driven at frequency $\Omega/2$. This permits excitation of the µHBAR phonon modes when the frequency separation (Ω) is tuned through the Brillouin frequency (Ω_{B}). This pump wave is then amplified with an EDFA to boost its optical intensity before entering the PBS to excite phonons within the µHBAR. A 1549.120 nm probe wave (p-polarized) is amplified using a second EDFA before passing through the PBS to interact with the µHBAR. The phase and amplitude of the excited phonons are measured through heterodyne detection of an anti-Stokes sideband that is imprinted on the probe wave through Brillouin scattering.

Coherent measurement of the elastic wave motion is performed by detecting the heterodyne beat-note produced by the interference of the anti-Stokes sideband with an optical local oscillator (LO). The optical LO tone is imprinted on the probe wave using a separate intensity modulator (IM2), driven at frequency Ω_1. While intensity modulation produces both $+\Omega_1$ and $-\Omega_1$ sidebands, only the $+\Omega_1$ is used as the optical LO. The reflected probe is then bandpass-filtered such that only anti-Stokes sideband and the $+\Omega_1$ LO tone are transmitted, enabling coherent detection of the elastic-wave motion at frequency $\Omega - \Omega_1$ using a high-speed photodetector. Since the detected RF signal power is proportional to the anti-Stokes optical power, the RF power is also proportional to the phonon population inside the µHBAR device. During frequency domain spectral measurements, a VNA is used to sweep the drive frequency (Ω) through the µHBAR resonance while simultaneously measuring the

phase and amplitude of the anti-Stokes beat note at frequency $\Omega - \Omega_1$. A slow sweep is necessary to ensure steady-state measurement of the resonant response. The dwell time between two adjacent frequency points needs to be longer than the lifetime of the phonon modes to avoid oscillatory patterns in the spectrum caused by unwanted phonon interference.

During ringdown measurements, high-speed demodulation of this same heterodyne beat note (at frequency $\Omega - \Omega_1$) is performed using a lock-in amplifier while the VNA sweeps the drive frequency (Ω) very rapidly through the cavity resonance. During ring-down measurements, the intensity modulation of the pump wave is abruptly switched off when the drive frequency (Ω) reaches the resonant frequency of the target phonon mode; the lock-in amplifier then records the phase and amplitude of the anti-Stokes beat-note during free-induction decay. The abrupt increase in amplitude of the $\Omega - \Omega_1$ beat note during resonant excitation of the µHBAR is used to trigger an arbitrary waveform generator (AWG); the AWG causes the RF switch to open, abruptly turning off the RF drive to IM1, permitting lock-in measurement of free-induction decay of the µHBAR phonon mode.

3.4 Windshield and sample preparation

All phonon measurements were performed at liquid helium temperature ($\sim$ 4K). The sample device is installed inside a Janis ST-100 cryostat and cooled by a recirculation gas cooler (RGC4) or a helium dewar (for better temperature stability). We machined an oxygen-free high-conductivity (OFHC) copper to match the size of the µHBAR samples, which is directly connected to the cold finger of the cryostat. The sample is sitting directly on the copper mount and sandwiched by an optical mirror from the other side. Then the optical mirror is clamped from the other side by a copper plate via spring-loaded screws. A spacer is placed between the sample and the mirror

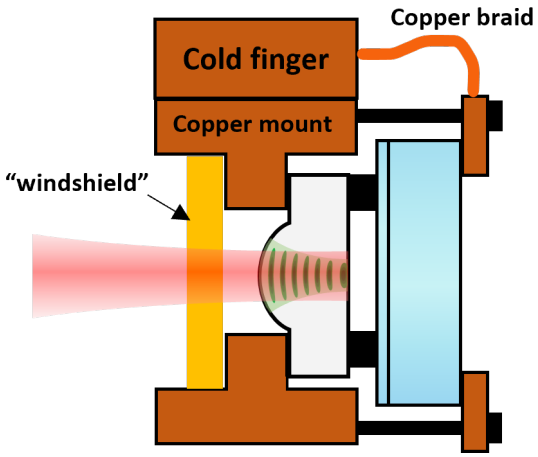

Figure 3.7: Sketch of the sample mount and the "windshield".

to avoid leakage of phonons into the mirror. The copper clamp is connected to the cold finger with a copper braid for optimal cooling. To obtain consistent and repeatable measurements of the μ HBAR linewidth, it was necessary to design the sample environment to minimize the adsorption of residual gas molecules on the µHBAR surface. Prior to cooling down, the cryostat is pumped at least below 1e-5 hPa. Since air molecules have a near-unity adsorption probability when they make contact with cold material surfaces (i.e. temperatures below 100 K) and have a very low probability of desorption, this is sometimes referred to as the "hit-and-stick" regime of adsorption dynamics. Hence, adsorption of molecules to the µHBAR surface can be prevented by surrounding the crystal surfaces by cold objects and ensuring that there is no ballistic trajectory that allows molecules in the cryostat chamber to attach the µHBAR surface. To prevent residual gas in the cryostat from condensing onto the sample, the plano and convex surfaces of µHBAR are protected using the sample holder in Fig. 3.7. Attachment of the µHBAR to the mirror offers protection to the plano surface. However, it was also important to introduce a cold "windshield" to prevent the convex µHBAR surface from being directly exposed to cryostat chamber (Fig. 3.7). Through these experiments, an AR-coated glass window is used as the windshield, however any transparent substrate can be used. Without the windshield,

we observed rapid degradation in the µHBAR Q-factors and a time-dependent red-shift of the phonon modes. However, after introducing the cold windshield, these problems were eliminated, permitting stable and repeatable measurements of phonon Q-factors without any drift of phonon frequency.

Since the phonon modes are very sensitive to surface adsorbates, our µHBAR devices need to be carefully cleaned before put in the cryostat. We follow a standard cleaning protocol before each cryogenic measurement:

1. sonication with organic solvent NMP, acetone, methanol, 3 min each;
2. Piranha cleaning for 8 min, and rinse it for 10 min with DI water;
3. (optional) oxygen plasma ashing for 1 min at a RF power of 100 W and a pressure of 300 mTorr.

After the cleaning procedures, the sample needs to be transferred to the cryostat and vacuumed as soon as possible. We did observe degradation of device Q-factors due to longer time of exposure to the air environment after the cleaning. Using a vacuum transfer box can be a good practice.

Chapter 4

Experiment results and phonon coherence analysis

In this chapter, we use CABS spectroscopy to study phonon coherence in μHBAR devices. The phonon coherence is determined by the phonon dissipation (loss) rate and pure dephasing rate. The phonon coherence is reflected by the spectral linewidth and the phonon dissipation rate can be measured directly by the phonon ring-down. As you can see in this chapter, for all the μHBAR devices we measured, the coherence Q-factor matches very well with the ring-down Q-factor, suggesting that the pure dephasing rate is negligible and the phonon coherence is mostly limited by phonon dissipation. Temperature-varying measurements indicate that at low temperatures ($T \sim 6$ K), the bulk phonon-phonon scattering becomes insignificant. Therefore, to figure out the dominating phonon dissipation mechanism, we fabricated a series of μHBAR devices of thicknesses ranging from $0.5 \sim 3.0$ mm, which effectively varies the surface participation ratio. We observed that the Q-factors show a linear dependence on the thickness, suggesting that the surface has a major contribution to the total phonon dissipation rate. Detailed analysis can be found in Section 4.4.

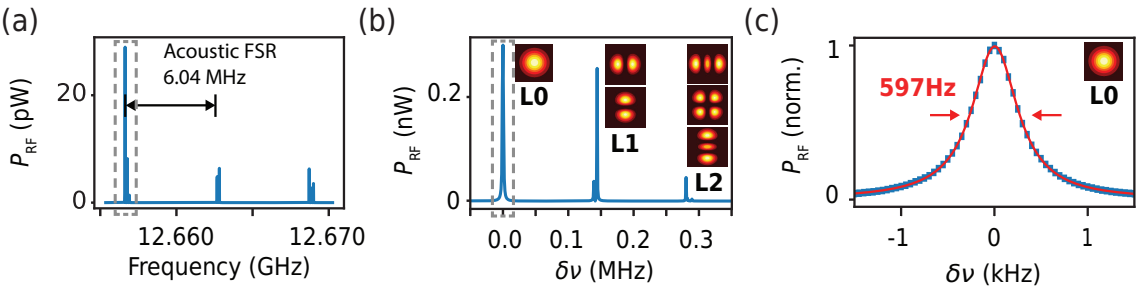

Figure 4.1: Phonon spectrum of a 0.5-mm-thick µHBAR device. (a) Spectrum of three longitudinal modes with acoustic free spectral range (FSR) of 6.04 MHz. (b) Each longitudinal mode family includes many transverse Hermite-Gaussian (HG) modes. (c) Spectrum of the fundamental Gaussian mode. 597 Hz linewidth corresponds to a Q-factor of 22 million.

4.1 Phonon spectrum and ringdown

Figures 4.1a-c show the phonon spectra from a µHBAR with $L = 0.5$ mm taken at 12.66 GHz frequencies at $T = 10$ K. The broad spectral scan of Fig. 4.1a shows three sets of resonances that repeat every 6.04 MHz, corresponding to the FSR of longitudinal acoustic modes. A magnified view of the first set of resonances is seen in Fig. 4.1b, which corresponds to the fundamental Gaussian mode and higher-order Hermite-Gaussian (HG) modes, are labeled as L0, L1, and L2. The frequency splitting between these modes is determined by the device thickness and radius of curvature of the convex surface. Here it's measured to be XXX, which matches well with thickness of 0.5 mm and radius of curvature of 100 mm, as seen in Table 2.2. According to the Gaussiam mode theory, in an ideal Fabry-perot cavity where the concave mirror is strictly spherical, the L1={HG01, HG10} mode family and the L2={HG02, HG11, HG20} are both degenerate. The frequency splittings we observed here among L1 and L2 are attributed to slight irregularities in the shape of the convex surface, which results from the imperfectly reflowed resist during the fabrication process. A high-resolution scan of the L0 resonance, seen in Fig. 4.1c, reveals a phonon linewidth of $\Delta\Omega/2\pi = 597$ Hz, corresponding to a Q-factor of 22 million.

With this powerful spectroscopic tool, we can quickly scan over multiple µHBARs

on the same substrate. Fig. 4.2a shows the measured Q-factors (in million) of all nine μHBAR devices on one 2.5-mm-thick substrate. All the devices show Q-factors higher than 100 million. Individual device reaches a Q-factor of 133 million. This is significantly higher than the Q-factor of a 0.5-mm-thick μHBAR device, which already gives a hint about the dominating phonon loss mechanism. But we will discuss it later in Section 4.4. Fig. 4.2b and c shows the phonon spectrum and ring-down of a 2.5-mm-thick μHBAR at 12.66 GHz frequency. The spectral linewidth is measured to be $\Delta\nu = 100$ Hz, corresponding to a spectral Q-factor of 126 million as $Q = \Omega/2\pi\nu$. The ring-down result shows a lifetime of 1.55 ms, corresponding to a ring-down Q-factor of 124 million as $Q = \Omega\tau_o$. The fact that the spectral Q matches well with the ring-down Q reveals that our μHBAR has a negligible pure dephasing rate (see Section 4.4 for more details). The inset of Fig. 4.2c plots the ring-down signal in a quadrature coordinate. As phonon experiences a free induction decay, its amplitude (normalized) goes down from 1 to 0, but along a constant-phase path (a straight line). It suggests that the phase of the phonon field is well kept as it goes through the free-induction decay, meaning there is negligible dephasing. This is a remarkable feature of our μHBAR devices compared with the nano-beam phononic resonators, as they are well-known to have a strong dephasing mechanism due to large interaction with surface two-level systems [19].

Now that we have identified that there is no dephasing in the μHBAR device, the phonon decoherence only results from energy dissipation, i.e. phonon loss. The next question to ask is what is the dominating phonon loss mechanism in our μHBAR system.

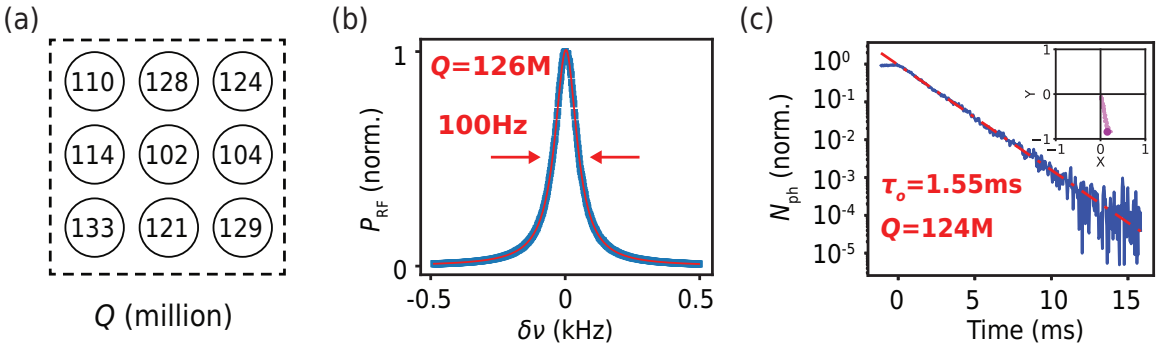

Figure 4.2: (a) Measured Q-factors of all 9 µHBAR devices on a 2.5-mm-thickness substrate. (b) Phonon spectrum of a 2.5-mm-thick µHBAR device, showing a linewidth $\Delta\nu = \Delta\Omega/2\pi = 100$ Hz and a spectral Q-factor of 126 million. (c) Phonon ring-down of the same µHBAR device as in (b). Exponential fitting yields a lifetime of 1.55 ms, corresponding to a Q-factor of 124 million. Inset top right: Coherent phonon ring-down plotted in a quadrature plane.

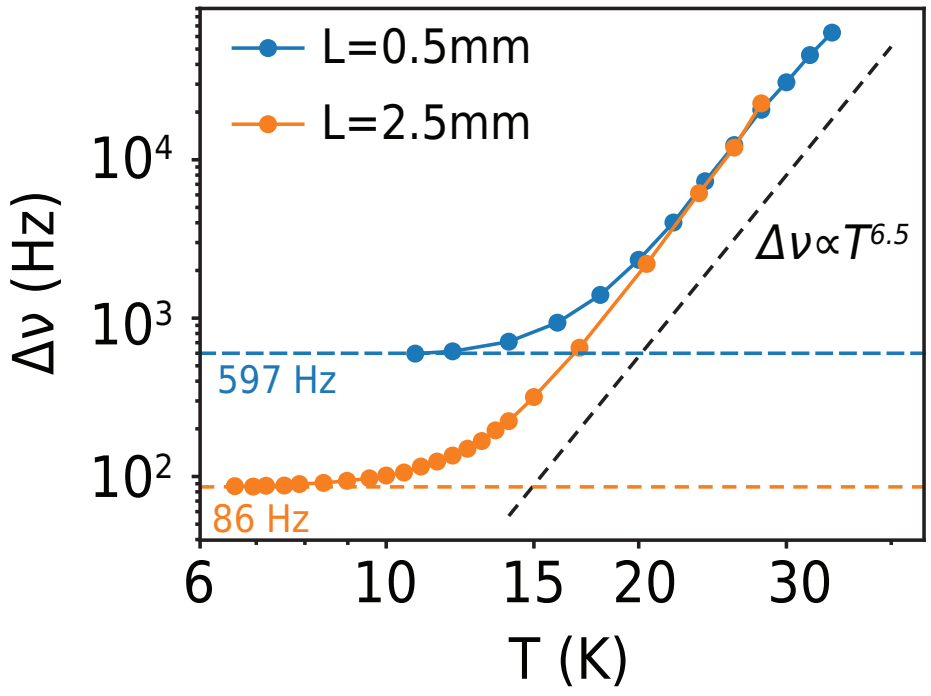

Figure 4.3: Phonon Q-factors at different temperatures. When $T > 18$ K, the phonon linewidth shows clearly $T^{6.5}$ temperature dependence (grey dashed line) due to bulk phonon-phonon scattering; when $T < 10$ K, the 0.5 mm µHBAR plateaus at 597 Hz, and the 2.5 mm µHBAR plateaus at 86 Hz.

4.2 Temperature sweep

To figure out the dominating phonon loss mechanism, we measured the phonon spectral linewidths ($\Delta\nu$) of μHBARs at different temperatures. Fig. 4.3 shows the results of a 0.5-mm-thick μHBAR device (blue) and a 2.5-mm-thick device (orange). When $T > 18$ K, the phonon linewidths of both μHBARs clearly show $T^{6.5}$ temperature dependence (tilted blank dashed line). This is predicted by the Landau-Rumer theory that features phonon-phonon scattering in the bulk material (see Section 4.4 for more details). However, at lower temperature ($T < 10$ K), the 0.5-mm-thick μHBAR linewidth plateaus at 597 Hz (blue dashed line), and the 2.5-mm-thick μHBAR linewidth plateaus at 86 Hz (orange dashed line).

From the above result, we learned that at low temperatures ($T < 10$ K), the bulk phonon-phonon scattering loss can be ruled out. Instead, whatever dominates the phonon loss here is independent on temperature. However, there are still a number of dissipation mechanisms that are not temperature dependent, including impurity scattering, surface roughness scattering, subsurface dislocation scattering, etc. In the next section, we try to identify whether the loss comes from the bulk or the surface.

4.3 Varying surface participation

Whether the dominating phonon loss comes from the bulk or surface can be investigated by varying the device thickness, which effectively changes the surface participation. From the analysis in Secion 4.4, we know that if the surface loss dominates, the total Q-factor scales linearly with the device thickness; if the bulk loss dominates, the total Q-factor is independent on the device thickness. Following this idea, we fabricated and measured multiple μHBAR devices with a range of thicknesses (0.5 mm to 3.0 mm). Fig. 4.4 shows the statistics of the measured Q-factors of 6 substrates with thickness ranging from 0.5 to 3.0 mm, each including 9 μHBAR devices. As is shown

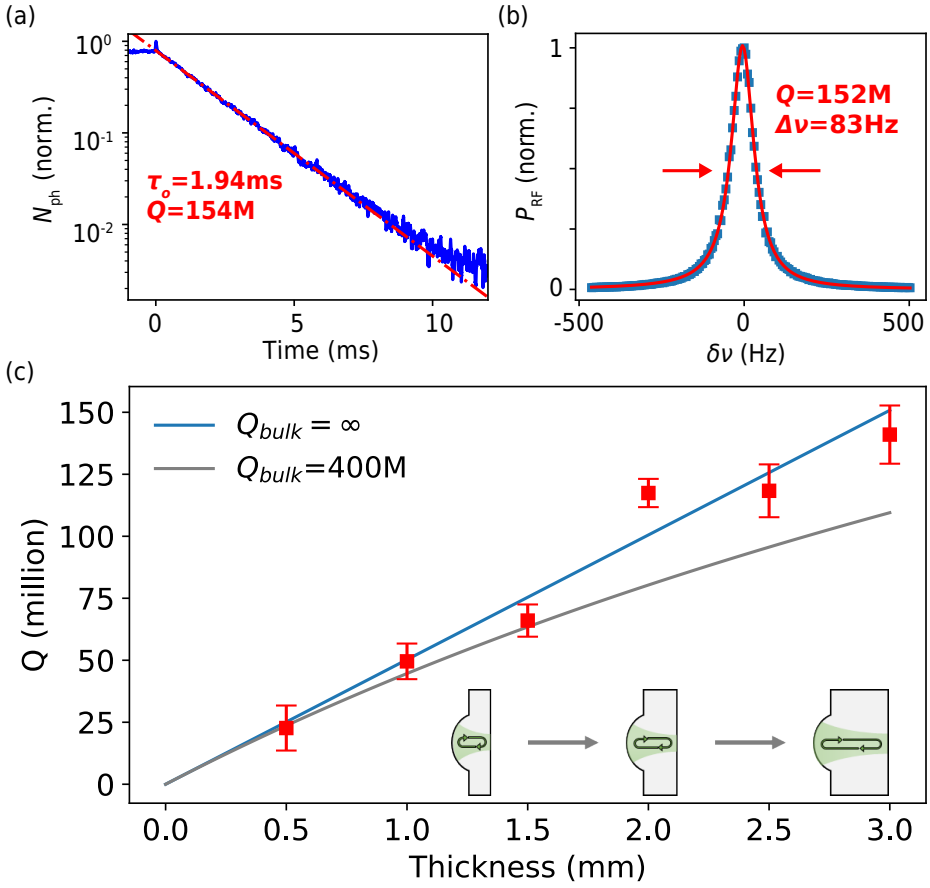

Figure 4.4: Statistics of measured Q-factors of 6 µHBAR substrates with thickness ranging from 0.5 to 3.0 mm. (a) Phonon ring-down result of the highest-Q µHBAR device. (b) Phonon spectrum of the highest-Q µHBAR device. (c) Summary of the mean values and standard deviations of the Q-factors for each thickness.The blue trend line assumes a 250 ppm surface loss per reflection and no bulk loss ($Q_{\mathrm{bulk}} = \infty$). The grey trend line assumes a 250 ppm surface loss per reflection, plus bulk loss ($Q_{\mathrm{bulk}} = 400$ million).

in Fig. 4.4c, the mean values of Q-factors align very well on a straight line (blue) which corresponds to 250 ppm surface loss per reflection and no bulk loss. This is a direct evidence that our µHBARs are limited by the phonon loss from the surface, rather than the bulk. If we artificially add some bulk loss ($Q_{\text{bulk}} = 400$ million) into the model, you will get the grey line. The individual highest-Q µHBAR device we measured is, without much surprise, on a 3-mm-thick substrate. Fig. 4.4a and b show you the ring-down result and phonon spectrum of it. The lifetime extracted from the ring-down result is 1.94 ms, corresponding to a ring-down Q of 154 million, and the spectral linewidth is measured to be 83 Hz, corresponding to a spectral Q of 152 million. Again, the fact that the ring-down Q matches so well with the spectral Q indicates that there is negligible dephasing rate in our µHBAR system.

4.4 Phonon coherence analysis

This section provides the theoretical background for analyzing the experimental results for this chapter. I start by giving definitions to the lifetime and coherence time of a Fabry-Perot cavity, explaining their relation and difference. You will see that their definitions are very similar to those of T_1 and T_2, which are widely used in the superconducting qubit community to describe a two-level system. Then I will introduce the phonon loss model we used to distinguish different loss sources.

4.4.1 Lifetime and coherence time

Consider a FP cavity of length L along z-direction where a field (optical or acoustic) with wave vector k propagates back and forth (see Fig. 4.5). The left and right moving fields are represented by $b_L(z,t)$ and $b_R(z,t)$, respectively. Assume the absorption coefficient is α and the reflection coefficients of the two mirrors are $r_1 e^{\phi_1}$ and $r_2 e^{\phi_2}$ where $r_1, r_2 < 1$ and ϕ_1 (ϕ_2) is a random variable describing the phase noise added

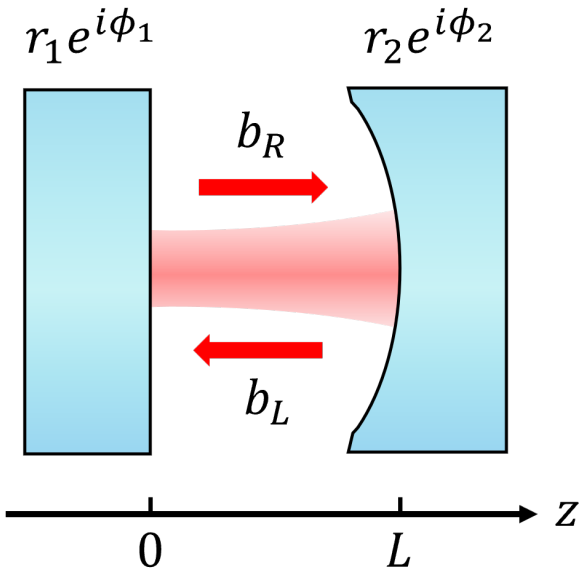

Figure 4.5: Schematic of a wave field propagating inside a FP cavity of length L.

by the reflection of mirror 1 (2). Quite straightforwardly, we have

$$\begin{aligned} b_R(L,t) &= b_R(0,t-T/2)e^{ikL-\alpha L/2}, \\ b_L(0,t) &= b_L(L,t-T/2)e^{ikL-\alpha L/2}, \end{aligned} \tag{4.1}$$

and the boundary condition for the mirror reflection gives

$$\begin{aligned} b_R(0,t) &= b_L(0,t)\cdot r_1 e^{i\phi_1(t)}, \\ b_L(L,t) &= b_R(L,t)\cdot r_2 e^{i\phi_2(t)}, \end{aligned} \tag{4.2}$$

where T is the round-trip propagation time, i.e. $T = 2L/v$. Therefore, after one round of propagation, the field at $z = L$ can be expressed by

$$\begin{aligned} b_R(L,t) &= r_1 r_2 e^{i(\phi_1(t-T/2)+\phi_2(t-T))} e^{-\alpha L+2ikL}\cdot b(L,t-T) \\ &= R e^{i\phi(t)}\cdot b_R(L,t-T). \end{aligned} \tag{4.3}$$

Here r_1 and r_2 represent the surface loss, α represents the bulk loss, $R = r_1 r_2 e^{-\alpha L+2ikL}$, $\phi(t) = \phi_1(t-T/2)+\phi_2(t-T)$ is the stochastic phase noise, which as you will see later,

is the source of pure dephasing. From now on, I will only focus on the dynamics of the field and replace $b_R(z,t)$ with $b(t)$. Using Eq. 4.3 as a recursive relation between fields after one round of propagation, we can get

$$\begin{aligned} b(t=nT) &= Re^{i\phi(t)} \cdot b(t-T) \\ &= R^2 e^{i[\phi(t)+\phi(t-T)]} \cdot b(t-2T) \\ &= ... \\ &= R^n \exp\left[i \sum_{m=0}^{n-1} \phi(t-mT)\right] \cdot b(t=0) \quad (n \geq 0). \end{aligned} \tag{4.4}$$

Therefore, field intensity can be calculated as

$$\begin{aligned} I(t) = \langle b^*(t) b(t) \rangle &= |R|^{2n} I(0) \\ &= (r_1 r_2 e^{-\alpha L})^{2n} I(0) \\ &= I(0) e^{[-\alpha v + \frac{v}{L} \ln(r_1 r_2)]t} \\ &= I(0) e^{-\Gamma_o t} \quad (t \geq 0), \end{aligned} \tag{4.5}$$

where v is the field propagation velocity and $\Gamma_o = \alpha v - \frac{v}{L} \ln(r_1 r_2)$ is the energy dissipation rate. The lifetime is then defined as $\tau_o = 1/\Gamma_o$. Note that the energy dissipation rate is composed of two parts, the bulk contribution αL and the surface contribution $-\frac{v}{L} ln(r_1 r_2)$.

While the stochastic phase noise from the surface doesn't contribute to the phonon dissipation, it makes an important source of dephasing, which is a critical factor especially for quantum applications. coherence time τ_{coh} and decoherence rate Γ_{decoh} are defined to evaluate the dephasing rate of a our phononic resonator. From Eq. 4.4 and Eq. 4.5, we know that the free-induction field can be expressed by

$$b(t) = b(0) \exp\left[-\Gamma_o t/2 + i \sum_{m=0}^{n-1} \phi(t-mT)\right] \quad (t = nT, n \geq 0). \tag{4.6}$$

The coherence property of a field is described by the degree of first-order temporal coherence $g^{(1)}(\tau)$, which is essentially the autocorrelation of $b(t)$. Setting time delay as $\tau = l \cdot T$ (note that τ and l can also be negative), we have

$$\begin{aligned} g^{(1)}(\tau) &= \frac{\langle b^*(t)b(t+\tau)\rangle}{\langle b^*(t)b(t)\rangle} \\ &= \frac{\langle e^{-\Gamma_o t/2}e^{-\Gamma_o(t+\tau)/2}\rangle}{\langle e^{-\Gamma_o t}\rangle}\langle \exp\,[-i\sum_{m=0}^{n-1}\phi(t-mT) + i\sum_{m=0}^{n+l-1}\phi(t-mT)]\rangle, \end{aligned} \tag{4.7}$$

where $\phi(t) = \phi_1(t-T/2)+\phi_2(t-T)$. The first term in Eq. 4.7 is quite straightforward,

$$\frac{\langle e^{-\Gamma_o t/2}e^{-\Gamma_o(t+\tau)/2}\rangle}{\langle e^{-\Gamma_o t}\rangle} = e^{-\Gamma_o\tau/2}\frac{\int_{\max\{0,-\tau\}}^{+\infty} e^{-\Gamma_o t}dt}{\int_0^{+\infty} e^{-\Gamma_o t}dt} = e^{-\Gamma_o|\tau|/2}. \tag{4.8}$$

The second term in Eq. 4.7 is the autocorrelation of the stochastic phase noise. Assuming the phase noise terms $\phi_1(t)$ and $\phi_2(t)$ to be zero-mean stationary Gaussian random variables and independent on each other, then we have

$$\langle \phi_i(t)\rangle = 0, \tag{4.9}$$

$$\langle \phi_i(t)\phi_i(t')\rangle = C_{\phi_i}(t-t'), \tag{4.10}$$

$$\langle f_i(\phi_i(t))\rangle = \langle f_i(\phi_i(t+t_0))\rangle, \tag{4.11}$$

$$\langle f_1(\phi_1)f_2(\phi_2)\rangle = \langle f_1(\phi_1)\rangle \cdot \langle f_2(\phi_2)\rangle, \tag{4.12}$$

where $C_{\phi_i}(t-t')$ is the time autocorrelation function of $\phi_i(t)$ and $f_i(\phi_i)$ is any function

of $\phi_i(t)$. In the case of $\tau \geq 0$, i.e. $l \geq 0$, the second term in Eq. 4.7 can be written as

$$\begin{aligned}\langle \exp[-i\sum_{m=0}^{n-1}\phi(t-mT)+i\sum_{m=0}^{n+l-1}\phi(t-mT)]\rangle &= \langle \exp[-i\sum_{m=0}^{n-1}\phi_1(t-mT)+i\sum_{m=0}^{n+l-1}\phi_1(t-mT)]\rangle \cdot \langle \phi_2 \\ &= \langle \exp[+i\sum_{m=n}^{n+l-1}\phi_1(t-mT)]\rangle \cdot \langle \phi_2 \text{ term}\rangle \\ &= \langle \exp[+i\sum_{m=0}^{l-1}\phi_1(t-mT)]\rangle \cdot \langle \phi_2 \text{ term}\rangle. \end{aligned} \tag{4.13}$$

Since $\phi_1(t)$ obeys the Gaussian probability distribution, so does $\sum_{m=0}^{l-1}\phi_1(t-mT)$. Therefore,

$$\begin{aligned}\langle \exp[+i\sum_{m=0}^{l-1}\phi_1(t-mT)]\rangle &= \exp[-\frac{1}{2}(\sum_{m=0}^{l-1}\phi_1(t-mT))^2] \\ &= \exp[-\frac{1}{2}\sum_{m,m'=0}^{l-1}\phi_1(t-mT)\phi_1(t-m'T)] \\ &= \exp[-\frac{1}{2}\sum_{m,m'=0}^{l-1}C_{\phi_1}((m-m')T)]. \end{aligned} \tag{4.14}$$

Assuming the time autocorrelation of the phase noise to be

$$C_{\phi_1}(t-t') = \langle \phi_1^2 \rangle e^{-\gamma|m-m'|T/2}, \tag{4.15}$$

then we have

$$\begin{aligned}\exp[-\frac{1}{2}\sum_{m,m'=0}^{l-1} C_{\phi_1}((m-m')T)] &= \exp[-\frac{\langle\phi_1^2\rangle}{2}\sum_{m,m'=0}^{l-1} e^{-\gamma|m-m'|T/2}] \\ &= \exp[-\frac{\langle\phi_1^2\rangle}{2}(l+2\sum_{m=0}^{l-1}\sum_{m'=0}^{m-1} e^{-\gamma(m-m')T/2})] \\ &= \exp[-\frac{\langle\phi_1^2\rangle}{2}(l-2\sum_{m=0}^{l-1}\frac{1-e^{-m\gamma T/2}}{1-e^{\gamma T/2}})] \\ &= \exp[-\frac{\langle\phi_1^2\rangle}{2}(l-\frac{l}{2(1-e^{\gamma T/2})}+\frac{1-e^{-l\gamma T/2}}{2(1-e^{\gamma T/2})(1-e^{-\gamma T/2})})].\end{aligned} \tag{4.16}$$

If the phase noise can be treated as a Markovian process, i.e. $\gamma T \gg 1$, then its autocorrelation can be simplified to be

$$\exp[-\frac{1}{2}\sum_{m,m'=0}^{l-1} C_{\phi_1}((m-m')T)] = \exp[-\frac{l\langle\phi_1^2\rangle}{2}], \tag{4.17}$$

and the second term in Eq.4.7 is

$$\langle\exp[-i\sum_{m=0}^{n-1}\phi(t-mT)+i\sum_{m=0}^{n+l-1}\phi(t-mT)]\rangle = \exp[-\frac{l}{2}(\langle\phi_1^2\rangle+\langle\phi_2^2\rangle)]. \tag{4.18}$$

Similarly, when $\tau<0$, i.e. $l<0$, we get

$$\begin{aligned}\langle\exp[-i\sum_{m=0}^{n-1}\phi(t-mT)+i\sum_{m=0}^{n+l-1}\phi(t-mT)]\rangle &= \langle\exp[-i\sum_{m=0}^{-l-1}\phi_1(t-mT)]\rangle\cdot\langle\exp[-i\sum_{m=0}^{-l-1}\phi_2(t-mT)\\ &= \exp[+\frac{l}{2}(\langle\phi_1^2\rangle+\langle\phi_2^2\rangle)].\end{aligned} \tag{4.19}$$

Therefore, generally the second term in Eq. 4.7 can be written as

$$\langle\exp[-i\sum_{m=0}^{n-1}\phi(t-mT)+i\sum_{m=0}^{n+l-1}\phi(t-mT)] = \exp[-\frac{|l|}{2}(\langle\phi_1^2\rangle+\langle\phi_2^2\rangle)] \tag{4.20}$$

Substituting this and Eq. 4.8 back to Eq. 4.7, we obtain

$$\begin{aligned} g^{(1)}(\tau) &= \exp\left[-\frac{\Gamma_o|\tau|}{2} - \frac{|l|}{2}(\langle\phi_1^2\rangle + \langle\phi_2^2\rangle)\right] \\ &= \exp\left[(-\frac{\Gamma_o}{2} - \frac{v}{4L}(\langle\phi_1^2\rangle + \langle\phi_2^2\rangle))|\tau|\right] \\ &= e^{-\Gamma_{\text{decoh}}|\tau|/2}, \end{aligned} \tag{4.21}$$

where the decoherence rate is a sum of dissipation rate and pure dephasing rate, i.e. $\Gamma_{\text{decoh}} = \Gamma_o + \Gamma_\phi$, and the pure dephasing is expressed by $\Gamma_\phi = \frac{v}{2L}(\langle\phi_1^2\rangle + \langle\phi_2^2\rangle)$. At last, the coherence time is defined as

$$\tau_{\text{coh}} = \int_{-\infty}^{\infty} (g^{(1)}(\tau))^2 d\tau = \frac{2}{\Gamma_{\text{decoh}}}. \tag{4.22}$$

Realize that when there is no pure dephasing ($\Gamma_\phi = 0$), the decoherence rate is equal to the dissipation rate ($\Gamma_{\text{decoh}} = \Gamma_o$), while the coherence time is twice the lifetime ($\tau_{\text{coh}} = 2\tau_o$), same as $T_2 = 2T_1$ for a two-level system.

4.4.2 Power spectral density with dephasing

As is demonstrated in the last secion, phonon coherence for an open system is determined by both energy dissipation and dephasing. In this section, we will model the power spectral density (PSD) of the phonon field regarding the existence of both mechanisms. Consider a phonon field $b(t) = \Theta(t)\exp(-\Gamma_o t/2 - i\Omega_o t - i\phi(t))$, where $\Theta(t)$ is the Heaviside step function, Ω_o is its oscillating frequency and $\phi(t)$ is a random variable that models the phase noise. Then its intensity can be expressed as $I(t) =< b^\dagger(t)b(t) >= e^{-\Gamma_o t}$, where $\tau_o = 1/\Gamma_o$ is the lifetime. We calculate the degree

of first-order temporal coherence

$$\begin{aligned} g^{(1)}(\tau) &= \frac{\langle b^\dagger(t)b(t+\tau)\rangle}{\langle b^\dagger(t)b(t)\rangle} \\ &= \frac{\int_{\max\{0,-\tau\}}^{+\infty} e^{-\Gamma_o t/2+i\Omega_o t+i\phi(t)}\cdot e^{-\Gamma_o(t+\tau)/2-i\Omega_o(t+\tau)-i\phi(t+\tau)}dt}{\int_0^{+\infty} e^{-\Gamma_o t}dt} \\ &= e^{-\Gamma_o|\tau|/2-i\Omega_o\tau}\langle e^{-i\Delta\phi(\tau)}\rangle \end{aligned} \tag{4.23}$$

where $\Delta\phi(\tau) = \phi(t+\tau) - \phi(t)$. Assume $\Delta\phi(\tau)$ represents stationary Gaussian noise, i.e. $P(\Delta\phi(\tau)) = \frac{1}{\sqrt{2\pi}\sigma}e^{-[\Delta\phi(\tau)]^2/2\sigma^2}$, where the variance $\sigma^2 = \langle[\Delta\phi(\tau)]^2\rangle$. Therefore,

$$\begin{aligned} \langle e^{-i\Delta\phi(\tau)}\rangle &= \int_{-\pi}^{+\pi} e^{-i\Delta\phi(\tau)}P(\Delta\phi(\tau))\cdot d(\Delta\phi(\tau)) \\ &= \frac{1}{\sqrt{2\pi}\sigma}\int_{-\infty}^{+\infty} e^{-i\Delta\phi(\tau)}e^{-[\Delta\phi(\tau)]^2/2\sigma^2}\cdot d(\Delta\phi(\tau)) \\ &= e^{-\sigma^2/2} \\ &= e^{-\langle[\Delta\phi(\tau)]^2\rangle/2}. \end{aligned} \tag{4.24}$$

We can then rewrite $g^{(1)}(\tau)$ as

$$g^{(1)}(\tau) = e^{-\Gamma_o|\tau|/2-i\Omega_o\tau}e^{-\langle[\Delta\phi(\tau)]^2\rangle/2}. \tag{4.25}$$

Then, according to the Wiener–Khinchin theorem, the one-sided PSD of the phonon field can be expressed as

$$\begin{aligned} S_{bb}[\Omega] &= 2\int_{-\infty}^{+\infty} g^{(1)}(\tau)\cos\Omega\tau\cdot d\tau \\ &= 2\int_{-\infty}^{+\infty} d\tau\cdot\cos\Omega\tau\cdot e^{-\Gamma_o|\tau|/2-i\Omega_o\tau}e^{-\langle[\Delta\phi(\tau)]^2\rangle/2} \\ &= 4\int_0^{+\infty} d\tau\cdot\cos\Omega\tau\cos\Omega_o\tau\cdot e^{-\Gamma_o|\tau|/2}e^{-\langle[\Delta\phi(\tau)]^2\rangle/2}. \end{aligned} \tag{4.26}$$

On the other hand, by definition, $\langle[\Delta\phi(\tau)]^2\rangle = \langle[\phi(t+\tau)-\phi(t)]^2\rangle = 2[\langle\phi^2(t)\rangle - \langle\phi(t)\phi(t+\tau)\rangle]$. Realize that $\langle\phi(t)\phi(t+\tau)\rangle$ is the auto-correlation function of $\phi(t)$.

According to the Wiener-Khinchin theorem, it also forms a Fourier pair with the one-sided PSD of the phase function $S_{\phi\phi}[\Omega]$ as

$$\langle \phi(t)\phi(t+\tau)\rangle = \frac{1}{2\pi}\int_0^{+\infty} S_{\phi\phi}[\Omega]\cos\Omega\tau \cdot d\Omega \tag{4.27}$$

Thus,

$$\begin{aligned}\langle[\Delta\phi(\tau)]^2\rangle &= \frac{1}{\pi}\int_0^{+\infty} S_{\phi\phi}[\Omega](1-\cos\Omega\tau)\cdot d\Omega \\ &= \frac{2}{\pi}\int_0^{+\infty} S_{\Omega\Omega}[\Omega](\frac{\sin^2\Omega\tau/2}{\Omega^2})\cdot d\Omega.\end{aligned} \tag{4.28}$$

Substituting it back to eq.(4.26), we obtain

$$\begin{aligned}S_{bb}[\Omega] &= 4\int_0^{+\infty} d\tau\cdot\cos\Omega\tau\cos\Omega_o\tau\cdot e^{-\Gamma_o|\tau|/2}e^{-\langle[\Delta\phi(\tau)]^2\rangle/2} \\ &= 4\int_0^{+\infty} d\tau\cdot e^{-\Gamma_o|\tau|/2}\cos\Omega\tau\cos\Omega_o\tau\cdot\exp\{-\frac{1}{\pi}\int_0^{+\infty} S_{\Omega\Omega}[\Omega']\cdot\frac{\sin^2\Omega'\tau/2}{\Omega'^2}\cdot d\Omega'\}.\end{aligned} \tag{4.29}$$

The last step uses the relation $S_{\phi\phi}[\Omega] = S_{\Omega\Omega}[\Omega]/\Omega^2$ as $\Omega(t) = \dot{\phi}(t)$.

Now let's take the example of white frequency noise, i.e. $S_{\Omega\Omega}[\Omega] = \gamma$ a constant. Therefore, the PSD of the phonon field can be calculated as

$$\begin{aligned}S_{bb}[\Omega] &= 4\int_0^{+\infty} d\tau\cdot e^{-\Gamma_o|\tau|/2}\cos\Omega\tau\cos\Omega_o\tau\cdot\exp\{-\frac{1}{\pi}\int_0^{+\infty} S_{\Omega\Omega}[\Omega']\cdot\frac{\sin^2\Omega'\tau/2}{\Omega'^2}\cdot d\Omega'\} \\ &= 4\int_0^{+\infty} d\tau\cdot e^{-\Gamma_o|\tau|/2}\cdot\cos\Omega\tau\cos\Omega_o\tau\cdot e^{-\gamma|\tau|/4} \\ &= 2\int_0^{+\infty} d\tau\cdot e^{-\Gamma_{\text{decoh}}|\tau|/2}\cdot[\cos(\Omega-\Omega_o)\tau+\cos(\Omega+\Omega_o)\tau] \\ &= \frac{1}{\Gamma_{\text{decoh}}/2 - i(\Omega-\Omega_o)} + \frac{1}{\Gamma_{\text{decoh}}/2 + i(\Omega-\Omega_o)} \\ &= \frac{\Gamma_{\text{decoh}}}{(\Gamma_{\text{decoh}}/2)^2 + (\Omega-\Omega_o)^2}\end{aligned} \tag{4.30}$$

where $\Gamma_{\text{decoh}} = \Gamma_o + \gamma/2$ describing the decoherence rate, and we neglect the negative frequency component since it's one-sided PSD. We realize that under the assumption of white Gaussian frequency noise, the PSD of the phonon field is Lorentzian and its linewidth is the sum of energy dissipation rate and a dephasing term, i.e. $\Delta\Omega = \Gamma_{\text{decoh}} = \Gamma_o + \Gamma_\phi$. Here $\Gamma_\phi = \gamma/2$ is half of the one-sided PSD of the phase noise.

4.4.3 Bulk vs. surface loss

From the above two sections, we know that linewidth $\Delta\nu$ of the power spectral density measures its decoherence rate Γ_{decooh} and the decoherence rate Γ_{decooh} is the sum of the energy dissipation rate Γ_o and the pure dephasing rate Γ_ϕ, i.e.

$$\Delta\nu = \Gamma_{\text{decoh}}/2\pi = (\Gamma_o + \Gamma_\phi)/2\pi. \tag{4.31}$$

The energy dissipation rate can be identified with the phonon ring-down experiment as $\Gamma_o = \Omega_{\text{ph}}/Q_{\text{ring-down}} = 1/\tau_o$. As we can see from both Fig. 4.2 and Fig. 4.4, the spectral Q-factors (Q_{spectral}) of our μHBAR devices are always equal to the ring-down Q-factors ($Q_{\text{ring-down}}$), which indicates $\Gamma_{\text{decoh}} = \Gamma_o$. Thus, the pure dephasing in our μHBAR system is negligible, i.e. $\Gamma_\phi = 0$, and the decoherence rate is determined primarily by the energy dissipation rate.

Both surface and bulk interactions contribute to phonon dissipation, as can be seen in Eq. 4.5. The bulk contribution $\Gamma_o^{\text{bulk}} = \alpha v$ is independent of the substrate thickness L, while the surface contribution $\Gamma_o^{\text{surf}} = -\frac{v}{L}\ln(r_1 r_2)$ is inversely proportional to L. Assuming a fractional energy loss per reflection of $l_1, l_2 \ll 1$ for the two resonator surfaces, then the reflection coefficients become $r_1 = \sqrt{1-l_1}, r_2 = \sqrt{1-l_2}$ and the surface loss rate becomes $\Gamma_o^{\text{surf}} = \frac{v}{2L}(l_1 + l_2) = (l_1 + l_2) \times \text{FSR}$, where $\text{FSR} = \frac{v}{2L}$ is the acoustic free spectral range and v is the longitudinal acoustic velocity. Therefore,

the total phonon-dissipation-limited Q-factor can be written as

$$\frac{1}{Q_{\text{tot}}} = \frac{1}{Q_{\text{bulk}}} + \frac{v(l_1 + l_2)}{2L}. \tag{4.32}$$

When bulk loss is negligible, i.e. $Q_{\text{bulk}} = \infty$, we have $Q_{\text{tot}} = \frac{2L}{v(l_1+l_2)}$. This is exactly what we saw in Fig. 4.4c. Using Eq. 4.32 to analyze the measured Q-factors of μHBAR devices of 6 thicknesses, we get $Q_{\text{bulk}} = \infty$ and $l_1 + l_2 = 500$ ppm. If we assume symmetric losses from both surfaces, i.e. $l_1 = l_2 = l$, then we get the surface loss from each surface reflection of $l = 250$ ppm, and the finesse of $F = \pi/l = 12,560$.

There are various types of surface interactions that could contribute to this 250 ppm loss, including surface roughness scattering, subsurface dislocations, impurity scattering, etc. Identification of the dominating loss channel requires careful material and structure investigation. In next chapter, I will introduce some powerful analyzing tools such as secondary ion mass spectroscopy (SIMS) and X-ray diffraction (XRD) to study the surface condition and report a special kind of surface treatment that yields significant remediation of surface/subsurface damages.

Chapter 5

Surface characterization and treatment

5.1 Various sources of surface losses

From the studies in Chapter 4, we have identified

- There is negligible pure dephasing in our μHBAR system, and the phonon coherence is limited primarily by the phonon loss.
- The phonon loss is dominated by the surface interaction.

However, there are a variety of surface interactions that can affect phonon dissipation. The first thing that comes to mind is surface roughness scattering, which is relatively easy to model. Assuming the surface height profile as a zero-mean Gaussian random noise with variance σ and zero correlation (white noise), the reflectivity R can be expressed by $R = e^{-(2k\sigma)^2}$ [27]. Therefore, the phonon scattering loss per reflection is $l = 1 - R \approx (\frac{4\pi\sigma}{\lambda_{\text{ph}}})^2$, where the λ_{ph} is the phonon wavelength. The surface roughness was measured with an optical profilometer (see Fig. 2.6c) to be $\sigma = 0.25$ nm and $\lambda_{\text{ph}} = 500$ nm, then the phonon loss per reflection is calculated to be 40 ppm. Recall

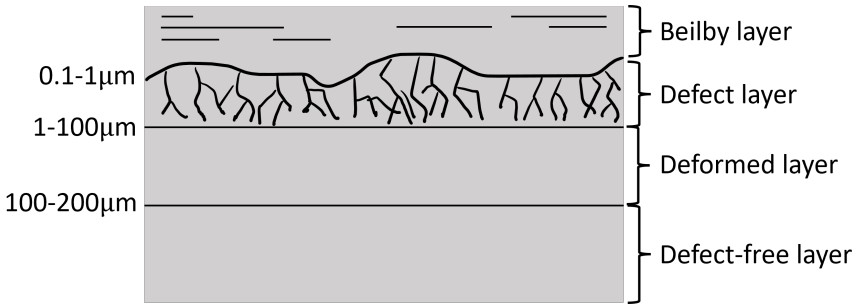

Figure 5.1: Sketch of the subsurface damages of a processed substrate.

that the total loss per surface reflection from our experiment is 250 ppm, of which the surface roughness scattering only makes 16%. Where does the rest 84% of surface loss come from?

To answer this question, it is worthwhile to take a look at the manufacture of the quartz substrates. The quartz substrates we fabricated the μHBAR devices on were purchased from China Quartz Technology. Single-crystalline quartz is usually grown out of melted high-purity quartz power using a hydrothermal synthesis method. Then it is cut into thin slices using diamond wire saws. In order to achieve good parallelism between two surfaces and minimal surface roughness, it needs to go through multiple steps like lapping, grinding and polishing. Each of these processes will unavoidably introduce contamination and structure disorders in a very thin layer under the surface, called the subsurface damages. Fig. 5.1 shows you the subsurface damages of a process substrates. Starting from the very surface, which is also the surface we usually see from an optical profilometer or AFM image, this is called the Beilby layer. The Beilby layer is a thin, amorphous surface layer that forms on materials during polishing or mechanical finishing processes. It is typically in the range of a few nanometers to micrometers depending on the polishing method and material, and forms on various materials, including metals, semiconductors, and ceramics. Because it has different material constituents, it can cause phonon dissipation via scattering. Below the Beilby layer, there is the damaged quartz surface layer with a lot of defects caused by the

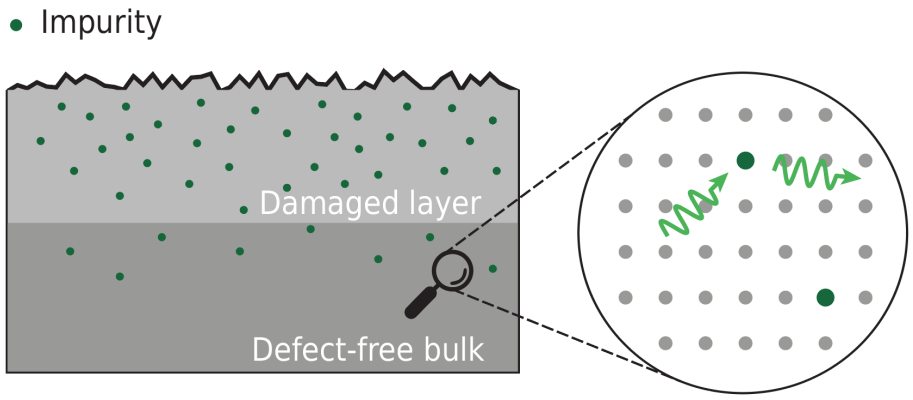

Figure 5.2: schematic of impurity scattering of phonon wave.

lapping, grinding and polishing processes. As one goes deeper, you might not find as many defects while instead you will see distorted lattice structures. This deformed layer can extend quite far into the bulk ($\sim$ 100 μm), beyond which you will finally reach the defect-free bulk quartz crystal.

Note that this sketch is very rough and the depth of each layer can vary significantly from substrate to substrate. Besides the structure disorder, impurity contamination can be and will be introduced into the subsurface in each of the very same processes, which also serves as point scatterers for phonons. Moreover, surface and subsurface damages can happen during our fabrication procedure, especially during the last step, the RIE process. The high-energy plasma during the RIE process will unavoidably imprint impurity ions into the subsurface of the substrate as well as break Si-O bonds causing lattice dislocations. At last, there is no such thing as defect-free bulk crystal. Anyways, following what the experiment results in Chapter 4 have indicated, I will focus on the surface and subsurface damages in this chapter.

5.2 Surface contamination

Contamination can happen in every step since the growth of the quartz crystal, while surface/subsurface contamination happens mostly during surface treatments such as

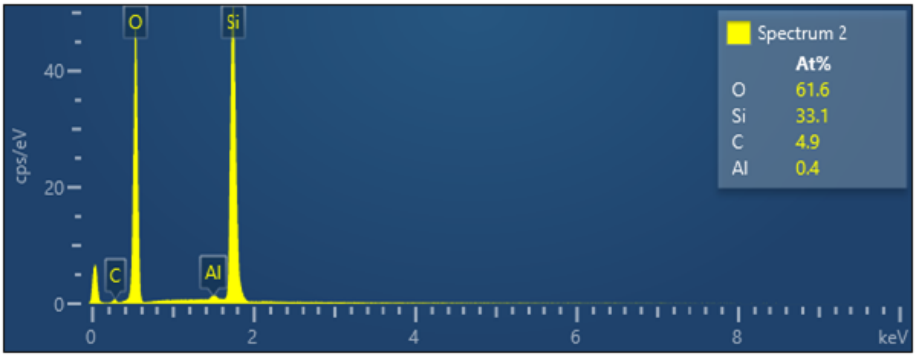

Figure 5.3: EDX results of a quartz blank, showing 4.9% C and 0.4% Al.

lapping, polishing, and surface etching. Common contaminants include C, H, Al, Fe, Na. Since the etching gas we use during the RIE process is SF6, we also expect S and F found as impurities in a thin subsurface layer. The impurity atoms are individual point scatterers and cause phonon dissipation (Fig. 5.2).

To investigate the impurity concentration, we first did energy-dispersive X-ray (EDX) spectroscopy which focuses a beam of electrons into the sample to stimulate the emission of characteristic X-rays. The advantage of this method is that it can quantitative measure the elemental composition. However, it is not as sensitive as the next method we are gonna talk about and doesn't not provide depth profile information. Fig. 5.3 shows the EDX result of a quartz blank. Except for the two constituent elements Si and O, we also observe impurity peaks of C and Al. Since electron has a very small penetration depth ($\sim$nm) in quartz, the chemical composition is only for few-nm-thick layer on the surface, which lies well within the Beilby layer in Fig. 5.1. As we discussed before, the Beilby layer is a thin amorphous surface layer that forms on materials during polishing or mechanical finishing processes, and it can have a very different chemical composition from the bulk material, quartz in this context. You can see it from Fig. 5.3 that the peak ratio of Si (33.1%) and O (61.6%) is not strictly 1:2. Moreover, we find that in this thin layer, C is the most significant contaminant with nearly 5% concentration, followed by Al which has a 0.4% concentration.

Secondary ion mass spectroscopy (SIMS) is a more sensitive method for chemical analysis. Equipped with an ion gun to remove material, it has the capability to do depth profiling of impurity concentration. Fig. 5.4 shows the depth profiles of different impurity concentrations for one blank substrate (before etch), and one fabricated substrate (after etch). Both come from the same batch of 2-mm-thick quartz substrates. For the fabricated substrate, SIMS is done on the dome side, i.e. the RIE-processed side. A significant amount of impurities such as C, Al, F, Na, Fe are observed. The total milling time with the ion gun is 1500 sec, corresponding to a thickness of 40 nm.

As you can see from Fig. 5.4, the RIE-processed device shows decreased concentrations of Al, Na, and Fe. These impurities are imprinted into the substrate surface by native grinding and polishing. By removing material with the high-energy plasma, RIE process reduces the amount of native impurities. On the other hand, the high-energy plasma, containing mostly SF6 and Ar, implants impurity elements into the substrate surface as well. This is why the concentration of F is much higher in the device than in the blank substrate. At last, C shows almost the same level of concentration but a different distribution, because C exists in the native substrate and can be introduced by the high-energy plasma. Therefore the RIE process didn't reduce its total concentration but changed its distribution instead.

5.3 Subsurface lattice structure disorder

5.3.1 Basics of grazing-incidence X-ray diffraction (GIXRD)

Procedures such as lapping, polishing and RIE, does not only introduce impurity contamination into the sample substrate, but also cause subsurface lattice disorders which include lattice dislocation and elastic deformation. X-ray diffraction (XRD) is an excellent method to study crystallinity and lattice deformation [39]. The working

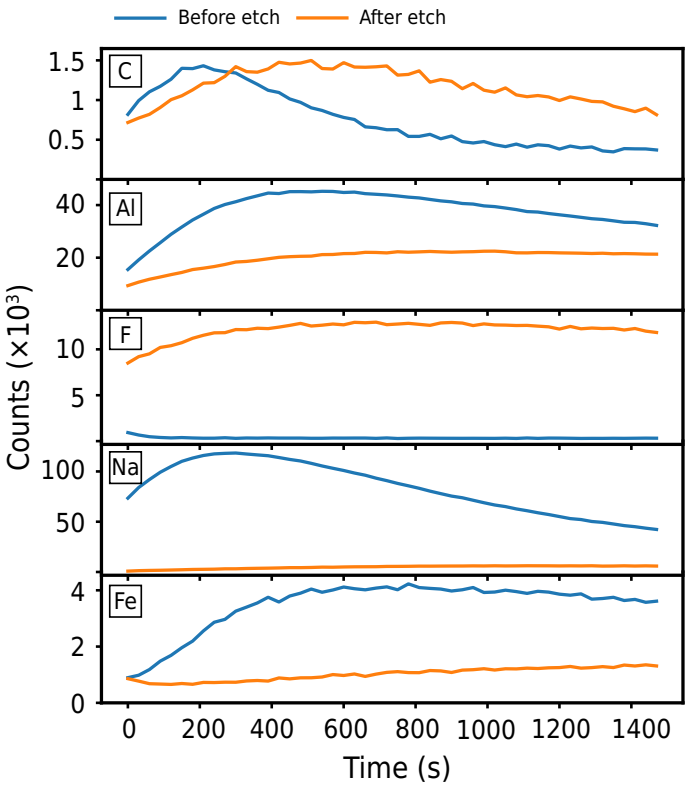

Figure 5.4: SIMS results before and after RIE process.

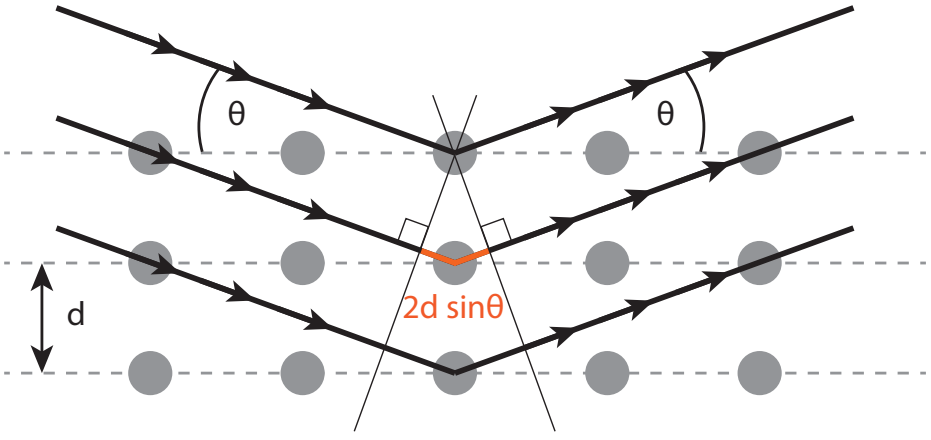

Figure 5.5: Principle of X-ray diffraction: the Bragg's law.

principle of XRD relies on the constructive interference of reflected X-ray beam from two atomic planes, which is visualized in Fig. 5.5. Assuming the X-ray beam with a wavelength of λ, is incident at an angle θ onto a series of atomic planes of spacing d. The reflected X-ray beam also has an angle of θ with respect to the crystalline plane. The relative optical path difference between X-ray beams scattered off two adjacent crystalline planes is given by $2d\sin\theta$, as marked in orange in Fig. 5.5. Constructive interference requires this optical path difference to be multiples of the X-ray wavelength λ, also called the Bragg condition. Therefore, the diffraction angles θ_{B} for Bragg reflection have to satisfy the following condition,

$$2d_{hkl}\sin\theta_{\mathrm{B}} = m\lambda. \tag{5.1}$$

Eq.5.1 is also knows as the Bragg equation. θ_{B} is referred to as the Bragg angle, and d_{hkl} refers to the interplanar spacing between crystallographic planes with Miller indices $[h, k, l]$. m is an integer and is referred to as the order of the diffraction maxima, with m = 1 being the first order, and m = 2 being the second order, and so on. The Bragg equation relates the angular position of diffracted X-rays to the lattice spacing and is the basis for all XRD measurements.

The penetration depth of X-ray is typically 1-100 μm. However, the subsurface damages in our µHBAR substrates lie within a very thin layer of a few microns. In a standard angular scan, the diffraction peak from the bulk substrate typically dominates the resultant pattern. In GIXRD, the incident angle ω is fixed to a small angle of $\sim 1^\circ$ with respect to the substrate surface. As you will see later, since the Bragg plane under study is not necessarily parallel to the substrate surface, the reflected angle is not always equal to the incident angle. The XRD machine (Rigaku) we use has a Cu K-α line (1.54 Å or 8.05 keV) and has a Ge (220)*2 filter to enable high-resolution XRD measurement. Fig. 5.6 shows the calculated penetration depth

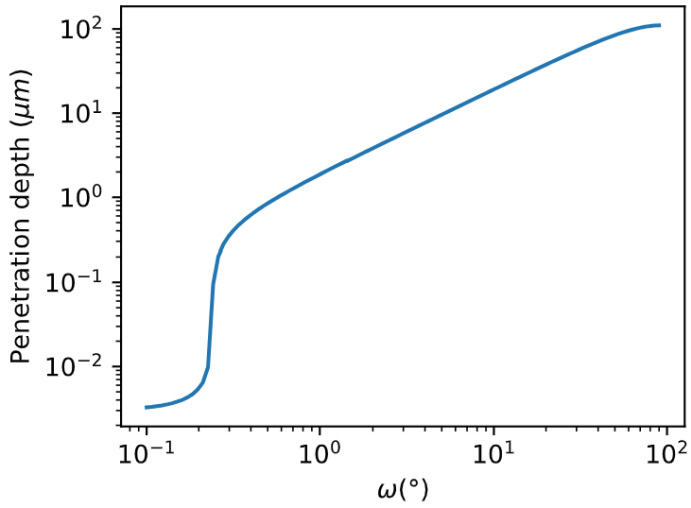

Figure 5.6: Penetration depth of X-ray at incidence angle from 0.1 to 90° (normal incidence). The X-ray energy is set as 8.05 keV. Material is set to be SiO2 with density of 2.65 g/cm3.

of X-ray beam at different incident angles based on the wavelength and density of the substrate material. The steep transition at $\omega \approx 0.2°$ is due to total reflection of X-ray. The refractive index of material is typically smaller than 1. Therefore, when an X-ray beam is incident from air to material, there is a critical angle below which the X-ray will be totally reflected. In our experiment, the incident angle is set to be $\omega \approx 1°$, so that the penetration depth will be $\sim 1\mu m$.

5.3.2 Rocking curve

The GIXRD provides a selective method that focuses only on the top 1-μm-thin layer of material. In this section, I will explain the measurement we did to investigate the subsurface damages. It is called the rocking curve. We first need to pick a Bragg diffraction peak with decent intensity. In a rocking curve, the Bragg angle $2\theta_{\mathrm{B}}$ is fixed to the center of this particular diffraction peak, and the sample is tilted in the ω axis such that Bragg planes are no longer parallel with its optimal position (see Fig. 5.7). This result is a single bell curve, known as a rocking curve, which gives the distribution of planes as a function of tilt. The width of the rocking curve depends

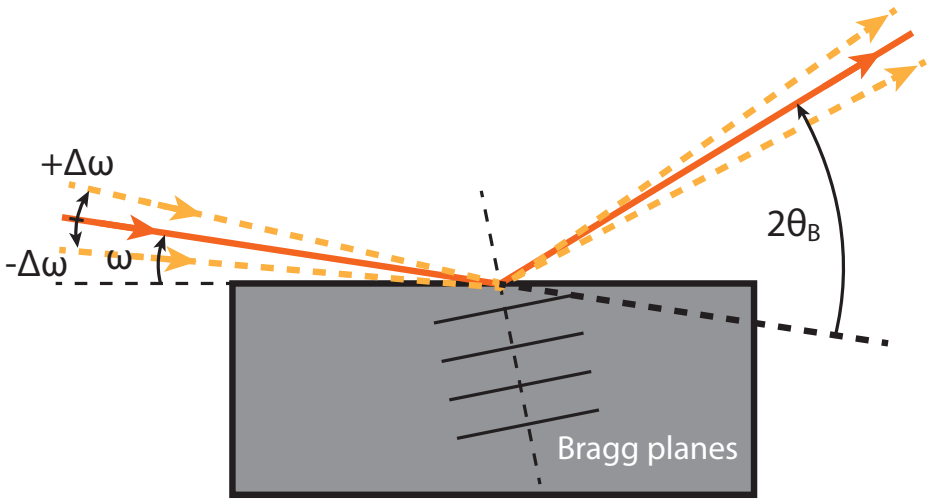

Figure 5.7: Schematic of a rocking curve measurement.

upon the mosaic spread of the grains, density of dislocations, and elastic deformation, which disrupt the parallel nature of the lattice planes. Therefore, the width of the rocking curve is generally used as an indication of the crystallinity [39, 40].

5.4 Surface remediation and improved phonon coherence

Given that the quartz substrates received from the vendor have native damages under the surface, we have tried several approaches to remediation of the crystal surface, which include etching, annealing, and polishing of crystal surfaces. However, among all of these, only repolishing of the crystal surface using a carefully optimized process produced a significant improvement in phonon coherence times. The polishing was done with a Multiprep^{TM} polishing machine with Red Final C adhesive back disc from Allied High Tech Products Inc. An aqueous polishing suspension with pH value of 10 has been applied during the polishing. It relies on the 40 nm colloidal fused silica grits for gently polishing the quartz surface. High-resolution GIXRD rocking curve has been recorded as we polish a brand-new quartz blank (Fig. 5.8). This rocking

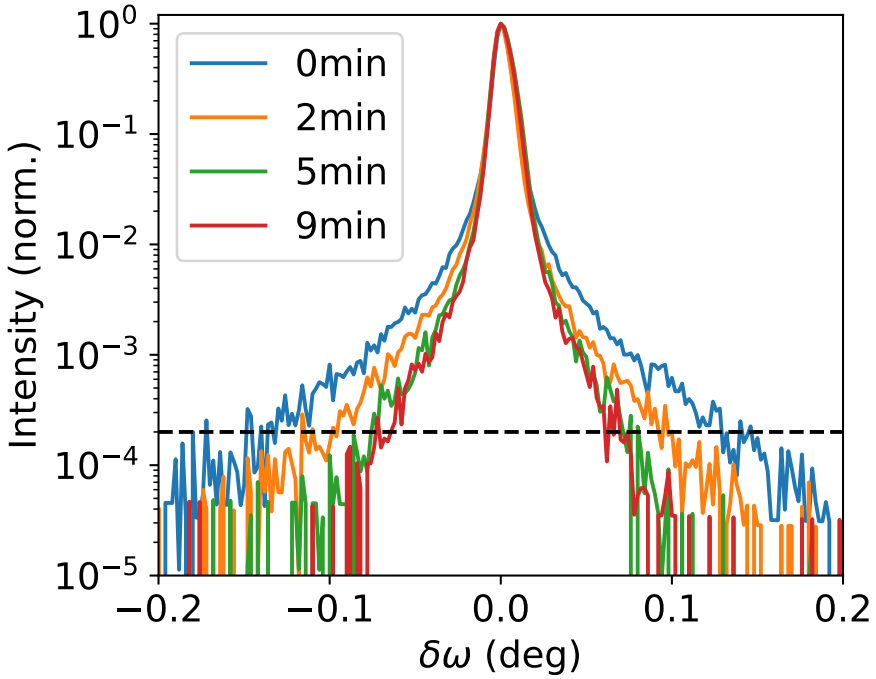

Figure 5.8: GIXRD rocking curves of quartz substrate after polishing for 0, 2, 5, and 9 min.

curve is associated with the $[0, -2, 3]$ Bragg plane, the incident angle is centered at 0.91°, and the Bragg angle is fixed at 68.15°. Because the contrast is so tiny, here we compare the angular width as the full width at 1/5000th maximum (FW5000M) instead of FWHM. Before polishing, the as-received substrate surface shows a angular width of 0.260°. As we polish the surface, the rocking curve gets narrowed down. Eventually, after 9 minutes of polishing, this rocking curve converges and angular width gets reduced to a lower value 0.126°, indicating that the X-rays are sampling a more regularly ordered lattice in the thin subsurface layer.

As we optimize the polishing process, we also keep track of the surface topography. We use atomic force microscopy (AFM) to get high-resolution profiles of the substrate surface. Fig. 5.9a shows an AFM image of a brand-new quartz blank in a field of view (FOV) of 10 by 10 μm. The root-mean-square (RMS) roughness σ_{RMS} is measured to be 0.60 nm. Besides, polishing lines from the manufacture can be

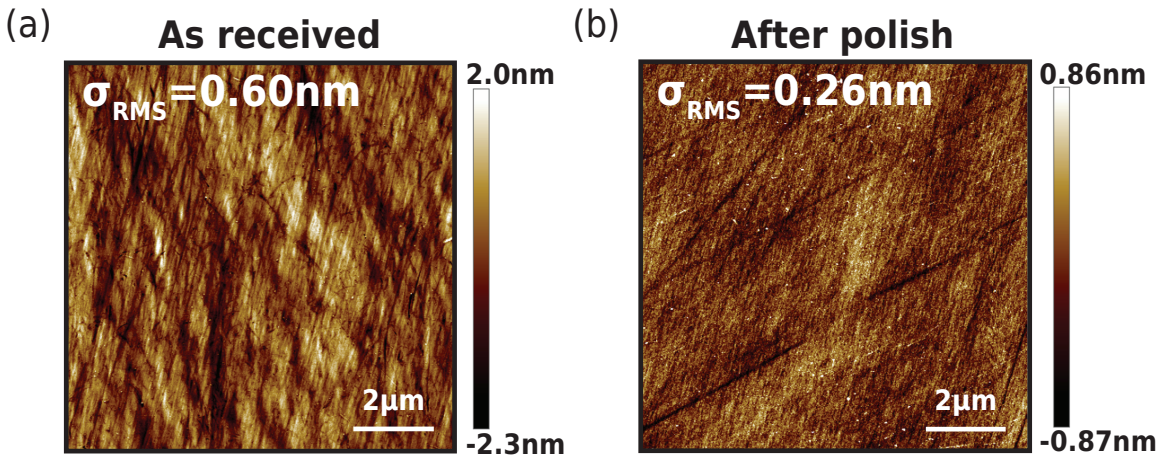

Figure 5.9: (a) AFM image of brand-new substrate. (b) AFM image of polished quartz substrate.

clearly seen. These polishing lines have typical widths ranging from 10-100 nm, and are not observable under the optical profilometer. Since they are smaller structures than half of the phonon wavelength (250 nm), in principle they are not strong phonon scatterers by themselves. However, the study of polishing mechanism suggests that following each of those polishing lines, there are numerous lattice distortions underneath which can affect a volume much larger than the size of the polishing scratches via plastic deformation (dislocations) of the crystal lattice, thus could have a much more significant effect on intra-cavity phonons. Fig. 5.9b shows an AFM image of a quartz blank after our optimized polishing process. It reveals much less pronounced polishing lines with an RMS surface roughness of 0.26 nm.

Narrower angular width from the GIXRD rocking curve and smoother surface from the AFM images both suggest that we now have better surface and subsurface conditions in the repolished samples. Next, we apply this optimized polishing process on the back side (flat surface) of the fabricated μHBAR devices and check the phonon coherence.

We applied the optimized polishing on the back side of two μHBAR substrates, a 2.5-mm-thick one and a 3-mm-thick one. The measured Q-factors are plotted in

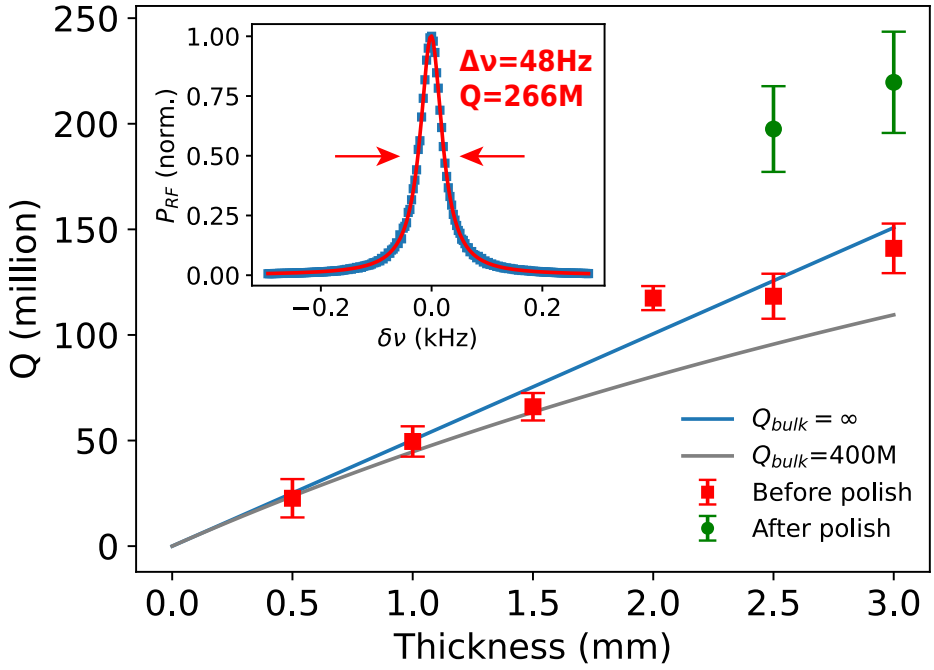

Figure 5.10: Summary of measured Q-factors of μHBARs with backside polished. Inset: Phonon spectrum of the highest-Q μHBAR resonator on a 3-mm-thick substrate.

Fig. 5.10 (green) together with the data before polishing. Both substrates show significant improvements. The average Q-factor of the 2.5-mm-thick substrate is improved from 103 million to 195 million, and the 3-mm-thick substrate is improved from 141 million to 209 million. From the measured Q-factors, we can calculate the total surface loss in a round trip. Assuming symmetric losses coming from both surfaces before the polish, one can estimate the fractional loss reduction directly by the polishing, as summarized in Table 5.1. On average, we obtain a 94% loss reduction from the 2.5-mm-thick μHBAR substrate and a 65% loss reduction from the 3-mm-thick substrate. Since we have demonstrated significant improvements in phonon Q-factors just by polishing the back side, a natural next thing to do is to polish both surfaces of the brand-new substrates before any fabrication. If we can obtain the same loss reduction from the front (dome) side of the 2.5-mm-thick substrate as well, i.e. $l = 17$ ppm for both the front and back side reflection, the total Q-factor will be $Q = \frac{2\pi L}{\lambda_{\rm ph} l} = 1.85 \times 10^9$ and the phonon coherence time will be $\tau_{\rm coh} = 46$ ms! Similar

estimation for the 3-mm-thick substrate gives $Q = 0.4 \times 10^9$ and $\tau_{\text{coh}} = 10$ ms.

Sample	Q-factor before/after polish	loss from back surface before/after polish	fractional loss reduction by polishing
2.5 mm substrate	103M / 195M	305ppm / 17ppm	94%
3.0 mm substrate	141M / 209M	268ppm / 93ppm	65%

Table 5.1: Comparison of measured Q-factors and surface losses before and after backside polish.

We did a double-side polishing on a 3-mm-thick quartz substrate and fabricate µHBARs on it. The measured Q-factors are summarized in Fig. 5.11. The inset in Fig. 5.11b shows the measured spectral Q-factors of all 9 µHBAR devices on this substrate. The average Q-factor is 286 million. Individual µHBAR shows a record-high Q-factor of 360 million, corresponding a coherence time of 9 ms and a record-level f-Q product of 4.56×10^{18} Hz. (Fig. 5.11a) This is euqal to a round-trip loss of 210 ppm, or 105 ppm per surface reflection. Fig. 5.11 shows the ring-down of the same µHBAR which yields a lifetime of 4.68 ms and a Q-factor of 372 million. The difference between the spectral Q and ring-down Q is only 3%. Therefore, the phonon coherence in our best µHBAR device is still limited by phonon dissipation from the surface.

5.5 RIE-introduced phonon loss

In the previous sections, we have demonstrated a systematic way to improve phonon coherence in our µHBAR devices, including careful surface diagnosis and treatments. In this section, I want to discuss RIE-caused surface damage and RIE-introduced phonon loss. RIE is an must-have procedure in the fabrication of µHBARs, as well as in the fabrication of many other types of phononic resonators. Therefore, to figure out the extra phonon loss caused by RIE is of vital importance.

We did two experiments to study the RIE-introduced loss to our µHBAR devices. Recall that in our fabrication recipe, we measured the dome height of the photore-

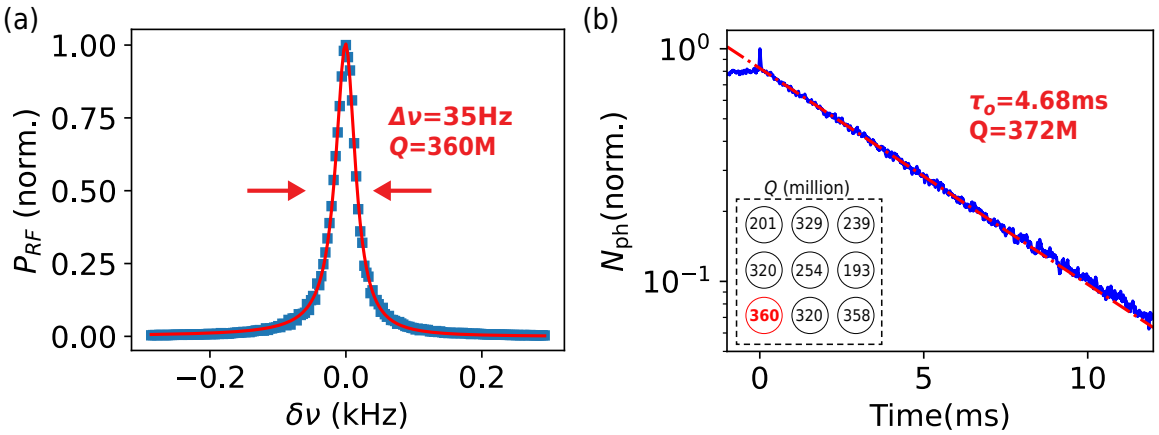

Figure 5.11: Phonon measurements of double-side polished 3-mm-thick µHBARs. (a) Phonon spectrum of individual µHBAR with a linewidth of 35 Hz and a Q-factor of 360 million. (b) Phonon ring-down of the same µHBAR in (a), showing a lifetime of 4.68 ms and a ring-down Q of 372 million. Inset: Summary of measured spectral Q-factors of all 9 µHBAR devices on this 3-mm-thick double-side polished substrate.

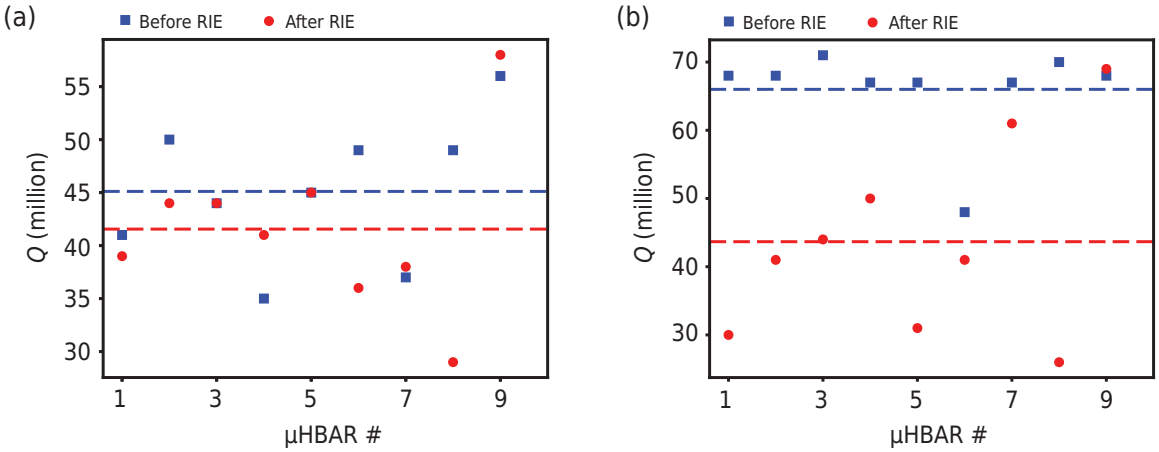

Figure 5.12: Extra phonon losses caused by RIE. (a) Backside (plano surface) over-etch test of substrate CQT15_1 that mimics the etch on the front side (dome surface). Before etching, the average Q of all nine µHBARs is 45 ± 6 million; after etching, the average Q of all nine µHBARs is 41 ± 7 million. (b) 80 min over-etch test of substrate CQT15_8 (40 min on each surface). Before etch, the average Q of all nine µHBARs is 66 ± 6 million; after etch, the average Q of all nine µHBARs is 43 ± 13 million.

sist after hard baking and estimated the etch duration needed to fully remove the photoresist. This is for minimizing the potential over-etch duration and mitigating RIE-introduced damages to the substrate surface. To verify that this actually works to our expectation, we spin-coated the back side of a 1.5-mm-thick µHBAR substrate (CQT15_1) with the same height of photoresist and ran the same RIE recipe for the same amount of time. Then we measured the phonon Q-factors to see if they were degraded by any amount. Note that the back side of the μHABR substrate has been intact during the whole fabrication. Therefore, whatever damage the RIE does to the front (dome) side should also be imprinted on the backside. Fig. 5.12a shows the measured Q-factors of all 9 µHBAR devices before and after the back side etch. 7 out of 9 devices don't show significant degradation in Q-factors. On average, the Q-factor changes from 45 ± 6 million (blue dashed line) to 41 ± 7 million (red dashed line).

Now it's safe to say that not much extra phonon loss has been introduced by the RIE process in our fabrication, because we intentionally minimize the over-etch duration to less than 10 min. However, long-time RIE over-etch can cause a serious problem. In the second experiment, we intentionally apply an extra 40 min etch on both the front side and back side (80 min in total) of another 1.5-mm-thick µHBAR substrate (CQT15_8, see Fig. 5.12b), significant Q degradation is observed. Some devices show Q degradation of more 50%. On average, the Q-factor drops from 66 ± 6 million to 43 ± 13 million, which indicates that the total phonon loss increases from 571 ppm to 877 ppm. The RIE-caused phonon loss during the 80 min over-etch is 306 ppm, i.e. 3.8 ppm/min. If we use this rate, 10-min over-etch will introduce no more than 40 ppm phonon loss, which is insignificant for non-polished substrates. In summary, RIE does introduce extra phonon losses, thus minimizing the over-etch duration is of vital importance for high-coherence µHBAR devices.

Chapter 6

Conclusion and outlook

In this thesis, I have demonstrated to you how we achieved nearly 10-ms coherence time for $>$ 10GHz phonons in our fabricated µHBARs. I started by introducing a reflow-based technique that enables scalable fabrication of those μHABRs with excellent shape control and surface roughness. Then we developed a novel noninvasive laser-based spectroscopy technique to measure the phonon spectrum (coherence time) and ring-down (lifetime). In this technique two pump and probe laser beams are used to drive and detect phonons via photon-phonon interaction. This actually manifests an optomechanical way of coupling to the µHBAR phonons which opens the door to many applications in cavity optomechanics. Next, by doing statistics of multiple µHBAR devices under varying temperatures and different surface participation ratios, we concluded that the phonon coherence time is limited by the energy dissipation associated with the device surface and subsurface. At last, combining powerful material diagnosis and surface characterization tools such as XRD and AFM, we identified that the dominating phonon dissipation comes from the coarse polishing finish during substrate manufacturing. Based on that, we developed a finer polishing recipe that eventually brings the phonon Q-factor to 360 million and the phonon coherence time to nearly 10 ms at 12 GHz.

Here I summarize the major findings in this thesis work:

- We fabricated μHBARs that reach Q-factors of 360 million for 12.66 GHz phonons, corresponding to a coherence time of 9 ms and a record-setting f-Q product of 4.6×10^{18} Hz.
- Pure dephasing rate is negligible in our μHBAR devices, meaning that the phonon coherence is only limited by phonon losses.
- The dominant phonon loss has been identified to come from the surface/subsurface damages associated to native polishing finish from the manufacture.
- We have developed a finer polishing recipe that can remediate the surface/subsurface damages, and finally achieve record-setting coherence times and f-Q products.

High-coherence phonons are a compelling resource in quantum computing as they permit numerous quantum operations within the coherence time. High-Q μHBAR devices with long coherence time has many applications in quantum sensing, quantum transduction, and quantum memory. There are two primary schemes to manipulate phonons in μHBAR devices: electromechanical coupling and optomechanical coupling. Electromechanical coupling to μHBARs typically relies on the piezoelectric effect, which only applies to materials that lack a center of symmetry in their crystal structure. For materials like sapphire, usually a piezoelectric player (for example, AlN) is coated on the surface. However, the piezoelectric will introduce extra phonon loss that will degrade the phonon Q-factor. The advantage of electromechanical coupling is that it typically has a stronger coupling rate than optomechanical coupling. Also, it can be more readily manipulated using the circuit-QED technique [7–9]. On the contrary, optomechanical coupling is a ubiquitous effect that applies to all materials. It doesn't need any coating on the device surface, thus keeps the phonons most intact. In this case, the μHBARs can keep the highest Q-factors and longest coherence times. However, the relatively low coupling rate has always been a challenge.

Recent advancements in cavity optomechanical might shine a light in solving this issue. From the analysis in Section 3.2, we know that the interaction is a three-wave mixing process. Under the stiff pump approximation, the optomechanical coupling rate is proportional to the pump field amplitude. If we put the μHBAR in a high-Q optical FP cavity, the coupling rate between the probe photon and phonon can be largely enhanced. Our group has recently demonstrated the ground-state cooling using this cavity-enhanced optomechanical coupling scheme [41].

At last, I want to point out that our reflow-based fabrication technique is applicable to all materials. It means in principle, we can build μHBAR devices in any material. Non-selective on material gives the freedom to explore different material platforms like diamond. Diamond is a very hard material which has a very high phonon speed (17.5 km/s). This results in a high Brillouin frequency of 54 GHz, which makes the ground state cooling much easier. Moreover, the synthesized diamond wafers through chemical vapor deposition can reach impurity concentration of ppb level. Most importantly, diamond is a solid-state platform rich in defect centers. Over the years, various types of color centers have been successfully coupled to phonons [42–45]. Similar to the cavity QED studies, the defect-phonon interaction will be significantly enhanced by the small volume and high coherence of the phonon modes in our μHBAR devices.

In summary, phononic resonators have played such an important role in quantum technology as it can easily couple to various types of quantum systems, such as superconducting qubit, optical photon and solid-state defect centers. In this thesis, we fabricate a special type of phononic resonator, the μHBAR, that reaches nearly 10-ms coherence time. Through systematic material study and surface characterization, we identified the limiting factors of this record-high coherence time and provided solutions to break the limits for even higher coherence times.

Bibliography

[1] M. Lombardi. The accuracy & stability of quartz watches. *Horological Journal*, 150(2):57, 2008.

[2] A. Elfes. Sonar-based real-world mapping and navigation. *IEEE Journal on Robotics and Automation*, 3(3):249–265, 1987.

[3] B. Drafts. Acoustic wave technology sensors. *IEEE Transactions on microwave theory and techniques*, 49(4):795–802, 2001.

[4] C. C. Ruppel. Acoustic wave filter technology–a review. *IEEE transactions on ultrasonics, ferroelectrics, and frequency control*, 64(9):1390–1400, 2017.

[5] D. Morgan. *Surface acoustic wave filters: With applications to electronic communications and signal processing*. Academic Press, 2010.

[6] K.-y. Hashimoto. *RF bulk acoustic wave filters for communications*. Artech House, 2009.

[7] Y. Chu, P. Kharel, T. Yoon, L. Frunzio, P. T. Rakich, and R. J. Schoelkopf. Creation and control of multi-phonon fock states in a bulk acoustic-wave resonator. *Nature*, 563(7733):666–670, 2018.

[8] U. Von Lüpke, Y. Yang, M. Bild, L. Michaud, M. Fadel, and Y. Chu. Parity measurement in the strong dispersive regime of circuit quantum acoustodynamics. *Nature Physics*, 18(7):794–799, 2022.

[9] E. A. Wollack, A. Y. Cleland, R. G. Gruenke, Z. Wang, P. Arrangoiz-Arriola, and A. H. Safavi-Naeini. Quantum state preparation and tomography of entangled mechanical resonators. *Nature*, 604(7906):463–467, 2022.

[10] D. Carney, G. Krnjaic, D. C. Moore, C. A. Regal, G. Afek, S. Bhave, B. Brubaker, T. Corbitt, J. Cripe, N. Crisosto, et al. Mechanical quantum sensing in the search for dark matter. *Quantum Science and Technology*, 6(2):024002, 2021.

[11] M. Goryachev and M. E. Tobar. Gravitational wave detection with high frequency phonon trapping acoustic cavities. *Physical Review D*, 90(10):102005, 2014.

[12] A. Lo, P. Haslinger, E. Mizrachi, L. Anderegg, H. Müller, M. Hohensee, M. Goryachev, and M. E. Tobar. Acoustic tests of lorentz symmetry using quartz oscillators. *Physical Review X*, 6(1):011018, 2016.

[13] R. Linehan, T. Trickle, C. R. Conner, S. Ghosh, T. Lin, M. Sholapurkar, and A. N. Cleland. Listening for new physics with quantum acoustics. *arXiv preprint arXiv:2410.17308*, 2024.

[14] H. Zhao, A. Bozkurt, and M. Mirhosseini. Electro-optic transduction in silicon via gigahertz-frequency nanomechanics. *Optica*, 10(6):790–796, 2023.

[15] M. Mirhosseini, A. Sipahigil, M. Kalaee, and O. Painter. Superconducting qubit to optical photon transduction. *Nature*, 588(7839):599–603, 2020.

[16] T. Yoon, D. Mason, V. Jain, Y. Chu, P. Kharel, W. H. Renninger, L. Collins, L. Frunzio, R. J. Schoelkopf, and P. T. Rakich. Simultaneous brillouin and piezoelectric coupling to a high-frequency bulk acoustic resonator. *Optica*, 10(1):110–117, 2023.

[17] M. J. Weaver, P. Duivestein, A. C. Bernasconi, S. Scharmer, M. Lemang, T. C. v. Thiel, F. Hijazi, B. Hensen, S. Gröblacher, and R. Stockill. An integrated microwave-to-optics interface for scalable quantum computing. *Nature Nanotechnology*, 19(2):166–172, 2024.

[18] A. Wallucks, I. Marinković, B. Hensen, R. Stockill, and S. Gröblacher. A quantum memory at telecom wavelengths. *Nature Physics*, 16(7):772–777, 2020.

[19] G. S. MacCabe, H. Ren, J. Luo, J. D. Cohen, H. Zhou, A. Sipahigil, M. Mirhosseini, and O. Painter. Nano-acoustic resonator with ultralong phonon lifetime. *Science*, 370(6518):840–843, 2020.

[20] A. B. Bozkurt, O. Golami, Y. Yu, H. Tian, and M. Mirhosseini. A mechanical quantum memory for microwave photons. *arXiv preprint arXiv:2412.08006*, 2024.

[21] C. T. Hann, C.-L. Zou, Y. Zhang, Y. Chu, R. J. Schoelkopf, S. M. Girvin, and L. Jiang. Hardware-efficient quantum random access memory with hybrid quantum acoustic systems. *Physical review letters*, 123(25):250501, 2019.

[22] M. Aspelmeyer, T. J. Kippenberg, and F. Marquardt. Cavity optomechanics. *Reviews of Modern Physics*, 86(4):1391–1452, 2014.

[23] L. Landau and G. Rumer. Uber schall absorption in festen körpen. *Phys. Z. Sowjetunion*, 11(18):18–25, 1937.

[24] P. Klemens. Effect of thermal and phonon processes on ultrasonic attenuation. In *Physical Acoustics*, volume 3, pages 201–234. Elsevier, 1965.

[25] H. J. Maris. Interaction of sound waves with thermal phonons in dielectric crystals. In *Physical Acoustics*, volume 8, pages 279–345. Elsevier, 1971.

[26] M. Goryachev, D. L. Creedon, E. N. Ivanov, S. Galliou, R. Bourquin, and M. E. Tobar. Extremely low-loss acoustic phonons in a quartz bulk acoustic wave resonator at millikelvin temperature. *Applied Physics Letters*, 100(24), 2012.

[27] S. Galliou, M. Goryachev, R. Bourquin, P. Abbé, J. P. Aubry, and M. E. Tobar. Extremely low loss phonon-trapping cryogenic acoustic cavities for future physical experiments. *Scientific reports*, 3(1):2132, 2013.

[28] P. Kharel, Y. Chu, M. Power, W. H. Renninger, R. J. Schoelkopf, and P. T. Rakich. Ultra-high-q phononic resonators on-chip at cryogenic temperatures. *Apl Photonics*, 3(6):066101, 2018.

[29] R. W. Boyd, A. L. Gaeta, and E. Giese. Nonlinear optics. In *Springer Handbook of Atomic, Molecular, and Optical Physics*, pages 1097–1110. Springer, 2008.

[30] R. Chiao, C. H. Townes, and B. Stoicheff. Stimulated brillouin scattering and coherent generation of intense hypersonic waves. *Physical review letters*, 12(21):592, 1964.

[31] G. P. Agrawal. Nonlinear fiber optics. In *Nonlinear Science at the Dawn of the 21st Century*, pages 195–211. Springer, 2000.

[32] W. A. Phillips. Two-level states in glasses. *Reports on Progress in Physics*, 50(12):1657, 1987.

[33] R. G. Gruenke-Freudenstein, E. Szakiel, G. P. Multani, T. Makihara, A. G. Hayden, A. Khalatpour, E. A. Wollack, A. Akoto-Yeboah, S. Salmani-Rezaie, and A. H. Safavi-Naeini. Surface and bulk two-level system losses in lithium niobate acoustic resonators. *arXiv preprint arXiv:2501.08291*, 2025.

[34] H. Warlimont and W. Martienssen. *Springer handbook of materials data*. Springer, 2018.

[35] A. G. Fox and T. Li. Resonant modes in a maser interferometer. *Bell System Technical Journal*, 40(2):453–488, 1961.

[36] D. Kleckner, W. T. Irvine, S. S. Oemrawsingh, and D. Bouwmeester. Diffraction-limited high-finesse optical cavities. *Physical Review A*, 81(4):043814, 2010.

[37] J. Sipe and M. Steel. A hamiltonian treatment of stimulated brillouin scattering in nanoscale integrated waveguides. *New Journal of Physics*, 18(4):045004, 2016.

[38] W. Renninger, P. Kharel, R. Behunin, and P. Rakich. Bulk crystalline optomechanics. *Nature Physics*, 14(6):601–607, 2018.

[39] G. F. Harrington and J. Santiso. Back-to-basics tutorial: X-ray diffraction of thin films. *Journal of Electroceramics*, 47(4):141–163, 2021.

[40] E. Letts, Y. Sun, D. Key, B. Jordan, and T. Hashimoto. X-ray characterization technique for the assessment of surface damage in gan wafers. *Journal of Crystal Growth*, 501:13–17, 2018.

[41] H. H. Diamandi, Y. Luo, D. Mason, T. B. Kanmaz, S. Ghosh, M. Pavlovich, T. Yoon, R. Behunin, S. Puri, J. G. Harris, et al. Quantum optomechanical control of long-lived bulk acoustic phonons. *arXiv preprint arXiv:2410.18037*, 2024.

[42] H. Chen, N. F. Opondo, B. Jiang, E. R. MacQuarrie, R. S. Daveau, S. A. Bhave, and G. D. Fuchs. Engineering electron–phonon coupling of quantum defects to a semiconfocal acoustic resonator. *Nano letters*, 19(10):7021–7027, 2019.

[43] E. MacQuarrie, T. Gosavi, N. Jungwirth, S. Bhave, and G. Fuchs. Mechanical spin control of nitrogen-vacancy centers in diamond. *Physical review letters*, 111(22):227602, 2013.

[44] E. MacQuarrie, T. Gosavi, A. Moehle, N. Jungwirth, S. Bhave, and G. Fuchs. Coherent control of a nitrogen-vacancy center spin ensemble with a diamond mechanical resonator. *Optica*, 2(3):233–238, 2015.

[45] S. Maity, L. Shao, S. Bogdanović, S. Meesala, Y.-I. Sohn, N. Sinclair, B. Pingault, M. Chalupnik, C. Chia, L. Zheng, et al. Coherent acoustic control of a single silicon vacancy spin in diamond. *Nature communications*, 11(1):193, 2020.